UNIVERSITÁ DEGLI STUDI DI NAPOLI FEDERICO II

DIPARTIMENTO DI INGEGNERIA CHIMICA, DEI MATERIALI E DELLA PRODUZIONE INDUSTRIALE

TESI DI DOTTORATO IN INGEGNERIA DEI PRODOTTI E DEI PROCESSI INDUSTRIALI
XXIX CICLO

Shape Memory Polymers Charged with Modified Carbon-Based Nanoparticles

RELATORE
Prof.ssa VERONICA AMBROGI

CANDIDATO
GIUSEPPE CESARE LAMA

CORRELATORE
Dott. PIERFRANCESCO CERRUTI

Anno Accademico 2016/2017

“Se vogliamo che
tutto rimanga com'è,
bisogna che tutto cambi”

[Tancredi Principe di Falconeri,
Il Gattopardo, Giuseppe Tomasi di Lampedusa]

Abstract

In this thesis, shape memory nanocomposites were prepared and characterized. The polymer matrix consisted in an epoxy-based liquid crystalline elastomer (LCE). Multi-walled carbon nanotubes (MWCNT) and graphite nanoplatelets (GNP) were selected as fillers. The influence of different contents of nanofillers on mechanical, thermal and shape memory properties was evaluated.

In order to disperse and homogeneously distribute the nanofillers within the polymer matrix an in-depth evaluation on the optimal conditions to synthesize the materials was carried out. These conditions had a substantial influence on the final distribution of the nanofillers within the epoxy-based matrix, which was analyzed from a macroscopic and microscopic point of view. The best results were obtained through a chemical surface modification of the nanoparticles.

The chemical modification of MWCNTs consisted in grafting the selected epoxy monomers on the surface. The obtained adducts were characterized in terms of chemical, thermal and morphological features.

Concerning GNP, a similar protocol based on surface modification was carried out. In this case, a preliminary oxidation process was performed in order to promote the exfoliation of graphene sheets, in form of graphene oxide (GO), and to favour their dispersion within the polymer matrix. Different degrees of oxidation were attempted.

GO nanoparticles were successively modified with epoxy monomers. Also in this case, chemical, morphological, structural and thermal characterization was carried out.

Surface modified carbonaceous nanoparticles were then dispersed in varying amounts in the organic matrix. The obtained nanocomposite systems were characterized in their chemical-physical and morphological properties. The adopted compatibilization strategies used for both MWCNTs and GNP were found to be extremely effective to get homogeneous

samples and to enable a dramatic enhancement of the actuation extent at low nanofiller content. Moreover, the stress threshold required to trigger the reversible thermomechanical actuation was significantly decreased. The effect of nanoparticles on thermomechanical properties of the materials was correlated to the microstructure and the phase behavior of the host system. Results demonstrated that the incorporation of carbon nanofillers amplified the soft-elastic response of the liquid crystalline phase to external stimuli. Tunable thermomechanical properties of these systems make them suitable for a variety of potential advanced applications ranging to robotics, sensing and actuation, and artificial muscles.

Table of Contents

CHAPTER 1

Introduction

1.1. Shape Memory Materials

Smart materials are one of the most interesting subject in materials science, as confirmed by numerous studies and papers published over the years. [1,2,3,4,5] In order to be considered smart, a material has to show the ability to respond to one or more external stimuli, and to adapt his properties to the new environment. The main ability of smart materials consists in acting as sensors and actuators at the same time. Consequently, they behave as transducers: when they receive an external stimulus, such as temperature,[6] light/color,[7] electric/magnetic field [8,9] or mechanical stress/strain,[10] they respond by changing some of their properties.

Several smart materials are known, classified on the basis of the specific stimulus they are able to respond to [11]. Some examples are reported in the Figure 1.1. Piezoelectrics are those materials showing a mechanical response when an electric or magnetic field is applied. Viceversa, if they undergo a stress, their response is a generated electric field. Mechanochromic materials react to an applied stress emitting with. For the electrochromic ones, the same response is triggered by an applied electric or magnetic field. However, the most common stimulus used to elicit a response from a smart material is the change of temperature. As an example, the materials able to emit light when heated are called thermochromic. Instead, pyroelectricity is relative to the generation of a thermal-induced electric/magnetic field. Finally, if a material shows a mechanical response when heated, it is considered a shape memory material.

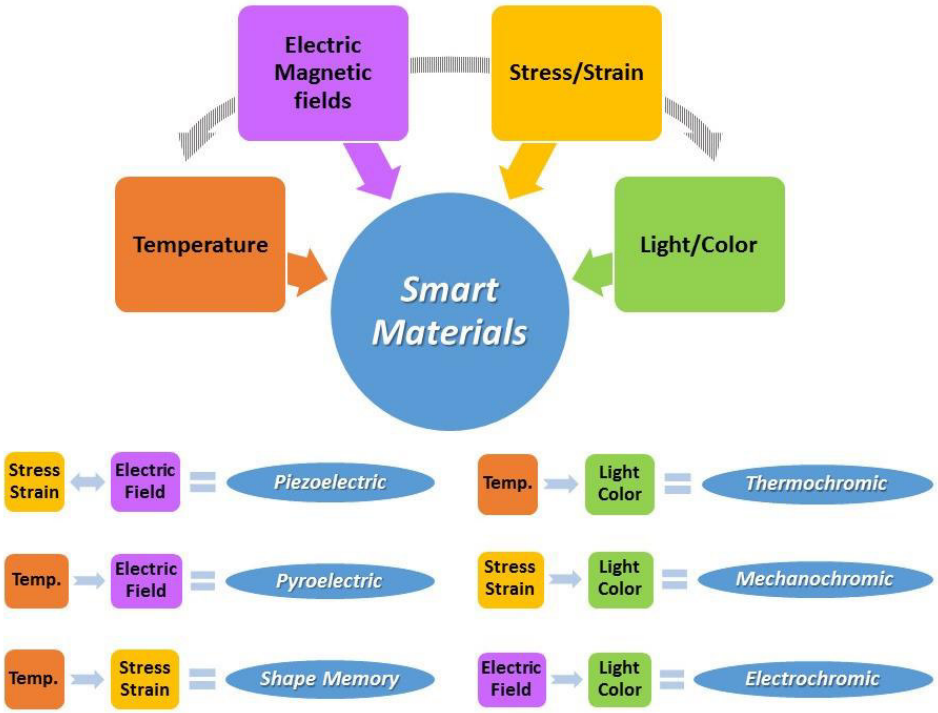

Figure 1.1 Classification of Smart Materials

Shape memory materials (SMM) represent one of the most investigated categories among smart materials. As shown in Figure 1.2, the attention devoted to these materials has significantly increased over the years.

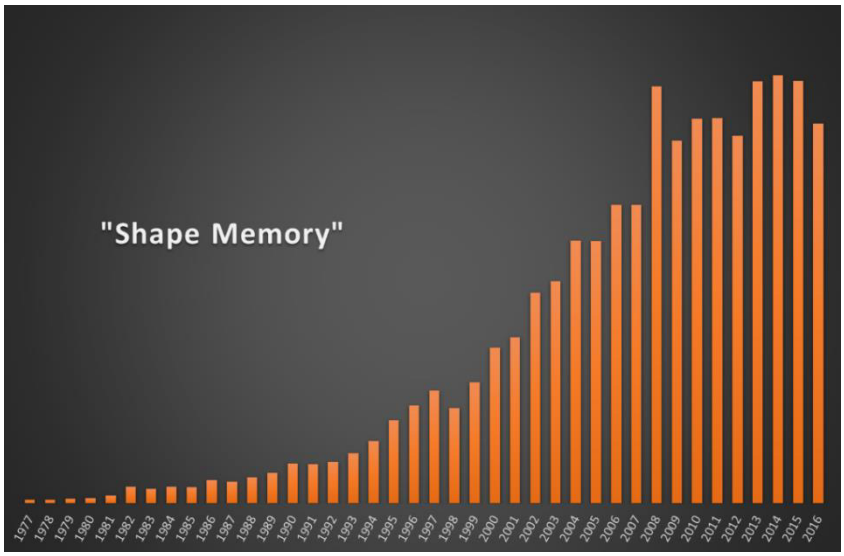

Figure 1.2 Trend of number of papers with “Shape Memory” as main subject from 1977 to 2016” (quote scopus.com).

The most distinguishing property of these materials stands in their ability to recover the deformation they experience. This is what is called shape memory effect (SME).[12,13,14]

When a SMM is in its steady state, it is in its "permanent shape". Then, if the material undergoes a deformation in controlled conditions, that is the "programming" process, it turns into the so-called "temporary shape". This latter state is kept until the material is allowed return to its "permanent shape", through a "recovery" process.[1-15]

Materials exhibiting SME have been widely used in many advanced fields, such as biomedical, [16] aerospace [17] and bionics,[18] electronic,[19] and civil engineering.[20]

The accounts concerning the discovery of this effect, and the statements about the first scientist reporting on this phenomenon are a bit ambiguous. The first scientist who was able to observe a pseudo-elastic behavior of gold-cadmium alloy was A. Olander, in 1932. In one of his works Olander wrote that, after an annealing process, some materials responded in an elastic way, so that they reminded of a rubber. Also, a first clue of a shape-shifting behavior was reported: after calculating the entropy content before and after the formation of the alloy, the author found out that an actual displacement of atoms (misplaced atoms) occurred in the material, so that some vacancies were created in the lattice.[21]

About 20 years later, in 1952, Chang and Read performed X-ray analysis on the same Au-Cd alloy prepared by Olander. They observed that this material experienced an unusual diffusionless change of the lattice when the sample was heated and cooled over a very short range of temperature. They concluded that a more detailed study on the role played by structural imperfections was required to better understand this phenomenon, since the specimen changed from an orthorhombic structure to a body centered cubic one, upon the rubbery-like recover of its original shape.[22]

In 1962, Buehler first wrote about a material with memory. His coming across this new class of material was an evident case of serendipity, since this behavior was observed by chance, thanks to a “fortunate fall” of two different rods made of the same material, Ni-Ti alloy that, when hit the ground, made two different sounds. This was due to the different thermal process they experienced before this occurrence. This had resulted in the formation of different crystalline structures of the material, depending on the rate of cooling. These two arrangements are the austenitic, formed at high temperature, and the martensitic, which is a metastable structure that arises at lower temperature. The latter can be twinned or detwinned, depending on the stress applied. Then, from a macroscopic point of view, when the specimen switches from one to the other structure, it experienced a sensible size change. This alloy was baptized Niti-NOL (NiTi – Naval Ordinance Laboratory) and the study on SME started.[23,24]

As far as organic shape memory materials is concerned, a step-back in time to 1941 is necessary, when Vernon and Vernon first gave the actual description of the SME, without naming it, in a patent about new materials for dental restoration. They were the first to give a know-how in the field, covering a wide range of “plasters” and resins. The patent was about the preparation of a methacrylate-based material exhibiting SME when underwent temperature changes, from room temperature, where it showed a hardening typical of gum, to temperatures below zero, where it recovered its softness ad the rubbery behavior.[25]

Even if the investigation in these systems may be considered as purely man-made, many different examples already exist in nature. One of the most common shape-shifting natural system is the pinecone, which can change its configuration, from open to close, if the environment is dryer or moister, respectively. This happens in order to protect the seed and to let it travel as much as possible. When it is produced, the seed has to be protected

from the water in the air: if the seed gets wet, it will be heavier and it will fall too close to the parent tree. Instead, if the weather is dry and windy, the pinecone will open its scales, and the seed is allowed to leave the pinecone, so that it can reach longer distances, and proliferate (Figure 1.3).[26]

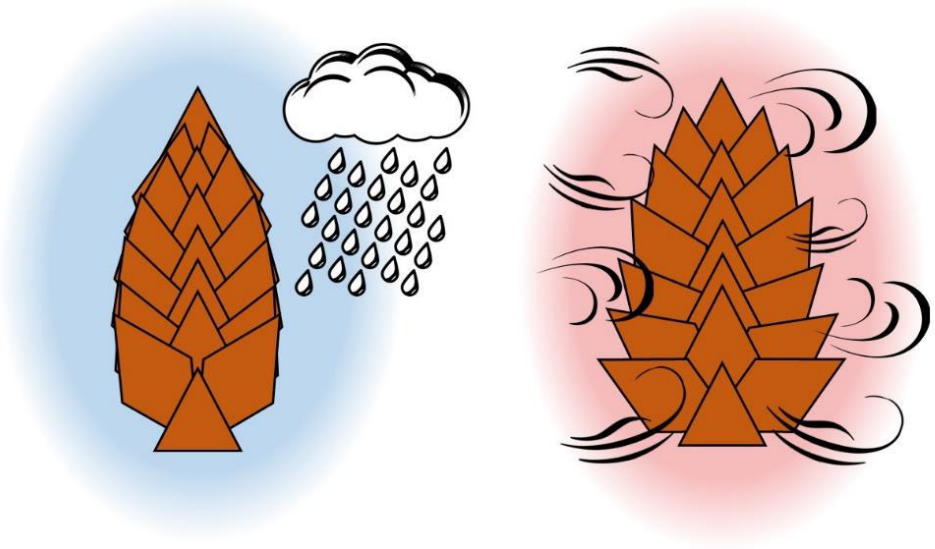

Figure 1.3 Scheme of closed pinecone with cold and wet weather (left); Scheme of an opened pinecone with dry and hot weather (right)

Other widely studied structures in natural world, which can be considered as shape-shifting, are the red blood cells (RBCs). They can experience a change in their shape simply by a variation of the salinity of the solution in which they are immerged. It is all about osmosis process, thanks to which, if the solution is isotonic (meaning that the solution has the same amount of solute of the RBC), the system will be steady. However, if the solution has a higher ionic strength with respect to RBC (i.e. it is hypertonic), and cell shrinks, because of its tendency to equilibrate the concentration of solute inside and outside the cell itself. On the other hand, if the solution is hypotonic, with a lower amount of solute with respect to the RBC, water moves through the membrane into the cell (Figure 1.4).[27,28]

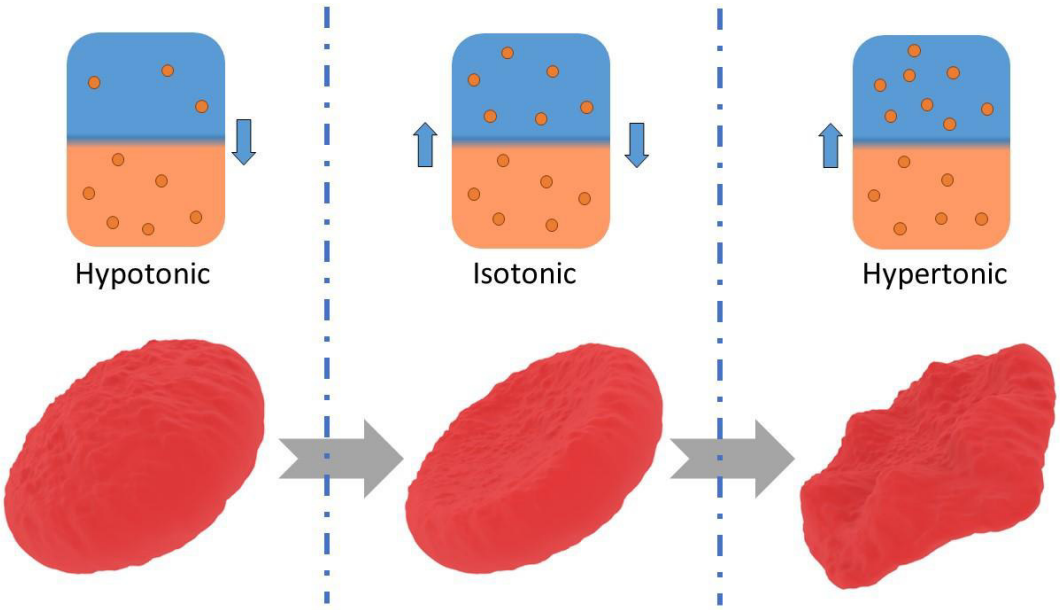

Figure 1.4 Left: hypotonic solution gives sphere-like RBC. Center: in isotonic solution, RBC keeps its shape. Right: hypertonic solution gives shrinked RBC.

By the way, a large variety of substances belongs to the class of shape memory materials, such as shape memory alloys (SMA), shape memory ceramics (SMC), shape memory polymers (SMP) and shape memory hybrids and composites (SMH and SMNc) (Figure 1.5). They will be presented in a more detailed way hereafter.

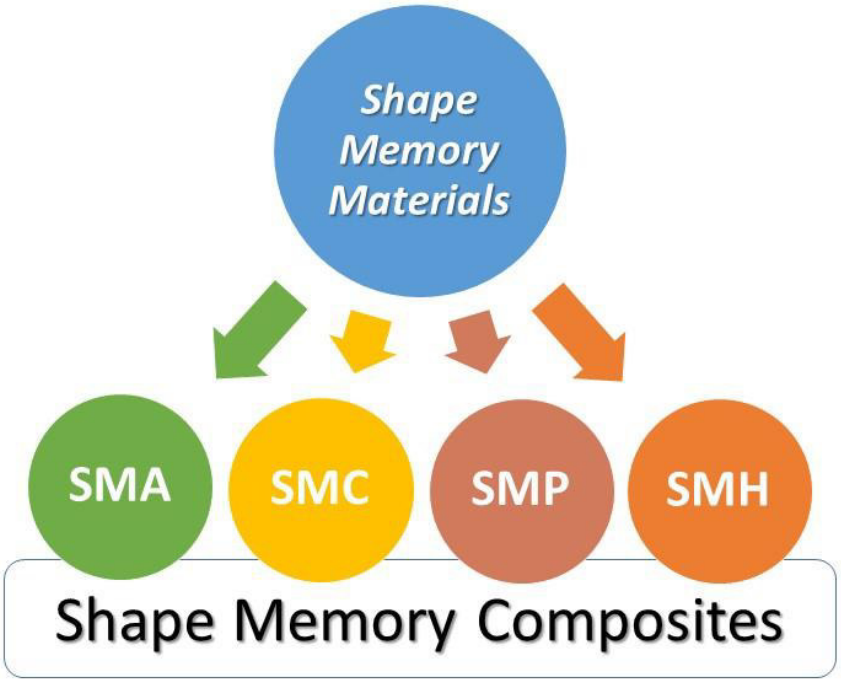

Figure 1.5 Classification of shape memory materials

1.2. Shape Memory Alloys (SMA)

Shape memory alloys (SMA) are the most studied classes of material showing shape memory effect [29,30]. One of the main reasons for their diffusion is that the starting materials are relatively cheap and easy to process, since they are metals.

As partly beckoned, these materials can exist in two phases, austenite and martensite, having the second two different possible arrangements, twinned and detwinned, generated by thermal changes. Therefore, for in SMAs it is necessary to identify some characteristic temperatures.[31]

In particular, at low temperature, martensite structure is stable. Upon heating , as soon as the material reaches the austenite-start-temperature (A_s), it changes its structure into austenitic one. The transformation is completed when the sample reaches the austenite-finish-temperature (A_f). This step can also occur while a load is applied. In both cases, the material experiences a contraction. Then, if the alloy is cooled down, it experiences the

reverse transformation, showing a switch to martensite as soon as it reaches the martensite-start-temperature (M_s). The conversion runs out when the material reaches the martensite-finish-temperature (M_f). The shape-shift to martensite can also be load-induced. Nevertheless, there is another limit temperature, named M_d, above which the martensite can not be observed with the application of a load.[24,32]

In order to better figure out how a SMA behaves at different temperatures and loads, a classification is needed. One-way SMAs (1W-SMA) are those materials that, once deformed, recover their original shape when heated, and no other changes occur. Two-way SMAs (2W-SMA) can switch from one shape to another, being one stable at high temperatures, and the other at low temperatures. They are less common, since they present several inconveniences with respect to 1W-SMAs, such as the necessity of programming in two different phases, a lower strain recovery and a higher rate of deterioration. [33,34] In the end, when the SMA is at a temperature between A_f and M_d, the shape-shifting from austenite to martensite and backwards can be displayed simply by loading or unloading the material, without any changes in temperature. This phenomenon is called pseudoelasticity. A 1W-SMA can also become a 2W-SMA if a constant load is applied to the specimen. This kind of system is effective, expendable and common in various applications.[35] A complete outlook of such behavior is reported in Figure 1.6.

As already mentioned, from a structural point of view, the SME is a diffusionless transition from austenite to martensite. [36] This transition is usually temperature-assisted. The term hysteresis defines the range of temperatures where the material can be applied, $\Delta T = A_f - M_s$. It is identified between those temperatures at which the material is 50% austenite while heating and is 50% martensite while cooling. [37] Once the extent of hysteresis is known, the material can be considered for a specific application. For example, for mini electro-mechanical systems (MEMSs), a narrow hysteresis is required. Instead, in

order to have, for example, a pipe joint that keeps the shape for a long time and in a wide temperature range, a SMA with a larger hysteresis is required. [38]

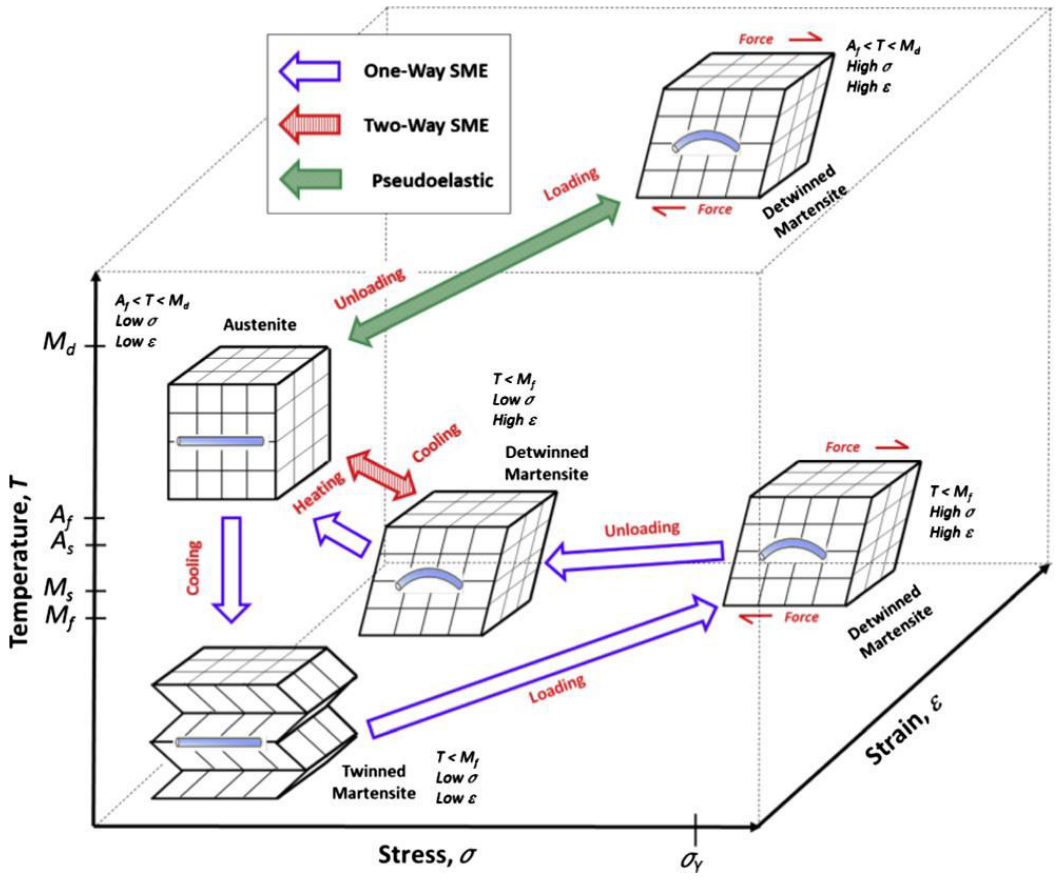

Figure 1.6 SMA phases and crystal structures [39]

The hysteresis loops depend on different factors, such as composition and thermomechanical stresses experienced by the material during processing and application. [40] Such thermal characterization can be easily performed by differential scanning calorimetry (DSC). [41] In this range of temperature, also mechanical, physical and thermal properties (such as Young's modulus, electrical resistivity and thermal conductivity) may change, depending on the phase, since austenite is harder and has a higher Young's modulus with respect to martensite. [42,43]

Thanks to their behavior, SMAs are applied in many fields. For instance, in cardiovascular and spinal surgery, dental and sports medicine are required advanced tools and systems, such as stent grafts, valve sizers, bone staples and arch wires, as well as locking rings, safety valves and control systems in automotive, aerospace and defense. Some of the leaders in the production and manufacturing of NiTiNOL are the Memry Corporation and Dynalloy, Inc., specialized in kits and accessories for their application.

However, SMA cannot experience deformations higher than 10%. [22] As later explained, other materials can be used in order to obtain a SME with higher deformation and processability.

1.3. Shape Memory Ceramics (SMC)

Another class of SMM is represented by shape memory ceramics (SMC). The maximal deformation they can reach is about 15%. This deformation is related to the shear strain associated to the martensitic transformation from tetragonal to monoclinic structure of the zirconia. [44] However, the real SME can be displayed only for strains lower than 2%. Moreover, the number of cycles the material can withstand before it starts to crack are much lower than SMA. [45] For this reason, in recent years the attention devoted to these materials is lower respect to SMAs. A quick synopsis is here reported.

The first main group of SMCs consists in viscoelastic ones. These materials, once deformed at high temperature, can be cooled down, in order to “freeze” the obtained shape. Then, the recovery can occur, with a prestrain up to 0.5%, by simply heating the specimen.[46] However, since they exhibit a structure in which 0.4-0.6 of volume fraction is mica, dispersed in a continuous glassy phase, the SME occurs in a different way from SMA. This is due to the interaction between the crystalline structure and the glassy phase. While

loading, the first is deformed and the second flows with it. Once the load is removed, the form is kept, until it is reheated and the energy stored in the glassy phase will be released and used as for recovering the original shape. The strain recovery can reach 99% if the sample undergoes a long annealing process. [47] In addition, some sintered ceramics with a very little amount of glassy phase shows SME, but this is much lower than the effect exhibited by the others.[48]

As for SMA, some SMCs can experience a thermally or stress activated martensitic transition, giving malleability or toughening, respectively. [49] In ceramics, if the transformations are thermoelastic, SME can be expected. Zirconia (ZrO) can show such behavior, since the structural switch from tetragonal (t) to monoclinic (m) at low temperature can occur thermoelastically. Also magnesia or cesia modified zirconia can show SME. This effect can be triggered lowering the temperature down to the t – m transition, whose value depends from the grain size of the solid phase. If the sample is above the transition temperature, the SME can be activated applying a stress. Once deformed, the original shape can be recovered reheating with a m – t transition. The great advance in this kind of materials stands in the possibility to use them at very high temperatures, but the higher strain value reachable is lower than 4%, and microfractures arises, limiting their applicability. [50,51]

Among SMCs, ferroelectrics are much similar to the well-known piezoelectric smart structures. [52] Those are perovskite-type oxides which can be paraelectric (PE), ferroelectric (FE) or antiferroelectric (AFE), depending on the composition and the crystalline lattice. These different lattices can appear depending on temperature, stress or external electric field. Macroscopical strains occur when PE-FE and AFE-FE transitions take place. [53] The latter can be induced applying an external electric field that reorients the polarized domains. This phenomenon causes a structure displacement and a subsequent volume

expansion, even larger than the piezoelectrics' one, due to the spontaneous strain, connected to the phase transformation, and to the electrical-induced one. [54,55] If the ceramic is metastable at FE and AFE, when the electric field is removed, the structure is kept until the electric field changes its polarity or the temperature is raised. In this case, the material shows SME. [56]

Some other metal oxides can show orbital order-disorder arrangements, such as paramagnetic, ferromagnetic and antiferromagnetic. The reversible transitions between these structures result in recoverable lattice alterations. [57] In this case, SME takes place, since ordered and disordered structures coexist and the Jahn-Teller transition between ferromagnetic and antiferromagnetic states occurs in short range. These class of SMCs is not much investigated because the switch temperatures between the states are very low.

However, SMCs find application in mechanics, as clamping devices,[58] and in electronics, as latching relays in switching systems, thanks to the low deformation, to guarantee the electrical contact, even though the voltage is no longer applied to the device.[36]

1.4. Shape Memory Polymers (SMP) and Elastomers (SMEL)

As mentioned above, SMPs are one of the most studied classes among responsive (or programmable) materials. In many cases, depending on the structural and chemical properties of the sample, the restoration of the original shape takes place as a response to different external stimuli, such as a variation of pH [59] or temperature, [60] or as a consequence of the application of an electric or magnetic field [61].

The first SMP to be invented was reported in 1984, in Japan. However, other traces of their first appearances was described in 1906 in terms of heat-, and water-shrinkable polymer [62] and lately the well-known and used heat-shrinking tube made of polyethylene to protect connections, joints and conductors. [63]

Compared to SMAs, SMPs exhibit several advantages. First of all, the density of the material is much lower (the most common polyurethane (PU) has a density of 1.25 g/cm^3, whereas NiTi is 6.4 g/cm^3). [64] The cost for the raw material and for the process is usually lower, even for complex shapes. As for the SME, SMP have a total recovery that can be even several orders of magnitude higher than SMA. Moreover, the thermomechanical properties can be tailored in a simple way, by varying the monomer ratio or by the addition of fillers. Moreover, these materials possess an excellent chemical stability, a high damping ratio, and most of them are biocompatible, therefore potentially suitable for drug delivery.

Thermoresponsive SMPs can be triggered by direct heat, or by means of induction, infrared, laser heating, or with Joule effect. Other documented ways to activate the SME are moisture, pH, solvent, light, electric or magnetic fields. The latter can also allow to engineer remote-controlled SMP, thanks to induction heating. One single SMP can be activated by different external stimuli, so that SMPs with multiple SME can be realized.

In general, in order to show a shape memory effect, a polymer material should have two main structural features. First, the presence of a stable polymer network; this can be achieved thanks to entanglements, chemical cross-linking, interpenetrated network or crystalline phase. The presence of one of more of these features gives the sample the possibility of recovering the original (or permanent) shape to the sample. Secondly, it must possess a reversible switch, i.e. a physical or chemical transition that allows the SME to occur. Depending on the nature of polymer network, the switch may occur in different ways, for example crystallization-melting transition [65], vitrification-glass transition [66],

anisotropic-isotropic transition for liquid crystals [67], reversible molecular cross-linking, like photo-isomerization [68], and supramolecular association-dissociation, such as hydrogen bonding or self-assembly [69]. In Figure 1.7, an overview on shape-shifting modes is reported.

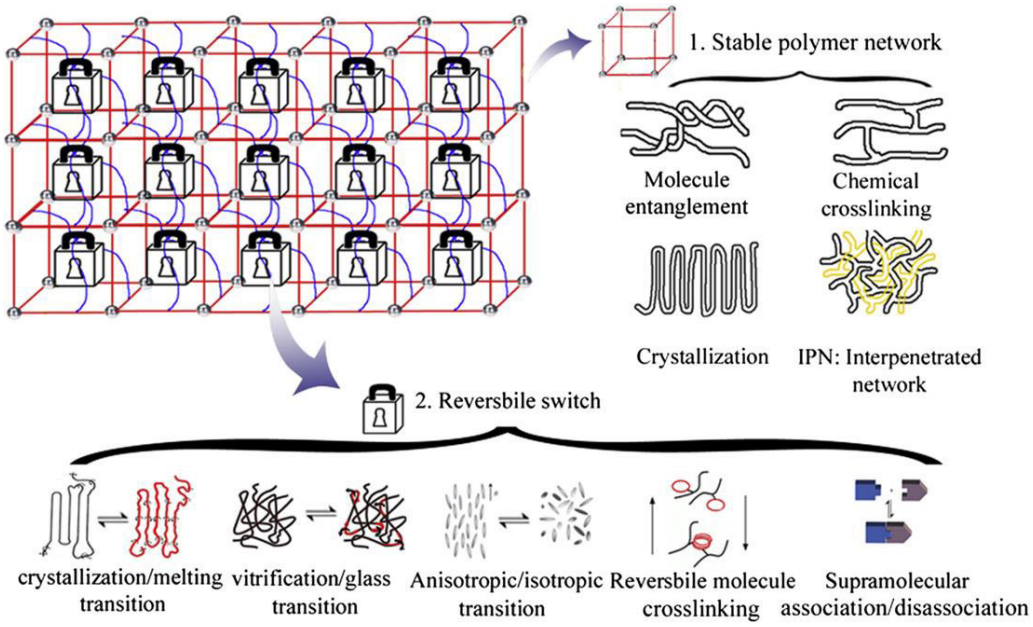

Figure 1.7 Various molecular structures of SMPs [79]

Among SMPs, a prominent role is played by shape memory elastomers (SMEL). In general, elastomers are polymer-based thermoset materials having a three-dimensional structure, with the distinctive presence of chemical cross-links between polymer chains. The amount of concatenated chains arises from the typical curing process of thermosetting polymers, which involves the reaction between a monomer and a curing agent. The complex network formed may present a different viscoelastic behavior, in terms of intermolecular forces, failure strain and Young's modulus, depending on kind and amount of the curing agent used. [70]

When an elastomer experiences a stress, its structure changes, and the polymer chains align along the direction of the applied stress. Then, when the load is removed, the

elastomer has the ability to restore its original condition thanks to the presence of the cross-links. Furthermore, an elastomer usually presents an amorphous structure, as the crosslinks inhibit chain crystallization. However, if one among monomer or curing agent has a rigid rod-like structure, a so-called liquid crystalline elastomers (LCE) could be formed [71]. In such a structure, the rigid-rod moieties, also called mesogens, can arrange in a side by side ordered structure, forming several locally aligned domains surrounded by an amorphous phase.

Just like other liquid crystalline materials, LCEs and liquid crystalline polymers (LCP) may be classified according to the kind of arrangement of the mesogens. The main liquid crystalline classes are; nematic, in which the mesogens are ordered along one direction; smectic, in which several stacked layers made of ordered mesogens are present; cholesteric, where the aligned mesogens are organized in layers, but with a different orientation in each one of them (Figure 1.8).

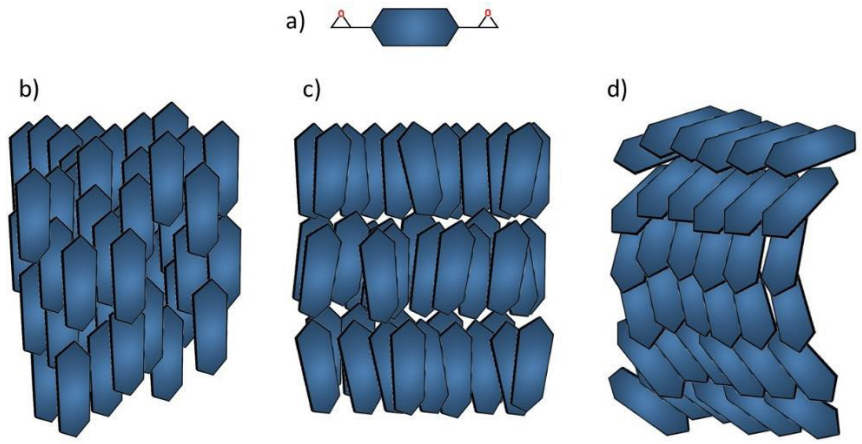

Figure1.8. Schematic representation of a) LC monomer,and of b) nematic , c) smectic and d) cholesteric LC arrangements.

In addition to this classification, another relevant parameter for LCPs classification is the position of the mesogens with respect to the polymer backbone. If the mesogen is part of the polymer backbone, then a main-chain LCP is formed. Instead, if the mesogens are grafted to the backbone, the resulting LCP is classified as a side-chain polymer. Moreover, side-on or end-on bonding is possible, depending on how the mesogen is connected to the backbone, [72] as reported in Figure 1.9.

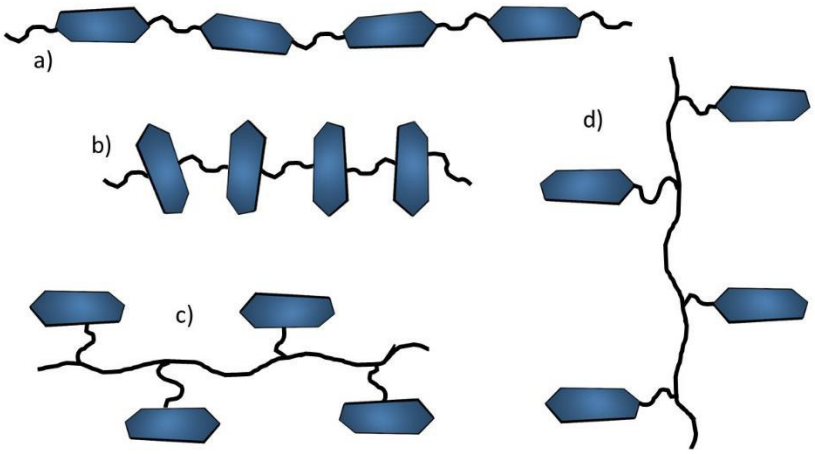

Figure 1.9 a) and b) are schematic representation of main-chain LC; c) and d) are schematic representation of side-chain LC, the first is side-on and the second is end-on one.

From a thermal point of view, liquid crystalline materials exhibit two different characteristic temperatures. The first one, usually occurring at lower temperature, is the glass transition (T_g), where, as with other semicrystalline polymers, the amorphous structure changes from glassy to rubbery. The second one, typically at higher temperature, is relative to the isotropization transition (T_i), where the ordered liquid crystalline (LC) arrangement is lost on heating, and the material becomes isotropic, resulting in a homogeneously disordered matrix. [73]

The isotropization process (as well as the reversed one, called anisotropization, occurring on cooling) requires the material to absorb a high amount of energy. However, thanks to this stored energy, some LCEs can show the SME. After the material is heated past T_i, it can be deformed to make it reach its temporary shape. During the process, the molecular structure is oriented along the stress direction. The sample is the cooled down below T_i so that any elastic response is inhibited. The sample is then unloaded and the shape memory effect can be triggered, simply rising the temperature up to the isotropization value, at which the aligned network releases the stored energy in form of mechanical work, to move back to its original position. Nevertheless, at this temperature the material in the actual permanent shape is still in the isotropic phase. The complete recover of the LC structure is then achieved upon the subsequent a cooling process. Of course, a loading applied prior to cooling results in a sample deformation, which can be used to trigger another shape recovery cycle. [74]

LCEs show excellent mechanical and physical properties, such as high fracture toughness, high moduli when oriented, low moisture adsorption and good thermal behavior, properties that are not observed in materials like amorphous or semi-crystalline polymers. [75]

On the basis of these properties, and also considering the ease of processing and low shrinkage after curing, lightly crosslinked epoxy resins are among the most studied liquid crystalline elastomers. They are produced by curing an epoxy monomer, usually having a stiff structure, with carboxylic acids having flexible aliphatic backbone.

As it is widely studied, the degree of crystallinity of the material obtained depends on the curing process, because for some epoxy monomers the liquid crystalline phase is metastable. Therefore, depending on the kinetics of reaction and the resulting crosslinked network, different typologies of ordered phase can be formed. [76]

Once the material is totally cured, mechanical and thermal behaviors are influenced by the LC domains. The strength to fracture and plastic deformation is increased thanks to the presence of liquid crystallinity. Each LC domain has the tendency to follow the direction of the solicitation, changing its orientation. The mechanism, known as transition from polydomain to monodomain, occurs while the load is applied. This definition comes out since all mesogens of the sample are pointing in the same direction. [77]

The local or global alignment causes the formation of an anisotropic material, whose structure can be tailored in many ways. In addition to changing the condition of the curing reaction and under mechanical stress, the LC arrangement can be oriented also under magnetic and electric field.

Moreover, as mentioned above, the exceptional structural, thermal, dielectric, and chemical stability, make epoxy-based LC elastomers among the most investigated material for elastomer-based nanocomposites

Several parameters, such as type of monomer and curing agent, degree of curing, shape and thickness of the specimen, can affect the extent of actuation in polymer-based shape memory materials. Among them, the addition of micro- and nano-sized particles is a very attractive way to modulate the properties of materials, including SME. In this regard, nanoparticles are of particular interest, as they possess a very high surface to volume ratio, which enables the creation of a large interfacial area between matrix and filler. As it is explained in the following, this hybrid materials are called polymer-based nanocomposites.

Besides these fundamental studies, SMPs find also technological application. Thanks to their promising properties, medical devices for surgery and biomedical engineering are produced, likewise sensors and aerospace equipment. For some of these applications, is also increasing the demand of rapid prototyping. For this reason, some studies are now

addressing the realization of 3D printed SMPs items. As an example, CRG group has developed a filament which combines SME with 3D printing.

1.5. Shape Memory Hybrids (SMH)

Shape memory hybrids are not proper SMM, but most, can be considered as a "home-made" SMM, since the starting materials do not show any SME, but their interaction can give birth to a responsive material. For example, a SMH can emulate a SMP. Taking silicone and wax, the first represents the elastic matrix, that stores the force, and the second is the part of the material that experiences the transition. When this hybrid is heated and compressed, the silicon stores a strain, and the melted wax flows, following the strain. Then, when the system is cooled down, wax solidifies and the silicone stands in this shape. Reheating the whole sample, wax is melted again and the silicon can switch back to its original shape. [35,78]

Just like SMPs, SMHs can exhibit SME in different ways, induced by heating or solvent dissolution, depending on which are the chosen components for the matrix or for the inclusion among metals, organic or inorganic compounds.

For this kind of material, it is possible to predict its final behavior, since the selected components maintain their physical-chemical characteristics. Also aging, relaxation and fatigue can be easily controlled, thanks to the chemical interactions between the matrix and the inclusion.

1.6. Shape Memory Polymer Composites (SMPC)

Shape memory polymer composites (SMPCs) are hybrid materials made of at least two phases: a polymer matrix and a dispersed phase, usually in fibrous or particulate form. Since each phase has its own physic-chemical properties, composites are not homogeneous materials. This inhomogeneity arises from the discontinuity between the phases. However, the two phases establish physical or chemical interactions, giving rise to a significant improvement in several parameters, such as mechanical performance, barrier properties, flammability, etc. In the case of SMPC, at least one of the two phases is made of a SMM. Herein, shape memory composites based on SMPs constituting the continuous phase are reported.

One of the main reasons accounting for the introduction of fillers in SMP is due to their intrinsic low mechanical strength and shape recovery stress. Selecting the proper particle, and the right concentration, it is possible to improve the mechanical behavior and the stress applied by the SMPC upon the shape recovery process. Microfibers, mat and fabrics, as well as carbon based particles can improve the bearable mechanical load, where exfoliated nanoclay and ceramics particles enhance the SME.

As shown in SMP section, temperature is by far the most employed stimulus able to trigger the SME. However, thanks to the right choice of fillers, it is possible to obtain SME by the exploitation of different stimuli, depending on their interaction with the SMP matrix. Indeed, is possible to observe what is called “athermal” SME. [79] This kind of stimuli-active effect is one of the most studied in recent decades, since it allows to control the switch

even from remote. It can be triggered not by rising the temperature of the environment, but with the application of a radiation or an electric field provided that conductive particles are embedded in the sample. The applied voltage induces a current in the sample that is intrinsically heated due to the Joule effect. Typically, carbon-based particles or a metal powder can trigger this effect.

Other possibilities to obtain athermal SME have been demonstrated, [79] such as magnetically-activated SMPs, in which ferromagnetic particles or silica-surface-modified ceramics particles are included, in order to induce thermomagnetically-induced SME. [80] Additionally, SME can be also water-promoted, if hydrophilic particles or water-active cellulose are used as fillers. [81] A SMP can become a photo-responsive SMPC, if particles that photo-dimerize when hit by infrared (IR) light are dispersed within the SMP. [82]

Besides the common SME, many recent studies report on the possibility of enabling a multiple-shape memory effect (MSME). [83] This arises when two different SMM are connected into one, with each of them keeping its own SME. This can be achieved not only choosing the right filler, but it can also be observed in those polymer blends or layered composites (laminates) in which the two chosen material, are, in fact, distinct SMPs, with well separated switching. [84]

In other cases, it is possible to observe a localized activation effect, thanks to a well-programmed distribution of the sensitive particles within the matrix. Those are the spatially controlled SMPCs. [85]

Recently, 2W-SMPCs were studied. They can be obtained, for example, embedding a pre-stretched LC SMP in an elastomeric matrix, in which the latter applies a stress on the SMP while reheated. [86] The same behavior is observed for laminates in which the elastomer layer responds to the SMP traction with an applied stress. [87] Another 2W-SMPC is the photo active class. This material switch from one shape to another thanks to the coupling of

azobenzene-based particles, characterized by a photo-induced cis-trans isomerization, with LCE. [88]

Among SMPCs, those with self-healing features represent an intriguing field of study. Up to now, SMPCs have enabled the intrinsic self-healing capability of SMPs, [89] even at macroscopic scale. [90] This happens if the SMP is modified with thermoplastic particles that heals the crack, where the SME cannot. An opposite approach can give similar result, including SMP fibres and thermoplastic particles into a thermoplastic bulk material. Also combining SMA and SMP makes possible to obtain a self-healing system, with the SMA operating as an armor for SMP. [91]

1.7. Shape Memory Nanocomposites

Nanocomposites take their name from the composites, as likewise they are characterized by the presence of at least two different phases thoroughly mixed. In general, a particulate or fibrous phase is embedded in a continuous matrix phase. Nanocomposites, unlike composites, are characterized by the nanometer-sized dimension of one of the phases that constitute the material, typically that in particulate form. Since each phase has its own physic-chemical properties, nanocomposites are thought as inhomogeneous materials. This inhomogeneity arises from the discontinuity between the phases, that is the interface, which may be responsible for several composite properties. Due to the very high surface area of the nanoparticles, the interface in nanocomposites is maximized, as it can be considered as a third phase that plays a paramount role in determining the final properties of the material.

In general, even if polymers exhibit very distinguishing properties, as pointed out above, some of their properties do not fit with the final use for which they had been considered. For example, in some cases a polymer works properly for its lightness, however it could be necessary to improve elastic modulus and strength, being the latter lower than metals and ceramics. One solution to improve these two parameters relies on including nanofillers, that allow achieving such an improvement. To this aim, fibers, filaments, platelets or particles, depending on the specific requirements are used, which help to manufacture lightweight materials that keep their typical versatility and processability. [92]

Of course, other than shape, chemical structure of the particle plays a key role in determining the properties of the final product. For example, if the sample is filled with rod-like cellulose nanofibers, [93] mechanical features and biocompatibility will be improved. On the other hand, if the polymer is filled with ceramic particles, for example halloysite nanotubes (HNTs), [94] the material will experience an improvement in mechanical properties, as well as in thermal stability. Metal nanoparticles can enhance optical or magnetical polarizability and chemical reactivity. [95] Besides these nanofillers, in recent years carbon-based are mostly used. They may improve thermal, mechanical and electrical properties, [96] even though may result in a lower biocompatibility, unless they are modified and compatibilized to stay in a biological environment. [97]

As shown in the following, the topic of this thesis encompasses the study of neat shape memory elastomers, as well as nanocomposites obtained using a SMEL as a matrix, in which carbon-based nanofillers were dispersed. The final material also showed SME. In the next sections, a review on the most used nanoparticles in polymer composites is given, along with a state of the art of the major classes of shape memory polymer nanocomposites (SMPNC).

1.7.1. Nanofillers

Commonly, the presence of a foreign body in a bulk material is considered as a defect, as any inhomogeneity can cause failures of the entire system. Therefore, to obtain a nanocomposite, that is a wholly new material from the two starting ones, the achievement of a homogeneous dispersion of the nanoparticles within the matrix is mandatory. Once the particles are evenly dispersed in a polymer matrix, a nanocomposite is obtained, the nanoparticles acting as nanofillers in the final product.

The term “nanofiller” indicates a particulate material having at least one dimension (length, width or height) lower than 100 nanometers. Nanofillers are often classified according to the number of dimensions that are below 100 nm. As an example (Figure 1.7), starting from a cube of 1 mm, if the height along the Z axis is reduced by 4 orders of magnitude down to 100 nm, it turns into a plate-like nanofiller (a 1D nanoparticle). Then, if the same is done for Y and X axes, a fibrous (2D) and a spherical (3D) nanofiller are obtained, respectively.[98]

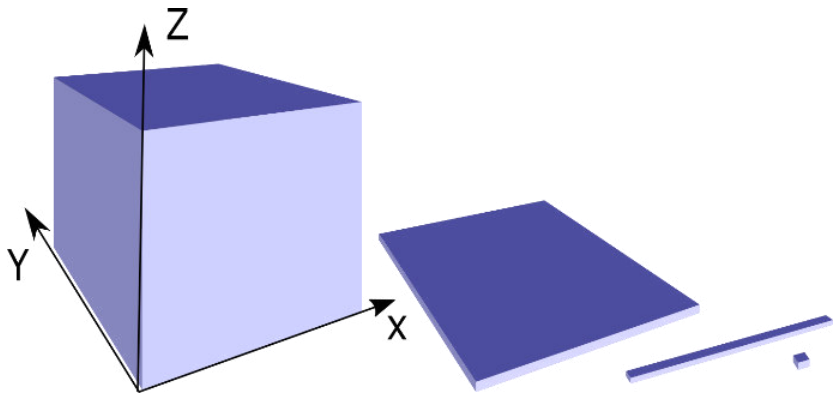

Figure 1.7 Schematic representation of a nanofiller

To fully exploit the potential of the interaction between nanofiller and polymer matrix, another consideration should be made. As already mentioned, in nanocomposites the interface between matrix and nanofiller plays a key role in dictating the properties of the material. Indeed, due to the small dimensions of nanofillers, the amount of atoms present on the surface is comparable with those underneath, and so are the energies respectively associated.[99] In order to reduce the surface energy, the nanofillers tend to agglomerate, mainly due to Van der Waals attractive forces, creating larger clusters. As a consequence, nanoparticles will not be well dispersed within the matrix, giving rise to a hardly predictable behavior of the obtained material, mostly in terms of mechanical and electrical properties. [100] Thus, tailoring the processing steps becomes necessary for a successful filler dispersion. Hereafter, a quick synopsis about most common nanofillers is reported.

Inorganic fillers. Silica particles are likely the most used inorganic nanoparticles. Usually, these fillers can be found in different morphologies, that is particles, nanotubes and platelets. The latter class is represented by clay nanoparticles [101], usually made of aluminosilicate inorganic materials. When dispersed in a polymer matrix, the stacking platelets could be exfoliated, and the layers totally separated one from another, or intercalated by the polymer chains, giving rise to a partial separation of the layers. [95] In general, the more they are exfoliated, the larger the enhancement of the required properties. Moreover, to achieve such a result, a modification of the particle surface properties is often performed, as to increase compatibility between filler and matrix.

In many cases, a surfactant is used to delaminate clays. On the broken edges of the particles, polar sites are situated. Those can be charged either positively or negatively by the adsorption of H^+ or OH^- ions, depending on the pH of the solution (the more is the acidity, the more the clay becomes positive). A specific surfactant can increase the clay's

surface charge. [95] Xu et al. [102] found that controlling the amount of cations released from the surfactant in the solution and their subsequent intercalation between layers of silica particles due to exchange with H^+ ions on clay surface, one can tune the clay dispersion. Also the polymer matrix can actively affect the dispersion grade, as pointed out by Okamoto et al. [103] Surface modification has been also reported for 3D silica nanoparticles, in order promote their dispersion and to reduce flocculation and aggregation. Jana et al. [104] managed to modify the silica surface, fuming it and introducing –OH groups, in order to let it react with the polymer matrix epoxy groups in thermosetting polymers. However, depending on the nature of filler and matrix, surface modification may not be necessary. As an example, Yudin et al. [105] produced systems including magnesium hydrosilicate nanotubes without any surfactants or surface modifications.

Another important class of inorganic fillers is represented by the metal-based nanoparticles. Their use can enable several magnetic, electrical and optical properties. [95] The use of pure metal nano-sized particles has been widely reported. Rutnakornpituk et al. [106] used cobalt for creating stable amphiphilic polysiloxane triblock copolymer micelles, starting from solution with surfactant and toluene. Rong et al. [107] obtained silver nanoparticles starting from silver salt, using sol-gel microemulsion techniques, to prepare core-shell colloid wires, where the core consisted in silver nanoparticles. Metal oxides are also widely used as nanoparticles. Yang et al. [108] prepared TiO_2 nanoparticles, that were added to the precursor solution of phenylenevinylene (PPV), in order to get surface-modified TiO_2 nanoparticles well interacting with the polymer matrix.

Organic fillers. The most used organic filler is cellulose, used in many kinds of shapes and fields. Mainly, it is used for mechanical reinforcement, since is characterized by high crystallinity, high Young modulus and resistance [109,110] Yu et al. [111] reported about enhanced dispersion of cellulose nanocrystals (CNCs), obtained from microcrystalline cellulose (MCC),

in chloroform, and then in the chosen polymer matrix. Dufresne et al. [112] also employed film casting of cellulose-polymers materials, using water dispersions. To obtain such result, surfactants [113] or surface modification strategies were employed. [114]

Carbon-based fillers. In recent years, a lot of carbon-based nanofillers have been described. According to the above-reported classification, 1D plate-like carbon nanoparticles are known as graphene, carbon nanotubes are 2D particles, while spherical, 3D carbon nanoparticles are called fullerenes. These kinds of fillers are used in order to enhance some properties, such as mechanical or physical ones, or to enable new properties the neat material would not exhibit, like electric conductivity. [115]

Graphite is made of many graphene nanosheets. It is the lower cost carbon-based filler available, and it has been used essentially to create conductive composites. However, when in graphite form, the percent amount needed to reach the percolation threshold is very high, resulting in poor mechanical properties. Graphite nanoplatelets (GNP) are produced by graphite partial exfoliation, resulting in discrete particles made up of few graphene layers, possibly enhancing the potential conductivity and strength of a GNP-polymer nanocomposite. [116] Apart from graphene based fillers, carbon nanotubes (CNTs) represent very promising 2D nanofillers. Likewise graphene, CNTs exhibit exceptional mechanical, thermal and electrical properties.

In general, many techniques may be used thanks to which graphitic materials are obtained. One of these is the chemical vapor deposition (CVD). With this method, a mixture of volatile carbon compounds are in a chamber where the temperature is very high, at atmospheric pressure. This procedure leads to the growth of carbon nanotube structures when metal nanoparticles are used. [117] Instead, Somani et al. [118] explained that, if the catalyst sites are metal foils, growth of graphene is obtained.

However, such good materials come with some contraindications. To see their properties applied, it is necessary to boost particle interaction with the surrounding polymer matrix. Since they are nanosized, it is very difficult to turn particles agglomerates into single ones, both for graphene and CNTs. In the case of graphene, the very first method to exfoliate these layers was a mechanical one, in which adhesive tape was used, by Novoselov et al. [119] when graphene was observed for the first time. Another exfoliation technique is the chemical one. Graphene has intrinsic chemical defects. This is due to the fact that it is a metastable structure, [120] made of sp^2 hybridized carbon atoms. The structural defects create saturated bonds that cause a change of hybridization to sp^3. It is possible to take advantage of such defects, creating a new kind of material, namely graphene oxide (GO), in which the hydrocarbon surface of graphene is grafted with reactive oxygen-based functional groups. This procedure may allow for graphene layer exfoliation. Stankovich et al. [121] used strong oxidizing agents, such as sulfuric acids followed by an ultrasonication, in order to exfoliate the layers. Other techniques includes the exfoliation by rapid evaporation of the solvent in which the graphene layers are dispersed, as Hernandez et al. [122] did.

CNTs have been discovered earlier than graphene. [123] For this reason, they are also more used and studied. Just like graphene, they can be single wall CNTs (SWCNTs), considered as a single sheet of graphene rolled up, and multi-walled CNTs (MWCNTs), in which many layers of graphene are rolled up one by one, in order to form a concentric system, with increasing radius. [115] The techniques to mix these nanofillers with polymer matrices are several. In the first place, they can be just mixed in a solution, with a suitable solvent for both nanofillers and matrix, and let it evaporate. [124] However, in this way the dispersion is not so efficient. To improve such aspect, Safadi et al. [125] used ultrasonication agitation, and Cui et al. [126] used a surfactant. With these methods, the integrity of the nanofiller may not

be preserved. Electrospinning CNTs with the polymer matrix has been also reported. [127] Despite being very simple, direct introduction of CNT in the polymer melt is usually less effective, [128] as the polymer is too viscous to tear the CNTs bundle apart. Another method for the dispersion of CNTs is the *in situ* polymerization. It works like a dispersion process, but without any solvents; the starting dispersion is made of monomer in which polymerization occurs, either with thermoplastic [129] or thermosetting [130] polymers.

Functionalization of CNTs is highly effective to avoid nanoparticles agglomeration. Also in this case, when the CNTs' surface atoms are involved in a chemical reaction, the hybridization of the reactive carbon changes from sp^2 to sp^3. Usually, the edge atoms are the most reactive. [131] Depending on the reagents chosen, it is possible to precisely select the functional groups that will be present on the CNT surface, such as carboxyl, alcohol [132] or amino groups. These obtained CNTs can be used for further reaction steps or inclusion in a polymer matrix, as they are more compatible with the organic phase.

1.7.2. Shape memory polymer nanocomposites filled with carbon-based fillers

Shape memory polymers represent a wide field, with many different ways to investigate in. An impressive amount of materials can be comprised in this category, and even higher possibilities arise when these material are used to obtain shape memory polymer nanocomposites. Hereafter, several examples of SMPNC are reported, sorted according to their main chemical structure, namely polyurethane-, styrene-, and epoxy-based SMPNCs.

1.7.2.1. Polyurethane-based SMPNC

SM polyurethanes have been the very first SMP ever studied in order to achieve a better comprehension of the SME. [133] Polyurethanes (PU) consist in a thermoplastic polymer with two different segments, namely a hard and a soft one (Figure 1.8). The hard segment is usually either a low molecular weight diisocyanate or a long chain macro diol diisocyanate characterized by high transition temperature. The reaction of these components with dihydroxy-terminated oligoesters or oligoethers affords a linear polyurethane. [134] The diisocyanate can exhibit both aliphatic or aromatic structure.

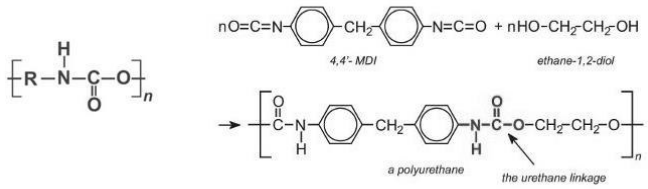

Figure 1.8 Polyurethane chemical structure

With each of these segments, a different semi-crystalline structure can be obtained. When diols or diamines are coupled with these monomers as chain extenders, a phase-segregated polyurethane block copolymer is obtained.

Such SMP can be used to design a SMPNCs, by the inclusion of nanoparticles within the matrix. In order to improve mechanical and to activate electrical conductivity, CNTs are the best choice. Cho et al. [135] used MWCNTs for this reason. First, the MWCNTs' surface was chemically modified by an acid treatment while sonication was going on. This was necessary to improve CNT interaction with the PU matrix, in order to get remarkable mechanical properties. Indeed, the higher the degree of surface modification, the better the properties achieved. Indeed, shape memory mechanical recovery increased, and so did

conductivity, giving rise to an electro-active composite. Choi et al. [136] used graphene dispersed within a SMP polyurethane-based matrix. The reinforcement effect due to graphene was achieved, thanks to the surface modification of the nanoparticles. However, this procedure lowered the shape memory effectiveness because the resulting conductivity of the nanoparticles was lowered, reducing the resistive heating effect.

1.7.2.2. Styrene-based SMPNC

In order to exhibit SME, a styrene-based polymer must have a cross-linked structure. Styrene-based SMPs are thermosetting polymers (Figure 1.9). They can be polymerized in different ways, since many monomers, mechanism or curing agents can give such arrangement.

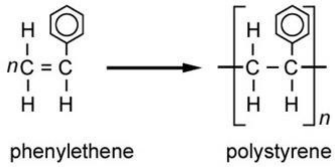

Figure 1.9 Example of styrene-based polymer

These structural features are provided by renewable natural oils, as found by Li et al. [137] Such oils led to formation of random copolymer networks, thanks to their high degree of unsaturation, through cationic polymerization with styrene. Since this network is present, it behaves like a SMP. It is possible to control the cross-link densities and the rigidity of the backbone to tune the Tg and mechanical properties, in view of the SME.

Yu et al. [138] produced a SMPNC using a styrene-based SMP and CNT. Their investigation concerned the possibility to use CNTs within the shape memory matrix as a triggering medium for the SME. The way they activated such effect involved microwave irradiation to heat the nanofillers, which acted as heating sources for the matrix, depending on the volume percentage of nanofillers and microwave intensity.

Up to now, very few studies, if any, involved graphene into styrene-based SMPNC. Much more works included other carbon nanoparticles, such as carbon black. Leng et al. [139] used such nanofiller to enhance the SME, using the response of the carbon-based particles to the infrared radiation, thanks to which the recovery rate was faster than the pristine sample, analyzed in the same work.

1.7.2.3. Epoxy-based SMPNC

Other than styrene-based SMP, also epoxy-based ones are thermosetting matrices widely used in the preparation of SMPNC (Figure 1.10).

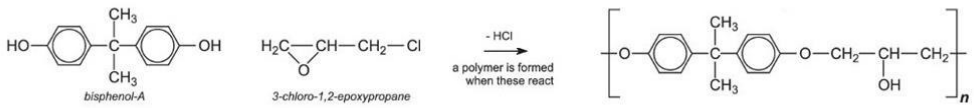

Figure 1.10 Epoxy-based resin

Kumar et al. [140] showed the different possibilities thanks to which is possible to obtain an epoxy-based SMP. To obtain such effect, they should present both crystalline (or liquid crystalline) and glass phases. The SME can be tailored just by changing the amount and the

composition of those that represent the thermally active reversible segment, even giving rise to triple-shape memory or self-healability behavior.

CNTs can be dispersed within the matrix, in order to enhance the SME. Liu et al. [141] produced a SMP system involving diglycidyl ether of bisphenol A (DGEBA) and methylhexahydrophtalic anhydride (MHHPA) in which different contents of MWCNTs were dispersed. They observed changes in characteristic temperatures, such as the glass transition (T_g), in the mechanical properties and in the subsequent SME, in relation to varying amounts of reagents and nanofillers. Mainly thanks to nanofillers, mechanical properties were strongly enhanced, likewise the recovery rate and the shape stability during the shape memory cycles.

Graphene is also used to activate new shape memory activation processes, like electrical trigger, in epoxy-based SMP. Wang et al. [142] used reduced graphene oxide paper to promote such behavior with resistive heating. The main result relevant to the shape memory effect was the increase of the recovery speed with increasing applied voltage.

1.8. Objective

Over these three years, the study of the doctoral program concerned the optimization of a functionalization strategy of carbon nanoparticles, in order to improve their dispersion within shape memory epoxy polymers, and the characterization of their effect on relevant properties of the matrix.

In detail, the main objective of the thesis is the realization of materials with tunable shape memory effect (SME), based on shape memory polymers (SMP), in which different kinds of carbonaceous nanofillers were dispersed. The chosen fillers were multiwalled

carbon nanotubes (MWCNT) and graphene oxide (GO). These two nanoparticles exhibit exceptional mechanical, electrical and chemical properties. However, a well-known problem arising from the use of these two nanoparticles, stands in their tendency to aggregate into clusters when dispersed in a polymer matrix. This could be detrimental to several properties, including thermal, mechanical, and shape memory behavior. Surface modification is a widely adopted strategy to overcome these drawbacks, therefore a part of the present work was devoted to chemical modification of MWCNT and GO, aimed to improve their compatibility with the polymer matrix.

GO was synthesized in our laboratory starting from graphite nanoplatelets (GNP), whereas carboxy-functionalized MWCNTs were purchased and then chemically modified. These nanoparticles were used as fillers at different weight percentages in epoxy-based shape memory liquid crystalline elastomers to obtain nanocomposites. To obtain a homogeneous dispersion and distribution of nanofillers within the matrix, a suitable compatibilization strategy was set up, involving the chemical functionalization of the carbonaceous nanofillers, to graft specific functional groups on their surface. The obtained materials were then characterized to evaluate the degree of functionalization.

The selected matrix consisted in an epoxy-based liquid crystalline (LC) elastomer, which is formed through reaction between a LC monomer and a dicarboxylic acid used as curing agent in presence of a catalyst. Neat resins were realized as a reference. All the obtained materials, cast as films, exhibited SME.

The latter were characterized in terms of mechanical, chemical, thermal and morphological properties. Moreover, the effect of the nanofillers on the thermomechanical behavior was elucidated.

These films may be used to produce thermo-responsive autonomous mechanical switch systems. Such device can be built-up as a multi-layered laminate, through the adhesion of

several layers made of different materials. A layer of the epoxy-based liquid crystalline elastomer in its temporary shape can be sandwiched between two layers of an amorphous epoxy-based material, which is cured around the first layer. During this curing process, the programmed LCE layer results to be embedded in the epoxy-based matrix, thanks to the interlayer adhesion between the two materials. In this way, when the device is heated above the Tg of the epoxy-based material, the LCE is able to recover its permanent shape, deforming the softened matrix. When the device is cooled down below the matrix Tg, the amorphous layer restrains the LCE material to the temporary shape, resulting in the thermally activated autonomous mechanical switching.

References

1 REZAEI, Soroosh Daqiqeh; SHANNIGRAHI, Santiranjan; RAMAKRISHNA, Seeram. A review of conventional, advanced, and smart glazing technologies and materials for improving indoor environment. *Solar Energy Materials and Solar Cells*, 2017, 159: 26-51.

2 JULIEN, Christian M., et al. Smart materials for energy storage in Li-ion batteries. *AIMS Materials Science*, 2016, 3.1: 137-148.

3 KHOO, Zhong Xun, et al. 3D printing of smart materials: A review on recent progresses in 4D printing. Virtual and Physical Prototyping, 2015, 10.3: 103-122.

4 QIU, Xiaoyun; HU, Shuwen. “Smart” materials based on cellulose: a review of the preparations, properties, and applications. Materials, 2013, 6.3: 738-781.

5 MURPHY, Erin B.; WUDL, Fred. The world of smart healable materials. Progress in Polymer Science, 2010, 35.1: 223-251.

6 JOCHUM, Florian D.; THEATO, Patrick. Temperature-and light-responsive smart polymer materials. Chemical Society Reviews, 2013, 42.17: 7468-7483.

7 YAVUZ, Mustafa S., et al. Gold nanocages covered by smart polymers for controlled release with near-infrared light. Nature materials, 2009, 8.12: 935-939.

8 GIORGIO, Ivan, et al. Piezo-electromechanical smart materials with distributed arrays of piezoelectric transducers: current and upcoming applications. International Journal of Applied Electromagnetics and Mechanics, 2015, 47.4: 1051-1084.

9 THÉVENOT, Julie, et al. Magnetic responsive polymer composite materials. Chemical Society Reviews, 2013, 42.17: 7099-7116.

10 KIM, Miso; DUGUNDJI, John; WARDLE, Brian L. Efficiency of piezoelectric mechanical vibration energy harvesting. Smart Materials and Structures, 2015, 24.5: 055006.

11 LEFEBVRE, Esther, et al. Smart materials: development of new sensory experiences through stimuli responsive materials. In: A Matter of Design. Making Society through Science and Technology. 2014.

12 Ye Zhou and Wei Min Huang / Procedia IUTAM 12 (2015) 83 – 92

13 W.M. Huang , Z. Ding, C.C. Wang, J. Wei, Y. Zhao, H. Purnawali, Materials Today JULY-AUGUST 2010 | VOLUME 13 | NUMBER 7-8

14 Smart Mater. Struct. 23 (2014) 023001 Topical Review, Yanju Liu, Haiyang Du, Liwu Liu and Jinsong Leng

15 A. Lendlein and S. Kelch Angew. Chem. Int. Ed. 2002, 41, 2034 ± 2057

16 HEARON, Keith, et al. A processable shape memory polymer system for biomedical applications. Advanced healthcare materials, 2015, 4.9: 1386-1398.

17 BARBARINO, Silvestro, et al. A review on shape memory alloys with applications to morphing aircraft. Smart Materials and Structures, 2014, 23.6: 063001.

18 PENG, Qingyu, et al. Shape-memory polymer nanocomposites with a 3D conductive network for bidirectional actuation and locomotion application. Nanoscale, 2016, 8.42: 18042-18049.

19 NIKDEL, Nazila, et al. Using neural network model predictive control for controlling shape memory alloy-based manipulator. IEEE Transactions on Industrial Electronics, 2014, 61.3: 1394-1401.

20 Duerig, Thomas W., K. N. Melton, and D. Stöckel. Engineering aspects of shape memory alloys. Butterworth-Heinemann, 2013

21 ARNE OLANDER VOl. 54, SOLID CADMIUM-GOLD ALLOYS, 3819-33, 1932

22 Plastic Deformation and Diffusionless Phase Changes in Metals-The Gold-Cadmium Beta Phase Chang, L. C.Read, T. A., Trans. AIME. Vol. 189, p. 47 (1951)

23 Effect of Low-Temperature Phase Changes on the Mechanical Properties of Alloys near Composition TiNi, W. J. Buehler, J. V. Gilfrich, and R. C. Wiley, 1962

24 The Chemical Educator, June 1997, Volume 2, Issue 2, pp 1–21, The Story of Nitinol: The Serendipitous Discovery of the Memory Metal and Its Applications

25 Vernon LB, Vernon HM. Process of manufacturing articles of thermoplastic synthetic resins. In: US Patent 2234993; 1941.

26 J Mater Sci (2016) 51:10663–10689, Morphing in nature and beyond: a review of natural and synthetic shape-changing materials and mechanisms, Kate Oliver1, Annela Seddon1,2,* , and Richard S. Trask3

27 Red blood cell as an adaptive optofluidic microlens, L. Miccio, P. Memmolo, F. Merola, P.A. Netti & P. Ferraro, nature communications

28 Francesco Merola, Pasquale Memmolo, Lisa Miccio, Roberto Savoia, Martina Mugnano, Angelo Fontana, Giuliana D'Ippolito, Angela Sardo, Achille Iolascon, Antonella Gambale and Pietro Ferraro. Tomographic Flow Cytometry by Digital Holography. Light: Science & Applications accepted article preview 17 October 2016

29 VAN HUMBEECK, Jan. Non-medical applications of shape memory alloys. Materials Science and Engineering: A, 1999, 273: 134-148.

30 FREMOND, Michel; MIYAZAKI, Shūichi. Shape memory alloys. Springer, 2014.

31 NATURE OF THE MULTISTAGE TRANSFORMATION IN SHAPE MEMORY ALLOYS UPON HEATING, Metal Science and Heat Treatment, Vol. 51, Nos. 11 – 12, 2009, L. Sun and W. M. Huang

32 Duerig, Pelton, Materials Properties Handbook Titanium Alloys pp. 1035-1048, 1994

33 Huang et al., JOURNAL OF MATERIALS SCIENCE LETTERS 19, 2000, 1549 – 1550

34 Ma et al., Int Mater Rev 2010;55:257–315.

35 Sun et al., Materials and Design 33 (2012) 577–640

36 OTSUKA 1999, Cambridge University Press, Shape memory materials

37 Buehler et al., Ocean Engineering Volume 1, Issue 1, July 1968, Pages 105-108, IN7-IN10, 109-120

38 Liu, In: Shape Memory Alloys, Editor: H. R. Chen, pp. 361-369, 2010, Nova Science Publishers, Inc., Chapter 13

39 JANI, Jaronie Mohd, et al. A review of shape memory alloy research, applications and opportunities. Materials & Design, 2014, 56: 1078-1113.

40 Stockel 1995, THE SHAPE MEMORY EFFECT, NDC, Nitinol Devices & Components, Inc., Fremont, CA

41 Hartl et al., Thermomechanical Characterization of Shape Memory Alloy Materials, 2008, in Shape Memory Alloys, Lagoudas ed.

42 Mihalcz, PERIODICA POLYTECHNICA SER. MECH. ENG. VOL. 45, NO. 1, PP. 75–86 (2001)

43 Sreekumar et al., Materials and Design 30 (2009) 3020–3029

44 Simha, J. Mech. Phw Solids, Vol. 45, No. 2, 261-292, 1997

45 Reyes-morel et al., J. Am. Cerum. Soc., 71 [8] 648-57 (1988)

46 Itoh et al., J. Japan Inst., Metals, Vol.52, No.5 (1988), 523-528

47 Schurch et al., Nature, Vol. 266, 706-7 (1977)

48 Itoh et al., J. Japan Inst., Metals, Vol.54, No.1 (1988), 117-124

49 Heuer, (1990), On the Thermoelastic Martensitic Transformation in Tetragonal Zirconia. Journal of the American Ceramic Society, 73: 1084–1093

50 Swain, Nature, Vol. 322, 234-6 (1986)

51 Jin, Current Opinion in Solid State and Materials Science 9 (2005) 313–318

52 Uchino, Actuators 2016, 5, 11

53 Cross, Journal of Intelligent Material Systems and Structures, Vol. 6 (1995), 55-61

54 Morozof, Thesys on Softening and hardening transitions in ferroelectric Pb(Zr,Ti)O3 ceramics, 2005

55 Wei et al., JOURNAL OF MATERIALS SCIENCE 33 (1998) 3743 — 3762

56 Pan et al., J. Appl. Phys. 66 (12), 6014 (1989)

57 Troyanchuk et al., Phys. Stat. Sol. (a) 157, 159 (1996)

58 FURUTA, Atsushi, OH, K.-Y., UCHINO, Kenji, (1990), IEEE 7th International Symposium on. IEEE, 1990. p. 528-529

59 CHEN, Hongmei, et al. Highly pH-sensitive polyurethane exhibiting shape memory and drug release. Polymer Chemistry, 2014, 5.17: 5168-5174.

60 SHI, Ying; YOONESSI, Mitra; WEISS, R. A. High temperature shape memory polymers. Macromolecules, 2013, 46.10: 4160-4167.

61 XIE, Meihua, et al. Strong electroactive biodegradable shape memory polymer networks based on star-shaped polylactide and aniline trimer for bone tissue engineering. ACS applied materials & interfaces, 2015, 7.12: 6772-6781.

62 Patterson et al., Solvent shrinkable polymeric material. U.S. Patent No 3,429,794, 1969.

63 Beloshenko et al., Russian Chemical Reviews 74 (3) 265 - 283 (2005)

64 Huang et al., Materials and Design 23 Ž2002. 1119

65 Ji et al., Smart Mater. Struct. 15 (2006) 1547–1554

66 Rousseau et al., J.Mater.Chem., 2010, 20, 3431–3441

67 Rousseau et al., J. AM. CHEM. SOC. 9 VOL. 125, NO. 50, 2003 15300

68 Yu et al., Macromol. Chem. Phys. 2005, 206, 1705–1708

69 Capadona et al., Science 2008, 319., 370-4

70 Sadhan K. De, Jim R. White, Rubber Technologist's Handbook, Volume 1, 2001

71 ZENTEL, Rudolf. Liquid crystalline elastomers. Advanced Materials, 1989, 1.10: 321-329.

72 Mark Warner, Eugene Michael Terentjev, Liquid Crystal Elastomers, 2007

73 Hölter et al., Macromolecules 1996, 29, 7003 - 7011

74 Ohm et al, Adv. Mater. 2010, 22, 3366–3387

75 Sue et al., *Polymer* Vol. 39 No. 20, pp. 4707-4714, 1998

76 Yi et al., J Therm Anal Calorim (2014) 117:481–488

77 Azoug et al., Polymer 98 (2016) 165-171

78 Fan et al., eXPRESS Polymer Letters Vol.5, No.5 (2011) 409–416

79 H. Meng, G. Li, Polymer 54 (2013) 2199-2221

80 He et al., Adv. Mater. 2011, 23, 3192–3196

81 Luo et al., Journal of Applied Polymer Science, Vol. 125, 657–665 (2012)

82 Small et al., Optics Express 2005;13:8204-13

83 Ahn et al., Adv. Funct. Mater. 2011, 21, 4543–4549

84 Cuevas et al., SoftMatter, 2012,8, 4928–4935

85 HRIBAR ET AL., ACS Nano.VOL.5, NO. 4, 2948–2956

86 Westbrook et al., Smart Mater. Struct. 20 (2011) 065010

87 Chen et al., Materials Letters 62 (2008) 4088–4090

88 Ikeda et al., Angew. Chem. Int. Ed. 2007, 46, 506 – 528

89 Xiao et al., J.Mater.Chem., 2010, 20, 3508–3514

90 G. Li, D. Nettles, Polymer 51 (2010) 755–762

91 Kirkby et al., Adv. Funct. Mater. 2008,18, 2253–2260

92 J. Jordan et al., Materials Science and Engineering A 393 (2005) 1–11

93 Favier et al., Macromolecules 1996,28, 6365-6367

94 M. Liu et al., Progress in Polymer Science 39 (2014) 1498–1525

95 SUPOVA et al., Sci. Adv. Mater. 2011, Vol. 3, No. 1

96 Kim et al., Macromolecules 2010, 43, 6515–6530

97 WANG, Wei, et al. Carbon nanotubes reinforced composites for biomedical applications. BioMed research international, 2014, 2014.

98 AJAYAN, Pulickel M.; SCHADLER, Linda S.; BRAUN, Paul V. Nanocomposite science and technology. John Wiley & Sons, 2006.

99 Krishnamoorti et al., J Polym Sci Part B: Polym Phys 45: 3252–3256, 2007

100 BORISENKO, Victor E.; OSSICINI, Stefano. What is what in the Nanoworld: A Handbook on Nanoscience and Nanotechnology. John Wiley & Sons, 2013.

101 Devi et al., International Journal of Advanced Engineering Research and Technology (IJAERT) Volume 4 Issue 7, July 2016, ISSN No.: 2348 –8190

102 Xu et al., Environ. Sci. Technol. 1995, 29, 312-320

103 M. Okamoto et al., Polymer 42 (2001) 1201±1206

104 Jana et al., Polymer 42 (2001) 6897-6905

105 V.E. Yudin et al., Polymer 48 (2007) 1306e1315

106 Rutnakornpituk et al., Polymer 43(2002) 2337-2348

107 Rong et al., Polymer 40 (1999) 6169–6178

108 Yang et al., Materials Chemistry and Physics 83 (2004) 334–339

109 Liu et al., Bioresource Technology 101 (2010) 5685–5692

110 Eichhorn et al., J Mater Sci (2010) 45:1–33

111 Yu et al., Carbohydrate Polymers 89 (2012) 971– 978

112 Dufresne et al., POLYMER COMPOSITES, APRIL 1997, Vol. 18, No. 2

113 Kviev et al., Appl. Phys. A 87, 641–643 (2007)

114 Yuan et al., Biomacromolecules 2006, 7, 696-700

115 Mittal et al., Journal of Industrial and Engineering Chemistry 21 (2015) 11–25

116 Seyller et al., Phys. Stat. Sol. (b) 245, No. 7, 1436–1446 (2008)

117 Zhao et al., Journal of Industrial and Engineering Chemistry 17 (2011) 218–222

118 P.R. Somani et al., Chemical Physics Letters 430 (2006) 56–59

119 NOVOSELOV, Kostya S., et al. Electric field effect in atomically thin carbon films. science, 2004, 306.5696: 666-669

120 Marnham et al., PHYSICAL REVIEW B 92, 085409 (2015)

121 Stankovich et al., Carbon 45 (2007) 1558–1565

122 HERNANDEZ, Yenny, et al. High-yield production of graphene by liquid-phase exfoliation of graphite. Nature nanotechnology, 2008, 3.9: 563-568.

123 IIJIMA, Sumio. Helical microtubules of graphitic carbon. nature, 1991, 354.6348: 56.

124 Du et al, Journal of Polymer Science: Part B: Polymer Physics, Vol. 41, 3333–3338 (2003)

125 Safadi et al., Journal of Applied Polymer Science, Vol. 84, 2660–2669 (2002)

126 CUI, S., et al. Characterization of multiwall carbon nanotubes and influence of surfactant in the nanocomposite processing. Carbon, 2003, 41.4: 797-809.

127 SON, Seung Uk, et al. Facile synthesis of various phosphine-stabilized monodisperse palladium nanoparticles through the understanding of coordination chemistry of the nanoparticles. Nano Letters, 2004, 4.6: 1147-1152.

128 Quian et al., Appl. Phys. Lett., Vol. 76, No. 20, 15 (2000)

129 WU, Tzong-Ming; LIN, Shih-Hsiang. Synthesis, characterization, and electrical properties of polypyrrole/multiwalled carbon nanotube composites. Journal of Polymer Science Part A: Polymer Chemistry, 2006, 44.21: 6449-6457.

130 MOISALA, A., et al. Thermal and electrical conductivity of single-and multi-walled carbon nanotube-epoxy composites. Composites science and technology, 2006, 66.10: 1285-1288.

131 AJAYAN, P. M., et al. Opening carbon nanotubes with oxygen and implications for filling. Nature, 1993, 362.6420: 522-525.

132 HUSSAIN, Shahir, et al. Spectroscopic investigation of modified single wall carbon nanotube (SWCNT). Journal of Modern Physics, 2011, 2.06: 538.

133 S. Hayashi Technical report on preliminary investigation of shape memory polymers, Nagoya research and development center, Mitsubishi Heavy Industries Inc (1990)

134 Chen et al., Journal of Polymer Science: Part B: Polymer Physics, Vol. 45, 444–454 (2007)

135 CHO, Jae Whan, et al. Electroactive shape-memory polyurethane composites incorporating carbon nanotubes. Macromolecular Rapid Communications, 2005, 26.5: 412-416.

136 CHOI, Jin Taek, et al. Shape memory polyurethane nanocomposites with functionalized graphene. Smart Materials and Structures, 2012, 21.7: 075017.

137 LI, Fengkui; LAROCK, Richard C. New soybean oil–styrene–divinylbenzene thermosetting copolymers. I. Synthesis and characterization. Journal of Applied Polymer Science, 2001, 80.4: 658-670.

138 Kai Yu et al, 2014, RSC Advances, 4, 2961

139 LENG, Jinsong; WU, Xuelian; LIU, Yanju. Infrared light-active shape memory polymer filled with nanocarbon particles. Journal of applied polymer science, 2009, 114.4: 2455-2460.

140 K.S. Santhosh Kumar et al., Reactive & Functional Polymers 73 (2013) 421–430

141 LIU, Yayun, et al. High performance shape memory epoxy/carbon nanotube nanocomposites. ACS applied materials & interfaces, 2015, 8.1: 311-320.

142 W. Wang et al., Composites Science and Technology 106 (2015) 20–24

CHAPTER 2

Surface modification of multiwalled carbon nanotubes (MWCNTs)

2.1. Introduction

Since their discovery in 1991, carbon nanotubes (CNT) have generated great interest due to their field emission and electronic transport properties, their high mechanical strength and their chemical properties.

With 100 times the tensile strength of steel, thermal conductivity better than all but the purest diamond, and electrical conductivity similar to copper, but with the ability to carry much higher currents, CNT are nowadays one of the most relevant building blocks of nanotechnology. [1]

CNT are long cylinders of covalently bonded carbon atoms. The ends of the cylinders may or may not be capped by hemifullerenes. In general, the end part of the cylinder is the result of pentagon inclusion in the hexagonal carbon network of the nanotube walls during the growth process.

There are two basic types of CNT: singlewalled carbon nanotubes (SWCNT) and multiwalled carbon nanotubes (MWCNT). Figure 2.1 reports a schematics of the kind of CNT available.

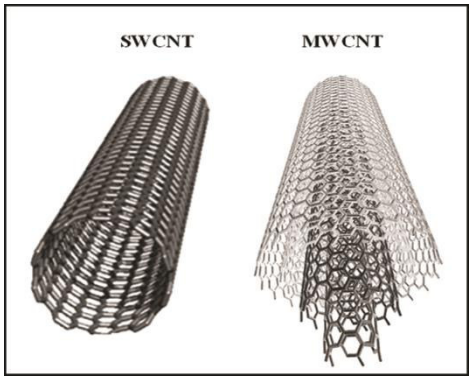

Figure 2.1 Schematic representation of a SWCNT and a MWCNT

SWCNT can be considered as single graphene sheets (graphene is a monolayer of sp^2-bonded carbon atoms) rolled into seamless cylinders. The carbon atoms in the cylinder have a partial sp^3 character that increases as the radius of curvature of the cylinder decreases. SWCNT have typical diameters of ~1 nm, with the smallest diameter reported to date of 0.4 nm [2]. This corresponds to the theoretically predicted lower limit for stable SWCNT formation based on consideration of the stress energy built into the cylindrical structure of the SWCNT.

MWCNT consist of nested graphene cylinders coaxially arranged around a central hollow core with interlayer separations of ~0.34 nm, indicative of the interplane spacing of graphite [3]. MWCNT tend to have diameters in the range 2–100 nm. MWCNT can be considered as a mesoscale graphite system, whereas the SWCNT is truly a single large molecule [1].

Carbon nanotubes possess high flexibility, low mass density, and large aspect ratio (typically ca. 300-1000). CNT have a unique combination of mechanical, electrical, and thermal properties that make nanotubes excellent candidates in the fabrication of multifunctional polymer nanocomposites. For example, theoretical and experimental results on individual SWCNT show extremely high tensile modulus (640 GPa to 1 TPa) and tensile strength (150-180 GPa).

There are several ways of preparing CNTs:

Arc-discharge method – This is the first method of preparation of CNT. This method enables producing MWCNT through arc-vaporization of two graphite rods placed end to end, separated by approximately 1 mm, in an enclosure usually filled with inert gas (helium, argon) at low pressure (between 50 and 700 mbar). After applying a DC arc voltage between two separated graphite rods by modifying apparatus for producing SiC powder, the evaporated anode generates fullerenes in the form of soot in the chamber, and part of

the evaporated anode is deposited on the cathode. When a graphite rod containing a metal catalyst (e.g., Fe and Co) is used as the anode and the cathode is pure graphite, SWCNT are generated instead of MWCNT. In figure 2.2, a schematic representation of arc discharge method for CNT production.

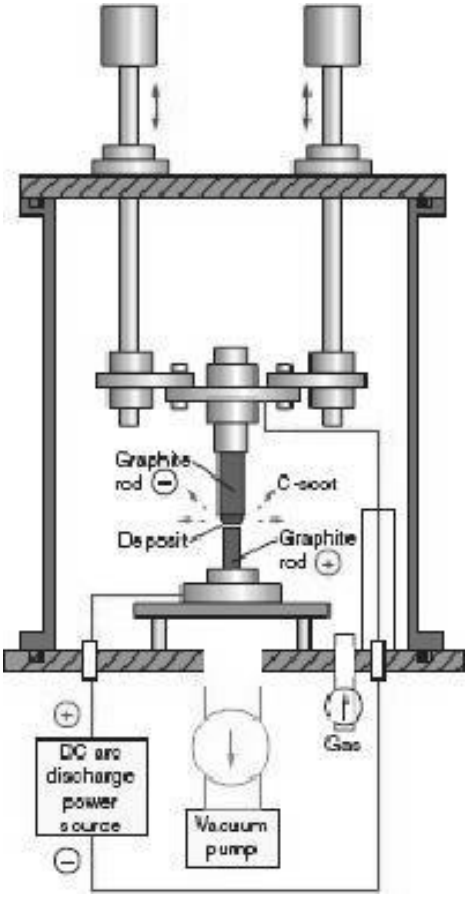

Figure 2.2 Schematic representation of arc discharge method to produce CNT

Laser-furnace method (or laser ablation) – This method was originally used as a source of metal clusters and ultrafine particles. It was then developed for fullerene and CNT production because it is suitable for materials with a high boiling temperature, such as carbon, as the energy density of lasers is much higher than that of other vaporization devices. This method involves a CO_2 laser beam, introduced onto the target (carbon composite doped with catalytic metals) located in the center of a quartz tube furnace.

Then, the target is vaporized in a high-temperature argon atmosphere and SWCNT are formed, that are conveyed by the gas to a special collector. The method has several advantages, such as the high quality of the diameter and controlled growth of the SWCNT. Changes of the furnace temperature, catalytic metals and flow rate directly affect the SWCNT diameter. The machinery is represented in Figure 2.3.

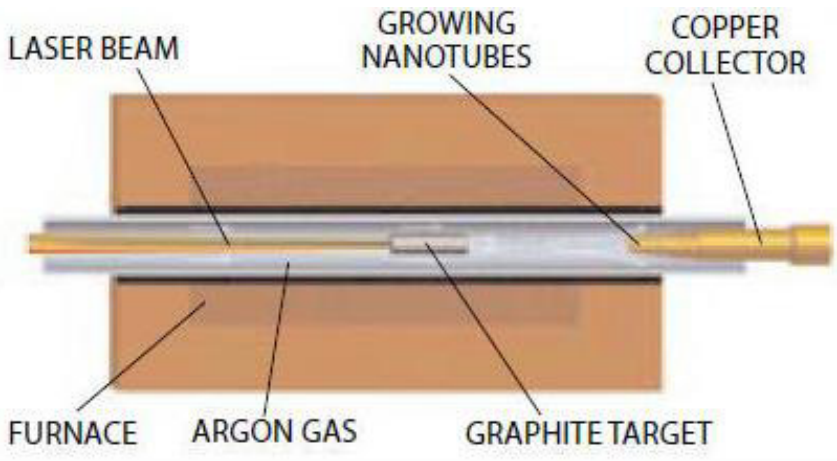

Figure 2.3 Schematic representation of the laser ablation method to produce CNT

Chemical-vapor deposition (CVD) – With this method it is possible to control the location and the alignment of the synthesized CNT. CVD uses hydrocarbon vapor (e.g., methane) that is thermally decomposed in the presence of a metal catalyst. The gas-phase molecules are decomposed to reactive species, leading to film or particle growth. CVD allows the synthesis of CNT at low temperature and ambient pressure, at the cost of crystallinity. CVD has been used for producing carbon filaments and fibers since 1959. The process involves passing a hydrocarbon vapor through a tube furnace in which a catalyst material is present at sufficiently high temperature to decompose the hydrocarbon. CNT grow over the catalyst and are collected on cooling the system to room temperature. CNT have also been successfully synthesized using organometallic catalyst precursors. The three main parameters for CNT growth in CVD are type of hydrocarbon, type of catalyst and growth

temperature. Apart from large-scale production, CVD also offers the possibility of producing single CNT for use as probe tips in atomic force microscopy (AFM). The tips produced are smaller than mechanically assembled ones, thus significantly improving the resolution of AFM [1]. A representation of the structure of this system is outlined in Figure 2.4.

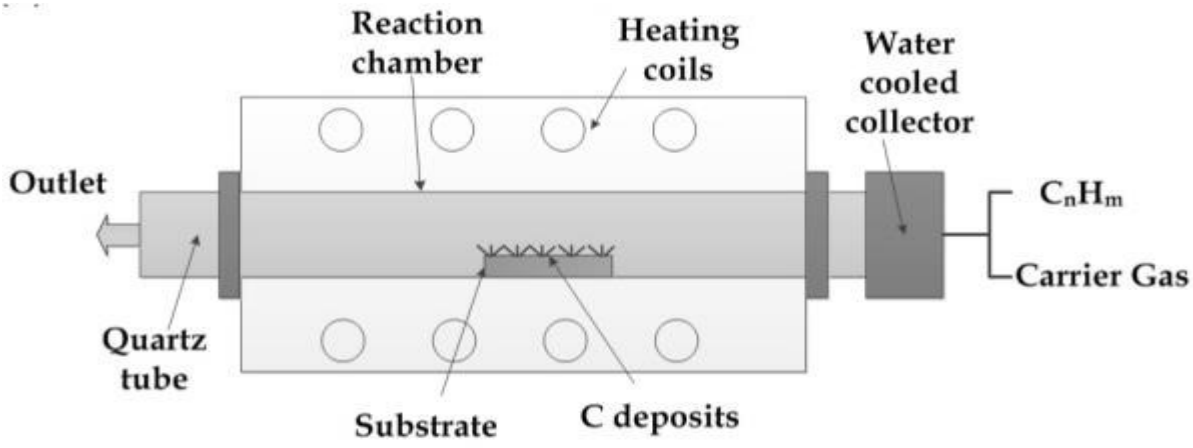

Figure 2.4 Schematic representation of the laser ablation method to produce CNT

Generally, in fibrous polymer nanocomposites, dispersion of the nanoparticle and adhesion at the particle–matrix interface play crucial roles in determining the mechanical properties of the nanocomposite. Without proper dispersion, the nanomaterial may not offer improved mechanical properties over that of conventional composites. Furthermore, a poorly dispersed nanomaterial may degrade the mechanical properties. Additionally, optimizing the interfacial bond between the particle and the matrix, it is possible to tailor the properties of the overall composite, similar to what is done in macrocomposites but using very low amount of nanofiller [4].

In this frame, the main problem is the creation of a good interface between nanotubes and the polymer matrix, to attain a good load transfer from the matrix to the nanotubes, during the application of a mechanical stress. The reason for this is essentially two-fold.

First, nanotubes are atomically smooth and have nearly the same diameters and aspect ratios as polymer chains (this is true in particular for SWCNT). Second, nanotubes are mostly organized into aggregates, which behave differently in response to an applied load as compared to an individual CNT. [5]

In order to maximize the advantage of nanotubes as reinforcing structures in high strength composites, the aggregates need to be broken up and well dispersed into the matrix. In addition, in most cases the surface of nanotubes has to be chemically modified (or functionalized) to achieve strong interfaces with the surrounding polymer chains.

Local strain in carbon nanotubes, which arises from pyramidalization and misalignment of the π-orbitals of the sp2-hybridized carbon atoms, makes nanotubes more reactive than a flat graphene sheet, thereby paving the way to covalently attach chemical species to nanotubes. This covalent functionalization of nanotubes can improve nanotube dispersion in solvents and polymers. Furthermore, covalent functionalization can provide a means for engineering the nanotube/polymer interface for optimal composite properties [3].

Suitable strategies are strictly required to improve the CNT compatibility and dispersibility, and to achieve the formation of homogeneous polymer based nanocomposites with improved polymer-filler interfacial adhesion. Different approaches have been used to improve the dispersion of carbon nanofillers into a polymer phase, including sonication [6], high-speed mixing [7],[8],[9] and calendering [10]. Other methods are based on non-covalent or covalent CNT surface functionalization. Among non-covalent, surfactant treatments [11], as well as polymer wrapping [12],[13] have been adopted. However, these methods often require complex processes. Concerning covalent surface functionalization methods, these are usually based on the grafting of low molecular weight compounds or polymer chains directly on the surface of carbon nanofillers [14],[15],[16]. Other covalent modifications are based on the incorporation of oxygen-containing functional

groups onto the CNT surface through a variety of methods, chiefly wet chemical oxidation [17,18,19,20] and plasma treatments [21].

Herein is presented the setup of an effective compatibilization strategy, able to improve the interfacial adhesion between a polymer matrix and CNT, and to promote a homogeneous dispersion of the carbonaceous nanofillers in an epoxy elastomer, aimed to the preparation of CNT nanocomposites to be applied as shape memory materials.

2.2. Experimental

2.2.1. Materials

Pristine CVD-grown multiwalled carbon nanotubes (MWCNT) and carboxyl-functionalized multiwalled carbon nanotubes (MWCNT-COOH), COOH content 0.7 wt%, were purchased from Cheap Tubes Inc. (Brattleboro, VT, USA). In Table 2.1 the main properties of MWCNT and MWCNT-COOH are reported.

Table 2.1: Main properties of MWCNT and MWCNT-COOH

Outer Diameter	30-50nm
Inside Diameter	5-10nm
Ash	<1.5 wt
Purity	>95 wt%
Length	10-20um
Specific Surface Area	60 m2/g
Electrical Conductivity	>100 S/cm

Two epoxy monomers were selected as CNT surface modifiers. Diglycidyl ether of bisphenol-A (EPON), number-average molecular weight M_n = 348 g/mol, was obtained from Sigma-Aldrich and used as received. *p*-bis(2,3-epoxypropoxy)-α-methylstilbene (DOMS) was prepared according to the synthetic procedure described in [22]. In Figure 2.5 schematic formulas are reported.

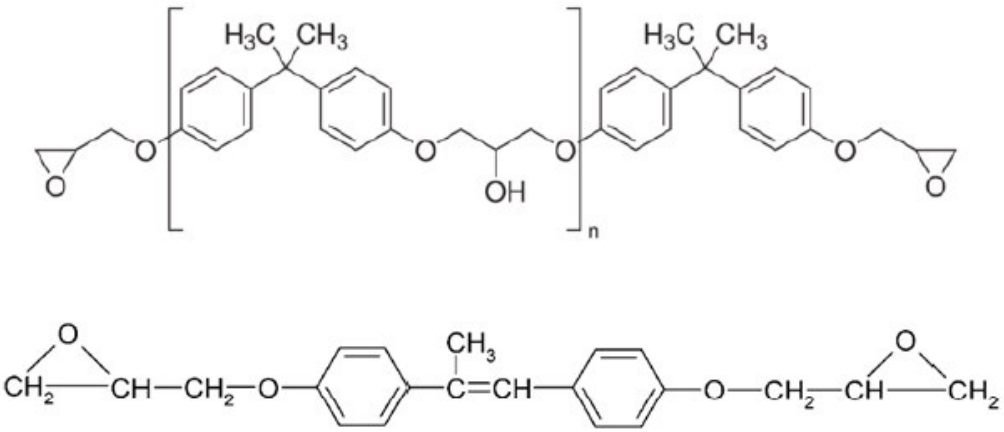

Figure 2.5 Structural formulas of EPON (top) and DOMS (bottom).

Dioxane, tricaprylylmethylammonium chloride (TCAC), chloroform, purity >99.5%, were obtained from Sigma-Aldrich and used as received.

The selected epoxy monomers (EPON and DOMS), MWCNT-COOH (1.5 wt%) and the catalyst (TCAC, 2 mol% with respect to the epoxy content) were sonicated with pulses of 5 seconds of sonication and 55 seconds of pause for 2 hours, at 150 °C, with an amplitude of 50%. The obtained products were then dispersed in a solvent (acetone for the mixture containing EPON and dioxane for that containing DOMS), heated at reflux for 20 min under stirring, cooled at room temperature and centrifuged at 10000 rpm for 12 minutes. Successively, the solutions containing the excess of epoxy monomer were removed. The solid precipitates were recovered and washed again with their own solvent, under stirring

at reflux for 20 min. According to the above described procedure, 5 washing and centrifugation cycles were carried out for each sample. Finally, the epoxy functionalized MWCNT adducts were dried under vacuum at 80 °C overnight.

These adducts were coded as MWCNT-EPON and MWCNT-DOMS, respectively.

2.2.2. Techniques

In order to confirm the formation of the epoxy-grafted MWCNT adducts hypothesized in Figure 2.6, and to characterize them, the adducts obtained from EPON and DOMS were purified by means of repeated washing and centrifugation cycles using suitable solvents (acetone for EPON and dioxane for DOMS).

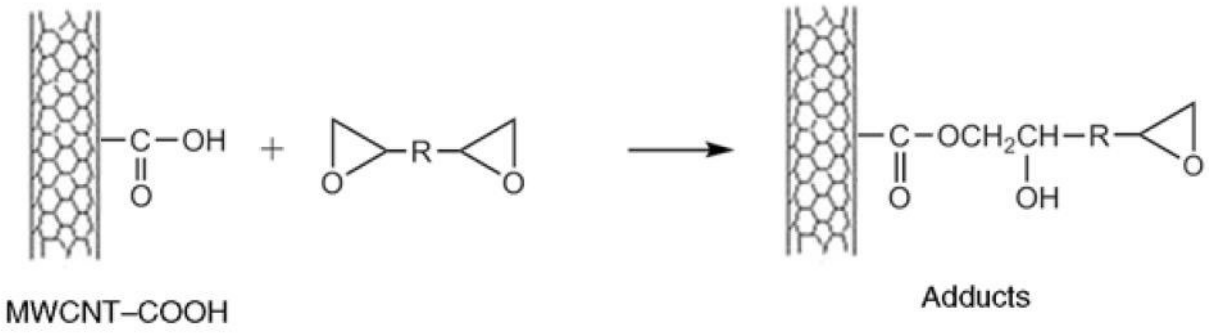

Figure 2.6 Reaction scheme between epoxy groups and carboxyl groups of MWCNT-COOH

The purified adducts were subjected to the following analytical procedures.

Dispersion Experiment

Dispersion experiments were performed on pure MWCNT-COOH, MWCNT-EPON as well as MWCNT-DOMS adducts. 5 mg of each sample were ultrasonicated in 30 mL of chloroform using a Sonics Vibracell (500 W, 20 kHz) ultrasonic processor (Sonics & Materials, Newtown, CT, USA). Ultrasonication was performed for 15 min alternating

ON/OFF cycles lasting 30 and 59 seconds, respectively. Amplitude was set at 25%. For the three experiments chloroform was used.

Fourier transform infrared (FTIR) spectroscopy

FTIR analysis was performed on the epoxy functionalized adducts MWCNT-EPON and MWCNT-DOMS. This technique was used to further confirm the occurred grafting of EPON and DOMS on the CNT surface and to get insight on the occurring reaction mechanism.

Transmission Electron Microscopy (TEM)

TEM analysis was performed by means of a FEI TECNAI G12 Spirit-Twin (120 kV, LaB6) microscope, equipped with a FEI Eagle 4K CCD camera (Eindhoven, The Netherlands). For the analysis, a small amount of modified MWCNTs were placed onto 400 mesh TEM copper grids and observed in bright field mode, with an acceleration voltage of 120 kV.

Thermogravimetric analysis (TGA)

TGA was carried out using a PerkinElmer Pyris Diamond thermogravimetric analyser (Wellesley,MA, USA). Unmodified MWCNT-COOH and their adducts grafted with EPON and DOMS (MWCNT-EPON and MWCNT-DOMS) were analyzed in air flux (50 mL min^{-1}) at a 10 °C min^{-1} heating rate using about 3 mg of material for each sample.

2.3. Results

As can be observed in Figure 2.7 from dispersion experiments, MWCNT-COOH started to settle after 2 hours from the sonication. On the contrary, both MWCNT-EPON and MWCNT-DOMS remained stably dispersed in chloroform for more than 24 hours after the

sonication. Nevertheless, it is to be remarked that the dispersion containing MWCNT-EPON showed a lower stability with respect to the one containing MWCNT-DOMS. In fact, after 36 hours after the sonication a partial settling of MWCNT-EPON was observed, thus suggesting a different grafting efficiency of the two monomers on the nanotube surface.

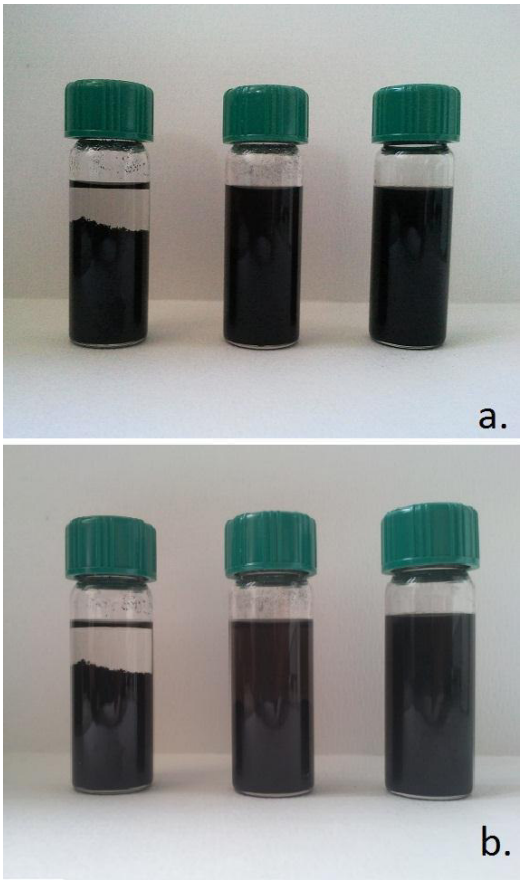

Figure 2.7 Dispersion stability in chloroform of MWCNT-COOH (left), MWCNT-EPON (middle) and MWCNT-DOMS (right) after: a) 2 hours and b) 36 hours after sonication

FTIR spectra of MWCNT-EPON and MWCNT-DOMS are reported in Figure 2.8 For comparison, spectra of EPON and DOMS are also reported in the same figure.

Consistently with previously reported data [23],[24], no detectable transmission bands were observed for the pristine MWCNT as well as for MWCNT-COOH. The most significant result obtained by FTIR analysis of the adducts was that either MWCNT-EPON and MWCNT-DOMS

present absorption bands centered at about 1730 cm-1, characteristics of the ester bond formed between the epoxy groups of EPON and DOMS and the carboxyl groups of MWCNT-COOH. Moreover, the adducts show the presence of absorption bands attributable to the stretching of aromatic C=C (1600-1610 cm-1) and C-C (1500-1510 cm-1), and of absorption bands characteristic of the stretching of C-O and C-O-C oxirane groups (800-930 cm-1) [25].

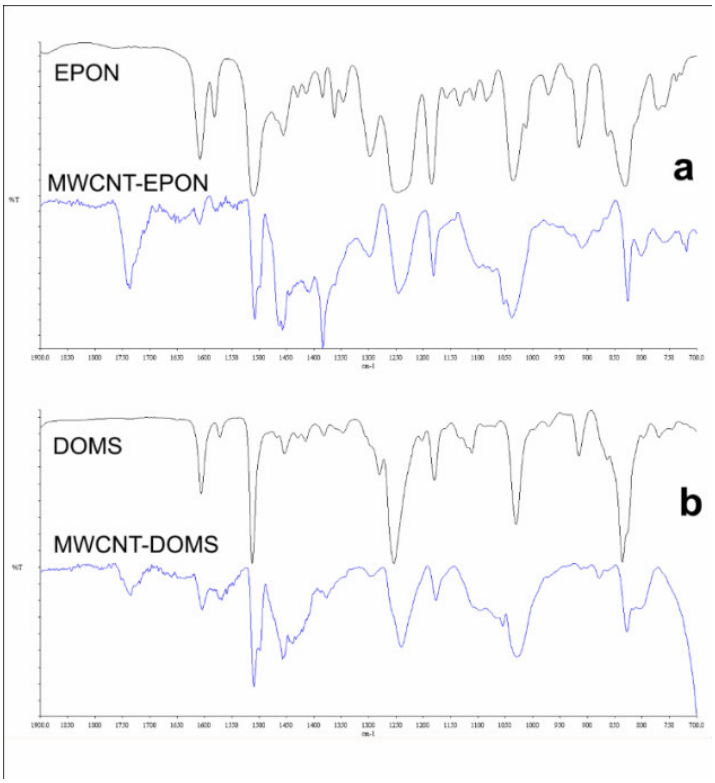

Figure 2.8 FTIR spectra in the range 1900-690 cm^{-1} of: a) EPON and MWCNT-EPON and b) DOMS and MWCNT-DOMS.

These result confirmed the occurred grafting of EPON and DOMS on the surface of MWCNT-COOH.

TEM analysis of DOMS-grafted nanotubes (Figure 2.9) after purification evidenced the presence of a uniform 5 nm thick layer covering the surface of the nanotubes.

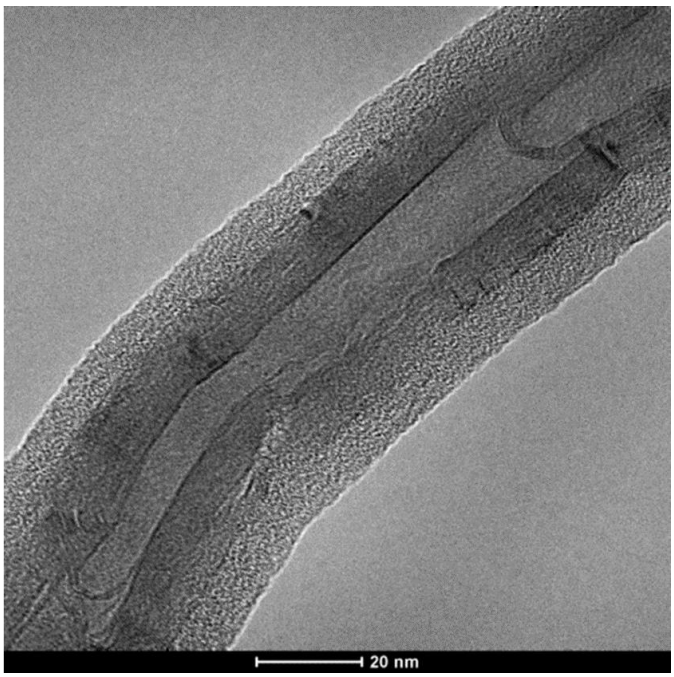

Figure 2.9 Bright field TEM image of the MWCNT-DOMS adduct.

From geometrical considerations, this value corresponds to a DOMS content of about 16 wt %, which is in good agreement with the amount obtained from thermogravimetric analysis.

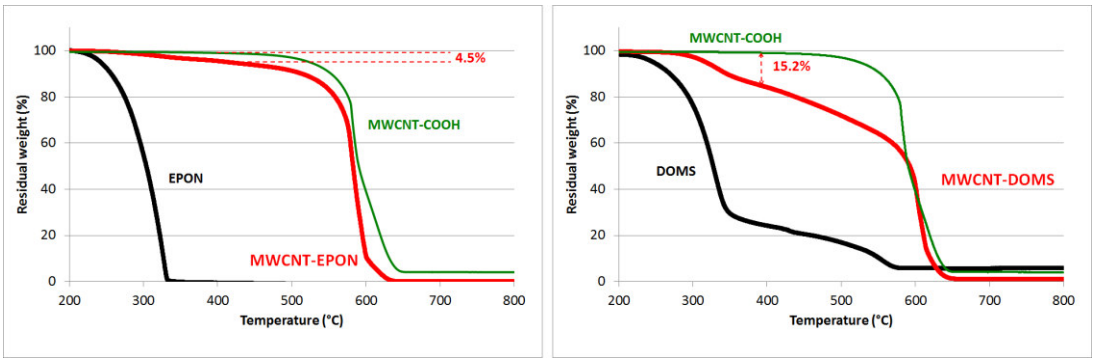

Figure 2.10 TGA traces in air flow of MWCNT-COOH, EPON, MWCNT-EPON, DOMS, and MWCNT-DOMS.

Indeed, the quantitative evaluation of the amount of EPON and DOMS grafted onto the MWCNT was obtained by TGA analysis performed in air flow. Figure 2.10 shows TGA traces of MWCNT-COOH, EPON and MWCNT-EPON, DOMS and MWCNT-DOMS. For temperatures

lower than 200 °C, the samples did not exhibit any significant degradation phenomena. At higher temperatures, they showed different thermo-oxidative behaviour.

In particular, EPON showed a degradation process occurring in one step in the range 200-370 °C. DOMS underwent thermooxidative degradation through a 2-step mechanism, the first step occurring in the range 200-400 °C, and the second one in the range 400-600 °C.

On the other hand, the TGA trace of MWCNT-COOH did not show any appreciable weight loss before 400 °C. The onset of the degradation process, evaluated as 2 wt% of weight loss, is at about 470 °C.

As concerning MWCNT-EPON and MWCNT-DOMS, both exhibited a weight loss step in the range between 250 and 400 °C. This phenomenon is related to the degradation of the EPON and DOMS fractions that were not removed after purification, thus supporting the occurrence of grafting between the epoxy monomers and the nanotubes, and allowing to determine the amount of grafted species on the CNT.

In particular, as indicated in Figure 2.10, MWCNT-EPON showed about 4.5 wt% of epoxy monomer grafted, whereas MWCNT-DOMS showed about 15 wt% of DOMS covalently bonded to the nanotube surface.

Taking into consideration that the theoretical amount of epoxy monomer that can be grafted to the COOH groups on the MWCNT-COOH is about 5 wt% both for EPON and for DOMS, it can be observed that in the case of MWCNT-EPON, the grafting efficiency is very close to the theoretical value. On the contrary, for MWCNT-DOMS the amount of reacted epoxy monomer exceeds the nominal value. This phenomenon may be attributed to the homopolymerization of DOMS monomers, which is a possible competitive reaction since at high temperatures epoxies are reactive towards self-polymerization to polyethers [26],[27],

especially in presence of proton donors present in the reacting mixtures, such as carboxylic acids or impurities formed during the synthesis.

2.4. Conclusions

This chapter dealt with the functionalization of MWCNT with two diepoxy monomers, namely EPON and DOMS.

EPON was a commercial product, whereas DOMS was obtained by a synthetic protocol previously set up in the research group in which this thesis work has been carried out.

The effective compatibilization strategy aimed to the improvement of the interfacial adhesion between epoxy resins and CNT and to promote a homogeneous dispersion of the nanotubes within both the matrices, has been set up. The first step of this strategy was studied in this chapter. It has been based on the covalent functionalization of the MWCNT-COOH, obtained by grafting the epoxy monomers on their surface. In this way, epoxy functionalized CNT adducts have been realized, able to further react during the curing process.

The functionalized MWCNT adducts have been isolated and characterized by means of solvent dispersion experiment, FTIR analysis, TEM analysis and TGA analysis, showing that appreciable amounts of diepoxy monomers have been grafted on the nanotube surface.

In the case of DOMS, this amount exceeded the theoretical value calculated on the basis of the COOH content of the as received nanotubes. This phenomenon has been attributed to the homopolymerization of DOMS monomers, since at high temperatures epoxies are reactive towards self-polymerization.

2.5. References

1 A. Merkoçi, M. Pumera, X. Llopis, B. Pérez, M. del Valle, S. Alegret (2005): New materials for electrochemical sensing VI: Carbon nanotubes. Trends in Analytical Chemistry, Vol. 24, No. 9

2 A. Jorio, A.G. Souza Filho, G. Dresselhaus, M.S. Dresselhaus, A. Righi, F.M. Matinaga, M.S.S. Dantas, M.A. Pimenta, J. Mendes Filho, Z.M. Li, Z.K. Tang, R. Saito (2002): Raman studies on 0.4 nm diameter single wall carbon nanotubes. Chemical Physics Letters, 351(1-2), 27–34

3 M. Moniruzzaman and K. I. Winey (2006): Review: Polymer Nanocomposites Containing Carbon Nanotubes. Macromolecules**,** *39,* 5194-5205

4 F. Hussain, M. Hojjati, M. Okamoto, R.ER. Gorga (2006): Review article: Polymer-matrix Nanocomposites, Processing,Manufacturing, and Application: An Overview. Journal of Composite materials, 40(17), 1511-1575

5 P.M. Ajayan, O.Z. Zhou. Application of Carbon nanotubes, in M.S. Dresselhaus, G. Dresselhaus, P. Avouris, Eds, Carbon Nanotubes - Synthesis, Structure, properties and Applications, Springer, Berlin, 2001, 391-425

6 K.A. Wepasnick, B.A. Smit, J. Bitter, D.H. Fairbrother (2010): Chemical and structural characterization of carbon nanotube surfaces. AnalBioanalChem, 396(3):1003-1014

7 O. Matarredona, H. Rhoads, Z. Li, J. Harwell, L. Balzano, D. Resasco (2003): Dispersion of single-walled carbon nanotubes in aqueous solutions of the anionic surfactant NaDDBS. J PhysChem B, 107, 13357-13367

8 J. Cheng, K.A.S. Fernando, L.M. Veca, Y-P. Sun, A. Lamond, et al. (2008): Reversible accumulation of PEGylatedsinglewalled carbon nanotubes in the mammalian nucleus. ACS Nano, 2(10), 2085-2094

9 T.E. Chang, L.R. Jensen, A. Kisliuk, R.B. Pipes, R. Pyrz, A.P. Sokolov (2005): Microscopic mechanism of reinforcement in single-wall carbon nanotube/polypropylene nanocomposite. Polymer 46(2), 439-444

10 B. Chandra, J.Bhattacharjee, M.Purewal, Y.-W. Son,Y. Wu, M. Huang, et al. (2009): Molecular-scale quantum dots from carbon nanotube heterojunctions. NanoLett; 9(4):1544-8

11 L. Vaisman, G.Marom, H.D. Wagner (2006): Dispersions of surface-modified carbonnanotubes in water-soluble and water-insoluble polymers. AdvFunct Mater;16(3):357-63

12 A. Satake, Y.Miyajima, Y.Kobuke (2005): Porphyrin-carbon nanotube compositesformed by noncovalent polymer wrapping. Chem Mater;17(4):716-24

13 X. Xin, G. Xu, T. Zhao, Y. Zhu, X. Shi, H. Gong, et al. (2008): Dispersing carbon nanotubesin aqueous solutions by a starlike block copolymer. J PhysChem C;112(42):16377-16384

14 J. Deng, J. Cao, T. Li, H. Tan, Q. Zhang, Q. Fu (2008): Mechanical and surface properties ofpolyurethane/fluorinated multi-walled carbon nanotubes composites. J ApplPolym Sci;108(3):2023-8

15 X.H. Men, Z.Z. Zhang, H.J. Song, K. Wang, W. Jiang (2008): Functionalization of carbonnanotubes to improve the tribological properties of poly(furfuryl alcohol)composite coatings. Compos SciTechnol; 68(3-4):1042-9

16 B.-X. Yang, J.-H. Shi, K.P.Pramoda, S.H.Goh (2007): Enhancement of stiffness,strength, ductility and toughness of poly(ethylene oxide) using phenoxygraftedmultiwalled carbon nanotubes. Nanotechnology;18(12):125606

17 I.D. Rosca, F.Watari, M.Uo, T.Akasaka (2005): Oxidation of multiwalled carbon nanotubes by nitric acid. Carbon;43(15):3124-31

18 V. Datsyuk, M.Kalyva, K.Papagelis, J.Parthenios, D.Tasis, A. Siokou, et al. (2008):Chemical oxidation of multiwalled carbon nanotubes. Carbon;46(6): 833-40

19 M. Li, M. Boggs, T.P. Beebe, C.P. Huang. (2008): Oxidation of single-walled carbonnanotubes in dilute aqueous solutions by ozone as affected by ultrasound. Carbon;46(3): 466-75

20 S. Osswald, M. Havel, Y.Gogotsi (2007): Monitoring oxidation of multiwalledcarbon nanotubes by Raman spectroscopy. J Raman Spectrosc;38(6):728-36

21 N.P. Zschoerper, V.Katzenmaier, U.Vohrer, M.Haupt, C.Oehr, T.Hirth (2009): Analyticalinvestigation of the composition of plasma-induced functional groups oncarbon nanotube sheets. Carbon; 47(9):2174-85

[22] Giamberini M, Amendola E, Carfagna C. Mol Cryst Liq Cryst 1995; 266:9–22

[23] V.Ambrogi, G. Gentile, C. Ducati, M.C. Oliva, C. Carfagna(2012): Multiwalled carbon nanotubes functionalized with maleated poly(propylene)by a dry mechano-chemical process. Polymer 53, 291-299

[24] A. Koshio, M. Yudasaka, M. Zhang, S. Iijima (2001): A simple way to chemicallyreactsingle-wall carbon nanotubes with organic materials using ultrasonication. Nano Lett1(7), 361-363.

[25] M. Gonzales, J.C. Cabalenas, J. Baselga: Application of FTIR on Epoxy resins – Identification, Monitoring the Curing Process, phase Separation and Water Uptake. In T. Thephile Ed., Infrared Spectroscopy – Materials Science, Engineering and Technology, InTech Europe, Rijeka, Croatia, 2012.

[26] M. Galià, A. Mantecon,V. Càdiz, A. Serra (1990). MakromolChem; 191:1111–8.

[27] M.S. Wang,T.J.Pinnavaia (1994). Chem Mater;6:468–74

CHAPTER 3

Shape Memory Elastomers filled with MWCNT

3.1. Introduction

As reported previously, in order to get an homogeneous dispersion within a polymer matrix, a nanofiller should be first surface-modified and compatibilized. In section 2.2.1, this first step has been accomplished, through the surface modification of MWCNT, aimed to obtain SMPNC based on a LCE epoxy-based matrix, and MWCNT as filler. Incorporation of these carbonaceous nanoparticles is expected to enable tailoring of the SME of the polymer matrix, giving rise to stimuli-responsive systems potentially interesting for a variety of applications, such as electronics, [1] biomaterials, [2] aerospace, [3] sensing and actuation, [4] and artificial muscles. [5]

In this view, many liquid crystalline elastomers (LCE) have been explored as stimuli responsive actuators, thanks to their exceptional thermomechanical behavior. [6,7,8,9] In fact, LCE show a spontaneous shape modification at phase transition, which results in a temperature-triggered strain recovery after the application of a tensile stress. These properties come about thanks to the combination of the orientational order, characteristic of the liquid crystalline chains, with the entropic elasticity of the polymer network. [10] LCE's thermomechanical properties are strictly related to the ability of the material to experience a reversible transition of the LC phase, from polydomain to monodomain, under stress. This transition is due to the parallel alignment of the mesogens with the stress axis. [11]

Such property is characteristic of both main-chain and side-chain LCE: Under tensile stress, the liquid crystalline domains tend to cooperatively align to the stress direction generating an elastomer with a monodomain structure, making them appealing as shape-memory systems. [12] Currently, two different classes of SMP are the subject of relevant studies, the so-called "one way" (1W) and "two way" (2W) shape-memory materials. In

particular, 1W SMP can be programmed in a temporary shape and are able to recover the equilibrium shape when heated above a threshold temperature (usually a first- or second-order phase transition temperature). However, 2W SMP feature musclelike contraction on heating and extension on cooling under tensile load, due to a reversible isotropic-to anisotropic transition. [13,14]

A potential strategy to tailor responsiveness of LCEs is represented by the incorporation of functional conjugated compounds [15] or thermal conductive fillers, such as gold nanoparticles [16,17] or carbon nanotubes (CNT). [18] The incorporation of CNT into LCE can promote a faster and more efficient response over the thermal actuation, improving thermal conductivity of polymeric LCE and thus inducing a quick delivery of heat to all mesogens. [18] Furthermore, CNT can also allow the actuation through other stimuli (e.g., electric and magnetic fields). [19] Moreover, coupling of aligned mesogens and high aspect ratio CNT, under uniaxial tensile force, may contribute to the soft elasticity and enhance the thermomechanical response. In literature, the mutual alignment between either low-molecular-weight or polymer liquid crystals and CNT has been proven. [20] In addition, it is reported that in some circumstances the presence of carbon nanoparticles partially destabilizes the liquid crystalline phase of the elastomeric network. [21] Recently, it has been demonstrated that by changing the extent of liquid crystallinity and the crosslinking density it is possible to tailor the LC transition and the thermomechanical properties of epoxy elastomers. [22] Therefore, addition of CNT to LCE is an appealing strategy to modulate the stability and the extent of the mesophase, thereby providing another way to tune the shape-memory properties of this class of materials. [3] In the present work, we demonstrate the feasibility of this approach. To this aim, smectic main chain liquid crystalline elastomer composites were prepared by adding multiwalled carbon nanotubes (MWCNT) to a diepoxy

monomer cured with an aliphatic dicarboxylic acid. In particular, (DOMS) was used as a mesogenic epoxy monomer and sebacic acid (SA) was used as curing agent.

A suitable surface modification strategy of the nanotubes was set up to promote the formation of homogeneous composite systems, thereby avoiding MWCNT segregation and maximizing their effects on the LCE phase behavior. [23,24,25] EPON was used as a reference point to prepare neat samples and to optimize the compatibilization strategy between epoxy monomers and nanofillers.

LC elastomeric nanocomposites were prepared with different amounts of MWCNT and characterized in their physicomechanical properties. Relationships between microstructure and thermomechanical properties of the materials were elucidated by calorimetry, mechanical and dynamic-mechanical analyses, variable-temperature X-ray diffraction, and morphological analysis, revealing that carbon nanotubes enhance actuation in shape-memory liquid crystalline elastomers.

3.2. Experimental

3.2.1. Materials

Same materials used in Chapter 2 were used in this section. In addition, sebacic acid (SA, melting point 133−137 °C), purity >99%, obtained from Sigma-Aldrich, was used as received. In figure 3.1, the structure of sebacic acid is represented.

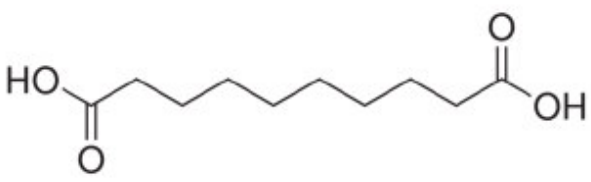

Figure 3.1 Structural formula of sebacic acid

Neat epoxy elastomer was obtained by adding to 3 g of epoxy monomer the stoichiometric amount of SA (molar ratio 1:1). Once SA melted, the catalyst (TCAC, 2 mol % with respect to the amount of epoxy groups) was added, and the mixture was kept under magnetic stirring for 5 min at 160 °C. The viscous mixture was then poured between two previously heated Teflon-coated glass slides sealed with a silicone gasket and secured with steel clamps and cured in oven at 185 °C for 2 h. The obtained film sample (about 100 mm long, 100 mm wide, 0.25 mm thick), depending on the epoxy monomer used, was coded as DOMS_SA or EPON_SA.

The cross-linking reaction of epoxy monomers with dicarboxylic acids is characterized by a very complex mechanism, involving several competitive reactions, which are responsible for the dissimilar growth of the forming networks. Depending on the experimental conditions employed in the synthesis of the epoxy based elastomers, such as nature of epoxy monomer, length of flexible spacer, curing time and temperatures, molar ratio of reactants, different physical and mechanical properties are displayed. The reaction scheme between epoxy monomer and carboxylic acids is reported in figure 3.2.

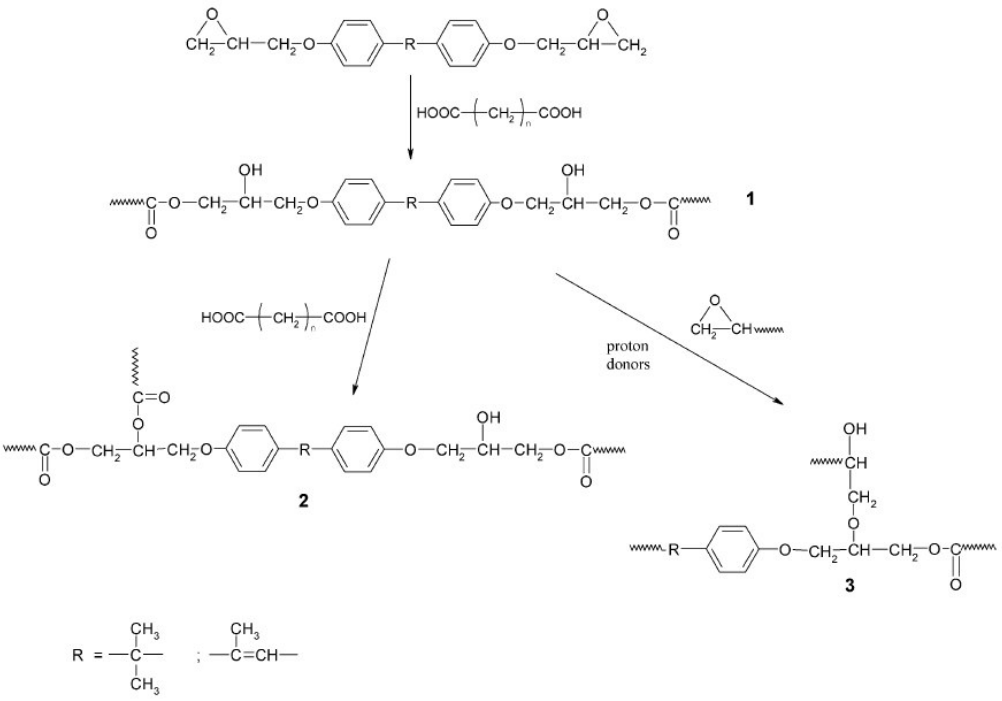

Figure 3.2 Reaction scheme between epoxy monomers and carboxylic acids

It proceeds via opening of the epoxy ring by the carboxyl group [26,27] (1). The hydroxyl groups produced are subsequently involved in the reaction with carboxylic acid, resulting in the formation of ester linkages by condensation (2), or in the etherification through the reaction with the epoxy molecules not reacted yet (3). On the other hand, at high temperatures homopolymerization of the diglycidyl derivative is also a possible competitive reaction (see Figure 3.3).

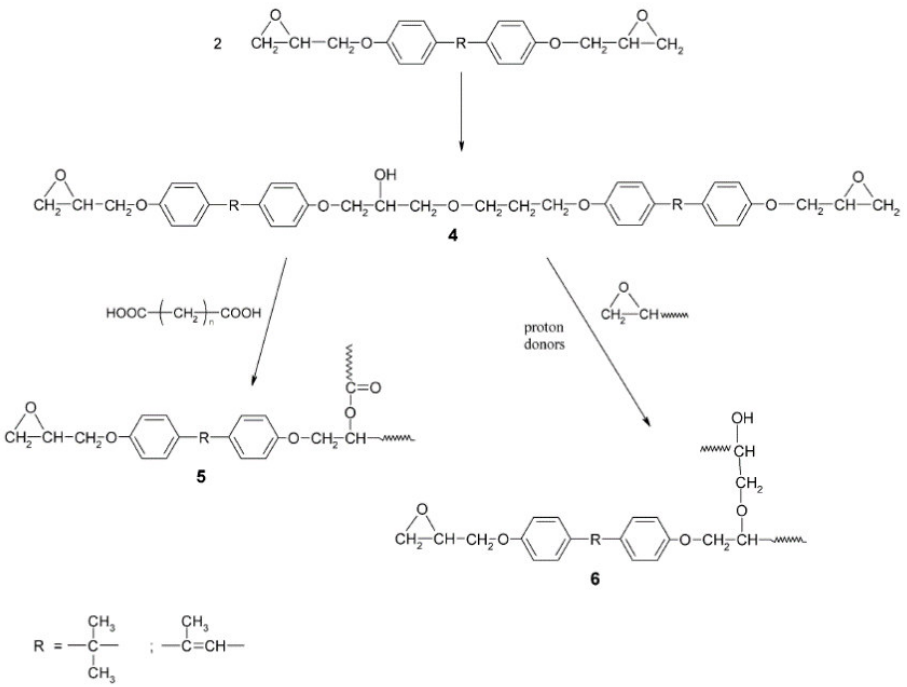

Figure 3.3 Homopolymerization reaction in the epoxy/acid mixture

The hydroxyl group in the ether dimer (4), can undergo both esterification with acid (5), or further etherification with an epoxy (6). Hydroxyl groups are, therefore, responsible for the formation of a lightly crosslinked network. The prevailing reaction path depends on the experimental conditions (reaction temperature, epoxy/acid molar ratio, nature of monomers and acids selected) and has not been clearly established [28] . In any case, independently of the monomer used, an elastomeric network is obtained. When mesogenic monomers, such as DOMS, are used, during the curing reaction with a curing agent, such as sebacic acid, a liquid crystalline phase is formed, embedded within the final network.

In the particular case of DOMS-SA a smectic elastomer was obtained, as inferred from already reported data [29] and further studied in this work.

For the epoxy-based nanocomposites, a study on the procedure protocol was required.

As further detailed, epoxy-based nanocomposites were obtained by a two-step procedure. First, nanotubes were dispersed in the molten monomers and then the obtained mixtures were poured in Teflon-coated glass molds and cured in oven at 185 °C.

The main problem faced during the preparation of the nanocomposites was the obtainment of macroscopically homogeneous samples.

In the first trial (procedure A), unmodified MWCNT were dispersed at 1.5 wt% load into the EPON/SA mixture under magnetic stirring. Therefore, the mixture was poured into the mold and polymerized at 185 °C for 18 hours without the use of a catalyst. As soon as transferred to the mold, the molten mixture containing the nanotubes appeared macroscopically homogeneous. Nevertheless, as it can be observed from the image of the cured sample (A_ES_1.5CNT) reported in Figure 3.4, the obtained material was highly inhomogeneous, with large areas in which nanotubes were wholly absent. This suggests that the segregation mainly occurred during the curing step between the molds.

Figure 3.4 Image of the sample A_ES_1.5CNT. Scale bar 0.5 cm

In order to reduce this effect, in the next trials the curing time was decreased, by the use of a suitable catalyst, TCAC.

Furthermore, to improve the distribution of the nanotubes within the epoxy matrix, commercial functionalized nanotubes, containing 0.7 wt% of COOH groups, were used in the next experiments.

Therefore, in procedure B, EPON and DOMS-based nanocomposites were realized by adding 0.75 wt% and 1.5 wt% of MWCNT-COOH. The nanotubes were dispersed in the mixture of monomers under magnetic stirring. The catalyst was added before transferring the mixture to the Teflon-coated glass molds and the cure was performed for 2 hours in oven at 185 °C. The picture of the obtained samples (EPON-based nanocomposites: B_ES_0.75fCNT and B_ES_1.5fCNT; DOMS-based nanocomposites: B_DS_0.75fCNT and B_DS_1.5fCNT) are reported in Figures 3.5 and 3.6, respectively. As shown, only for the sample B_ES_1.5fCNT an improved macroscopic homogeneity was achieved, but in most cases, and especially at the lowest CNT content, the nanotubes resulted highly agglomerated and large areas devoid of any nanotubes were evident.

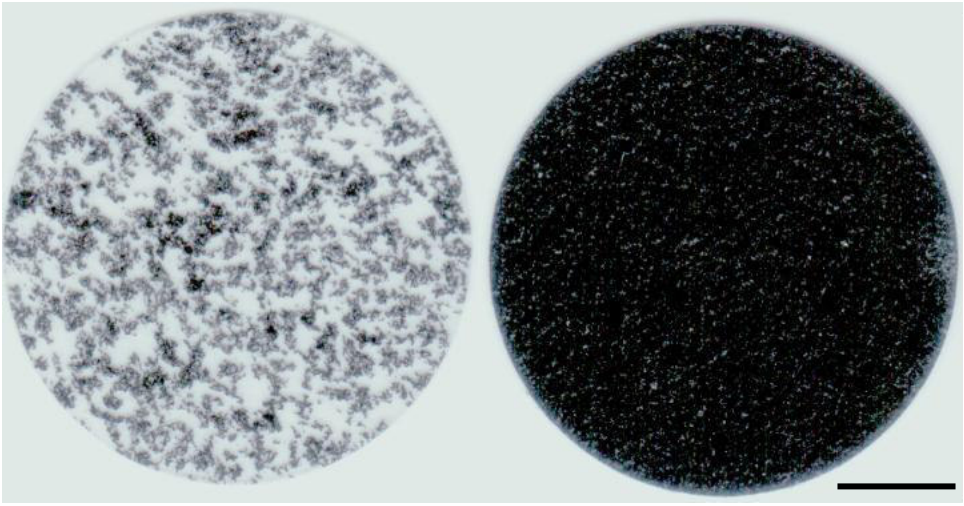

Figure 3.5 Images of the samples B_ES_0.75fCNT (left) and B_ES_1.5fCNT (right). Scale bar 0.5 cm

Figure 3.6 Images of the samples B_DS_0.75fCNT (left) and B_DS_1.5fCNT (right). Scale bar 0.5 cm

A further attempt to improve the CNT distribution into the epoxy matrices was performed by using a preliminary treatment of the MWCNT-COOH in a planetary ball milling in presence of EPON and SA (procedure C). After that, the obtained mixture was transferred to a beaker and the same 2-step curing process adopted in the procedure B was carried out. In this case, only the EPON based systems containing 0.75 wt% and 1.5 wt% of MWCNT-COOH were prepared. As a matter of fact, in the case of DOMS, the ball milling process was not able to promote a macroscopically homogeneous dispersion of the nanotubes within the mixture of monomers. This was due to the higher melting temperature of DOMS with respect to EPON. During ball milling DOMS was not melted and it was recovered at the end of the milling process completely separated from the rest of the mixture.

The images of the EPON based samples obtained with this procedure (C_ES_0.75fCNT and C_ES_1.5fCNT) are reported in Figure 3.7. As it can be observed, a significant improvement of their macroscopic homogeneity was achieved with this methodology only for the sample containing 1.5 wt% of MWCNT-COOH (C_ES_1.5fCNT).

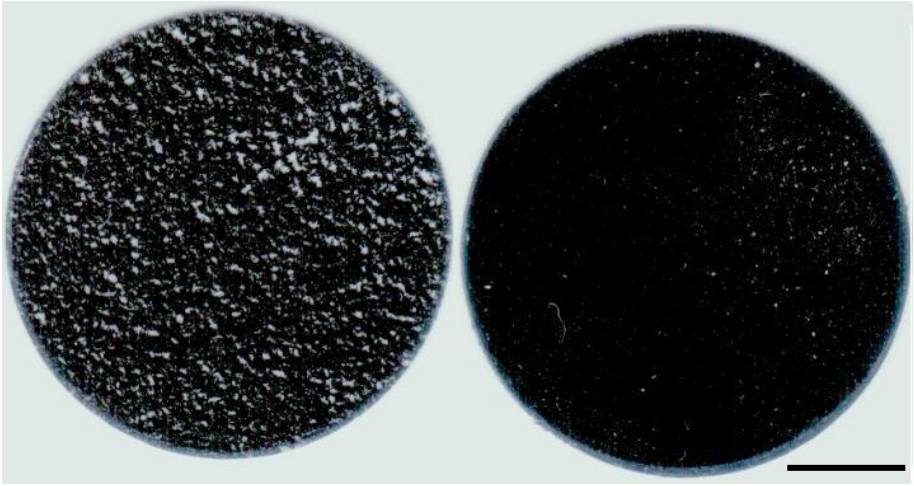

Figure 3.7 Images of the samples C_ES_0.75fCNT (left) and C_ES_1.5fCNT (right). Scale bar 0.5 cm

The next procedure used to avoid agglomeration phenomena and poor distribution of the nanotubes into the matrices was based on the preliminary sonication of MWCNT-COOH in an EPON solution in THF (procedure D). After sonication and solvent evaporation, the mixture was transferred in a beaker to carry out the same curing process described for the procedures B and C. With this procedure EPON based nanocomposites containing 0.75 wt% and 1.5 wt% of MWCNT-COOH were realized.

The pictures of the obtained samples (D_ES_0.75fCNT and D_ES_1.5fCNT) are reported in Figure 3.8. As it can be observed, the solvent-aided sonication procedure was not effective to obtain homogeneous materials.

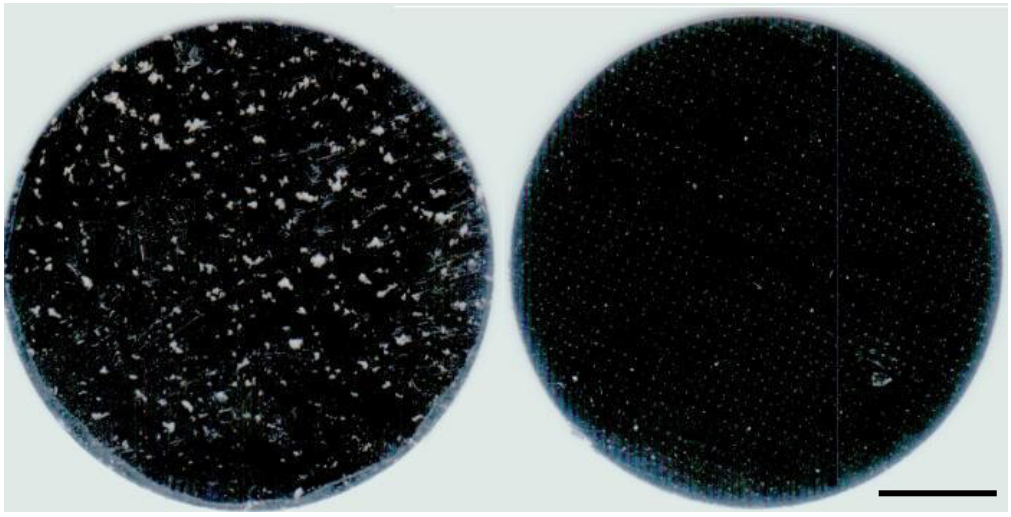

Figure 3.8 Images of the samples D_ES_0.75fCNT (left) and D_ES_1.5fCNT (right). Scale bar 0.5 cm

Based on the obtained results, a different approach was tested to improve the nanotube dispersion within the epoxy matrices. In procedure E, nanocomposites were obtained by a two-step procedure, the first involving the dispersion of nanotubes in the molten DOMS and the formation of an epoxy-functionalized MWCNT adduct. Subsequently, the curing reaction between epoxy monomer and SA was carried out in an oven. In particular, the first part of this procedure was performed following the same scheduling of chapter 2.

For each preparation, the content of MWCNT-COOH was calculated taking into account the desired final content of nanofiller in the nanocomposites after the addition of SA. After the first step, SA (1:1 molar ratio with respect to the initial DOMS) was added to the reaction mixture containing the MWCNT-DOMS. As soon as the cross-linking agent melted, additional catalyst (TCAC, 2 mol %) was introduced. The obtained mixture was sonicated for further 120 s using the same experimental conditions. The resulting material was poured in the previously described glass mold and cured in an oven at 185 °C for 2 h.

The obtained samples (about 100 mm long, 100 mm wide, 0.25 mm thick) were coded as DS_xCNT, where x is the final content of nanotubes in the nanocomposites (x = 0.75, 1.5,

and 3.0 wt %). In Figure 3.9 and 3.10 are shown the specimens resulting from Procedure E, labeled E_ES_0.75fCNT, E_ES_1.5fCNT, DS_0.75CNT and DS_1.5CNT.

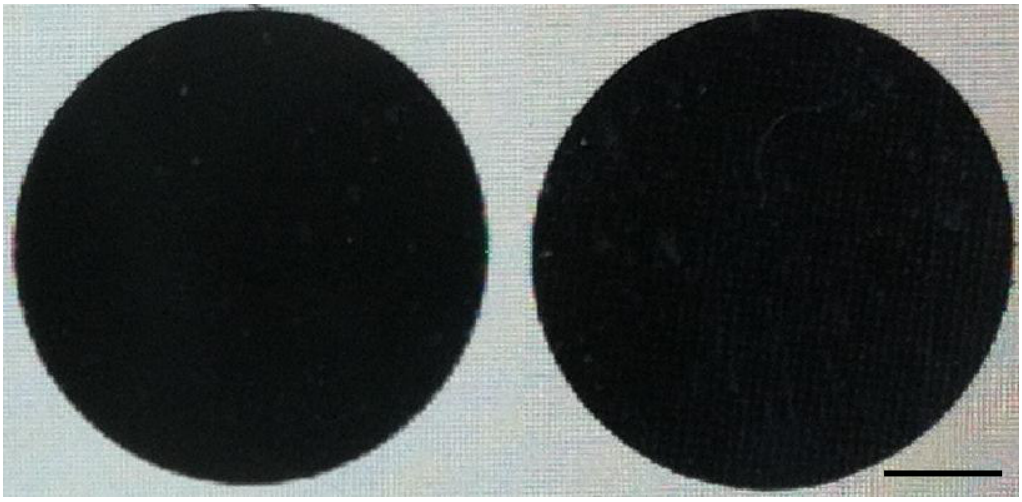

Figure 3.9 Images of the samples E_ES_0.75fCNT (left) and E_ES_1.5fCNT (right). Scale bar 0.5 cm

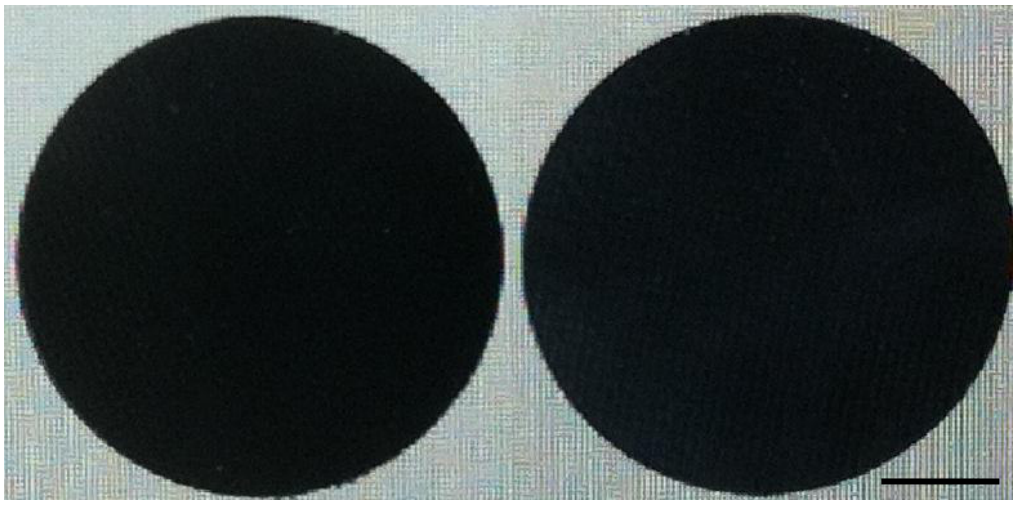

Figure 3.10 Images of the samples DS_0.75CNT (left) and DS_1.5CNT (right). Scale bar 0.5 cm

3.2.2. Techniques

Scanning Electron Microscopy (SEM)

SEM analysis was performed using a FEI Quanta 200 FEG (Eindhoven, The Netherlands) in high vacuum mode, using a secondary electron detector and an accelerating voltage

ranging between 15 and 20 kV. For the analysis, pieces were obtained from the samples coded DS_xCNT. They were cooled down with liquid nitrogen, and a brittle fracture was obtained. Before the analysis samples were coated with a gold-palladium layer (about 15 nm thick) by means of a sputter coater Emitech K575X.

Transmission Electron Microscopy (TEM)

TEM analysis was performed on a FEI TECNAI G12 Spirit-Twin (120 kV, LaB6) microscope equipped with a FEI Eagle 4K CCD camera (Eindhoven, The Netherlands).

For the analysis, pieces removed from the samples coded C_ES_1.5fCNT, and DS_1.5CNT were used. Small strips (about 3 mm x 10 mm) were cut from the specimens and embedded in an Epoxy embedding medium by the procedure reported below.

The Epoxy embedding medium (45359, Sigma-Aldrich) was constituted by the following components:

- Epoxy embedding medium (EEM)
- 2-Dodecenylsuccinic anhydride (DDSA)
- Methylnadic anhydride (NMA)
- 2,4,6-tris(dimethylaminomethyl)phenol (DPM-30)

A solution containing the EEM (5 mL) and DDSA (8 mL) was prepared at room temperature under vigorous stirring for 30 min (mixture A). Another solution containing the EEM (8 mL) and NMA (7 mL) was prepared at room temperature under vigorous stirring for 30 min(mixture B). The two mixtures were blended in a ratio 1:1 by volume under vigorous stirring for further 30 min and the accelerator DPM-30 was added (16 drops, > 2.0 wt%).

The resin was poured in the cavities of a multi-specimen rubber silicon mold, and in each cavity the small strips obtained from the samples were placed. Finally, the resin was polymerized at 45°C for 12 h followed by 48 h at 60°C.

The obtained embedded specimens were sectioned with a diamond knife at room temperature using a Leica UC7 ultramicrotome (nominal thickness 160 nm). The sections were finally placed onto 400 mesh TEM copper grids and observed in bright field mode with an acceleration voltage of 120 kV.

Differential Scanning Calorimeter (DSC)

Phase and glass transition temperatures of prepared elastomers were determined using a TA Instruments DSC Q2000 Differential Scanning Calorimeter (DSC). The analyses were performed in dynamic mode at a 10 °C min^{-1} heating rate from −20 to 150 °C.

Dynamic mechanical analysis (TMA)

Dynamic mechanical analysis was performed on polydomain samples by means of a PerkinElmer Pyris Diamond DMA dynamic mechanical analyzer in the film tensile configuration at a frequency of 1 Hz and a strain amplitude of 5 µm. Samples (length 10 mm, width 9 mm, average thickness 0.25 mm) were heated from 25 to 120 °C at 3 °C min^{-1}.

Tensile tests

Mechanical tensile tests were performed on dumbbell-shaped specimens die-cut from the films (0.25 mm thickness, 25 mm gauge length, 4 mm gauge width). An Instron 5564 mechanical testing machine was employed, equipped with a 1 kN load cell and a forced air oven, at a temperature of 40 °C, which was above the glass transition temperature of the

samples. Stress−strain tests were performed at a crosshead displacement rate of 50 mm min−1, according to ASTM D412-2006 standard test method.

Thermomechanical analysis (TMA)

Thermomechanical analysis was performed on a PerkinElmer Pyris Diamond DMA apparatus operated in controlled force mode. Prior to start, samples (gauge length 5 mm, width 9 mm, average thickness 0.25 mm) were thermally equilibrated at 100 °C for 10 min. To characterize the two-way shape-memory effect, the following four-step experiment was carried out: (1) stretching the sample at T = 100 °C by ramping force from a prestress of 4.5 kPa to a final stress value of 45 kPa (180 kPa for experiments with stepwise decreasing stress, as in Figure 3.13e), during 10 min (deformation), (2) cooling the sample at the rate of 2 °C min−1 to 10 °C under constant force and keeping the sample at this temperature for 10 min (cooling), (3) unloading the force to prestress value (to half of the value, for experiments with stepwise decreasing stress), during 10 min (unloading and shape fixing), and (4) reheating the sample to 120 °C and annealing for 10 min (recovery). Characterization of the triple-shape-memory effect only differed in that during the last step the sample was reheated up to an intermediate temperature of 60 °C, kept in isothermal conditions for 30 min, and finally heated to 120 °C.

Wide angle X-ray diffraction (WAXD)

Wide-angle X-ray scattering analysis (WAXS) was carried out using a Rigaku model III/D max generator equipped with a 2D imaging plate detector, using a Ni-filtered Cu Kα radiation (wavelength 1.5418 Å) at room temperature on unstretched DOMS_SA and DS_0.75CNT, as well as on the same samples in the maximum elongation state reached

during thermomechanical tests (after step 3). The order parameter S was calculated on the unstretched and stretched DOMS_SA and DS_0.75CNT by applying the following equations:

$$S = \frac{1}{2}(3[\cos^2\theta] - 1) \quad (1)$$

$$[\cos^2\theta] = 1 - 2[\cos^2 x] \quad (2)$$

$$[\cos^2 x] = \frac{\int_0^{\pi/2} I(\cos^2 x)(\sin x)dx}{I(\sin x)dx} \quad (3)$$

where x is the coordinate of azimuthal scans performed on the diffraction patterns. Variable-temperature WAXS analysis was carried out using an Anton Paar SAXSess camera equipped with a 2D imaging plate detector. Cu Kα X-rays were generated by a Philips PW3830 sealed tube source and slit collimated. Variable temperature diffractograms were collected at different temperatures during cooling. For each step, the temperature was held for 10 min before starting the measurement. All scattering data were corrected for background and normalized for the primary beam intensity. In order to remove the inelastic scattering from the data, WAXS profiles were additionally corrected for the smearing effect. Collected data were normalized with respect to the sample thickness.

Electrical resistivity

Electrical volume resistivity of the obtained samples DOMS-SA, DS_0.75CNT, DS_1.5CNT and DS_3.0CNT and was evaluated according to ASTM D257 with a Keithley 8009 Resistivity Test Fixture and a Keithley 6517 Electrometer. The analysis were carried out with the following conditions: 80 seconds measure time, offset voltage 0V, alternate voltage 200V and 8 collected points per sample. For the evaluation of SME due to resistive heating, analysis with a FLIR ThermoVision A40 infrared camera was carried out.

3.3. Results

The first aim related to the realization of the nanocomposites was the achievement of homogeneous samples. In fact, all samples prepared using unmodified MWCNT or MWCNT-COOH were macroscopically inhomogeneous, with the presence of large agglomerates of nanotubes evidenced by SEM and TEM (Figure 3.11). Therefore, a new approach undertaken to improve nanotube dispersion consisted in a prolonged sonication of MWCNT-COOH in molten DOMS in the presence of TCAC as catalyst. This step promoted grafting of DOMS monomer on the nanotube surface through the reaction of the epoxy ring with the carboxyl groups of nanotubes.

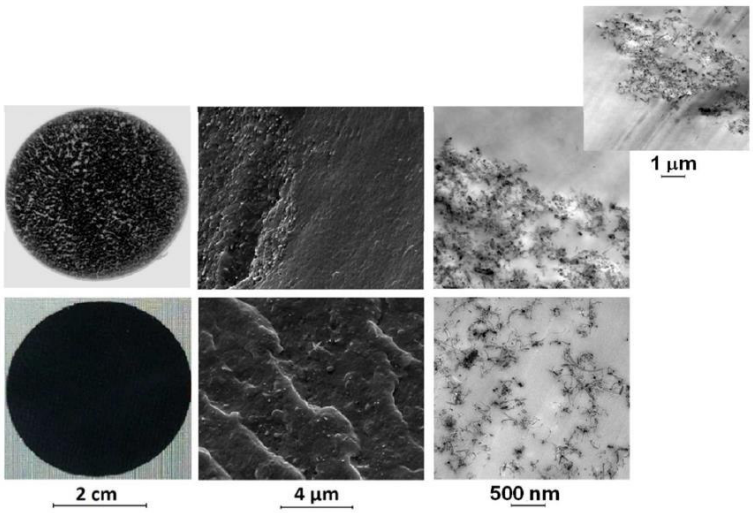

Figure 3.11 Comparison between a LC elastomer containing 1.5 wt.% of MWCNT-COOH (top row) and DS_1.5CNT (bottom row) evidencing the difference in CNT dispersion and sample homogeneity: optical images (left), SEM micrographs (center) and bright field TEM images (right).

As soon as the adduct formed, a stoichiometric amount of SA was added to the reacting mixture, and the samples were cured in oven at high temperature. According to this procedure, DS_xCNT samples were prepared, where x is the carbon nanotube content,

namely, 0.75, 1.5, or 3.0 wt %. The crosslinking of epoxy monomers with dicarboxylic acids, is a complex reaction, which proceeds through epoxy ring opening by the carboxyl group. [30] The produced hydroxyls in turn react with carboxylic acid or with unreacted epoxy molecules, giving rise to ester or ether groups, respectively. Furthermore, at high temperature homopolymerization of the diglycidyl derivative may also take place. [31]

Unlike the composite films containing MWCNT-COOH, which showed poor distribution and dispersion of nanotubes (Figure 3.12a), the optimized procedure based on the use of MWCNT-DOMS, yielded macroscopically homogeneous nanocomposite systems, as shown for DS_1.5CNT (Figure 3.11 bottom row). SEM and TEM analysis of this sample indicated the achievement of a good nanotube dispersion with no agglomeration. From SEM and TEM micrographs it is particularly evident that the synthesis through the formation of DOMS-functionalized adducts was an effective strategy to achieve good distribution of nanotubes within the epoxy matrix.

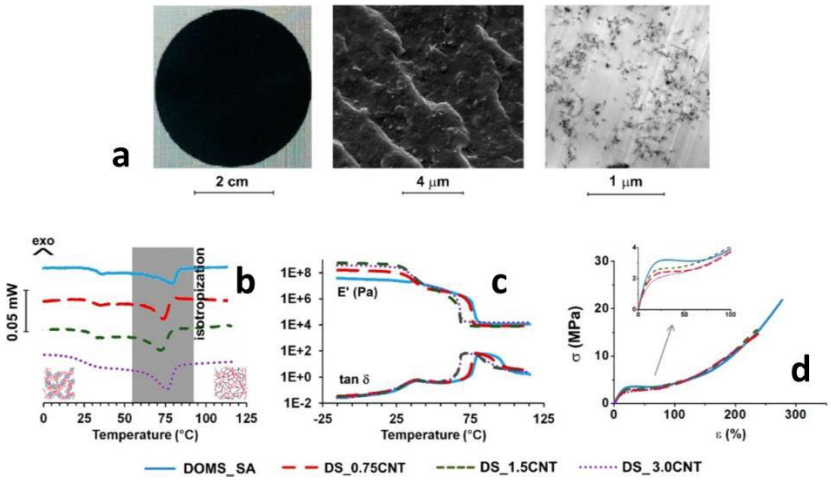

Figure 3.12 (a) Optical image (left), SEM micrograph (center), and bright-field TEM image (right) of DS_1.5CNT. (b) DSC traces (II heating scan) of DOMS_SA, DS_0.75CNT, DS_1.5CNT, and DS_3.0CNT. (c) Storage modulus (E') and tan δ of DOMS_SA, DS_0.75CNT, DS_1.5CNT, and DS_3.0CNT. (d) Stress−strain curves of DOMS_SA, DS_0.75CNT, DS_1.5CNT, and DS_3.0CNT

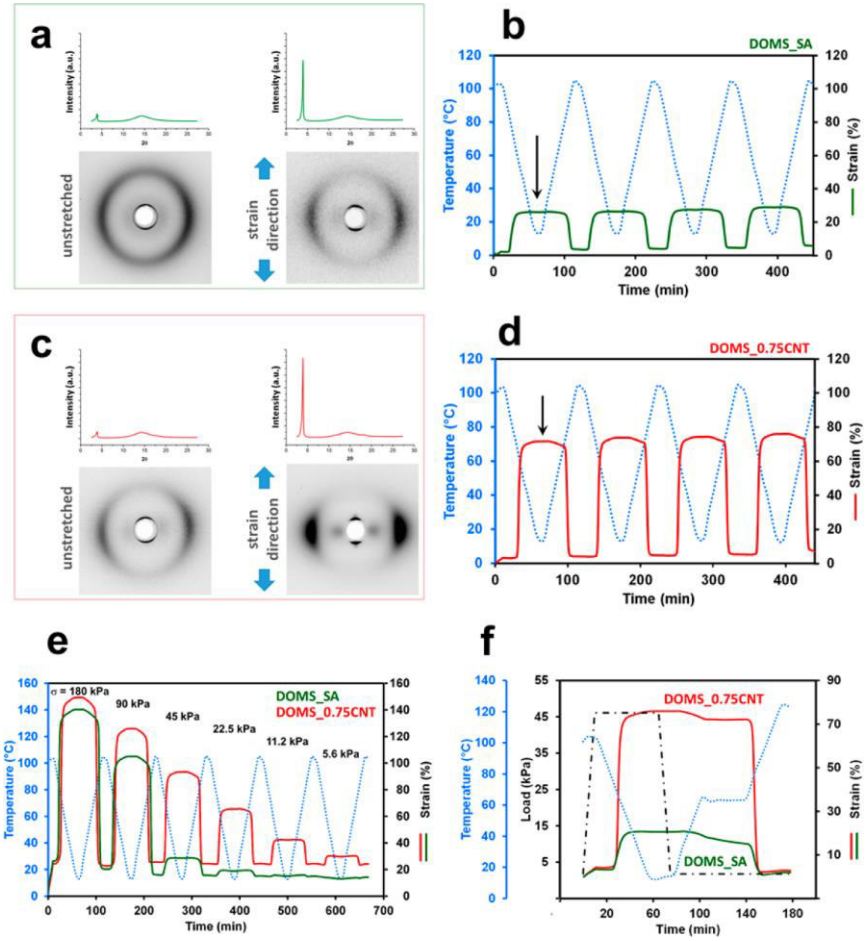

Figure 3.13 Thermomechanical properties of LC nanocomposite elastomers: (a) WAXD diffraction pattern of the unstretched (left) and the fully stretched DOMS_SA (right, corresponding to the elongated state indicated by the arrow in panel b) and corresponding intensity integrations along the meridian axis normalized to the reflection at higher 2θ (top left and right). (b) Four-cycle two-way shape-memory behavior of DOMS_SA under tensile loading corresponding to 45 kPa. (c) WAXD diffraction pattern of the unstretched (left) and the fully stretched DS_0.75CNT (right, see the arrow in panel d) and corresponding intensity integrations along the meridian axis normalized to the reflection at higher 2θ (top left and right). (d) Four-cycle two-way shape-memory behavior of DS_0.75CNT under tensile loading corresponding to 45 kPa. (e) Two-way shape-memory behavior of DOMS_SA and DS_0.75CNT under decreasing tensile loadings (σ = 180 to 5.6 kPa). (f) Triple shape-memory behavior of DOMS_SA and DS_0.75CNT

Independent of MWCNT presence and relative amount, smectic-A elastomers were obtained, [11] as inferred from DSC (Figure 3.12b) and WAXD analysis (Figure3.13a). WAXD pattern shows a weak reflection at about 2θ = 5.6°corresponding to a d-spacing of about

16 Å, comparable with the length of 15.1 Å calculated for DOMS mesogen. [30] Thermal transition temperatures and associated enthalpies of the prepared elastomers were determined by DSC and are listed in Table 3.1. DSC traces of DOMS_SA, DS_0.75CNT, DS_1.5CNT and DS_3.0CNT are reported in Figure 3.12b. All elastomers exhibited T_g values (second heating scan) varying from 32.1 °C (DOMS_SA) to 25.1 °C (DS_3.0CNT), with a progressive decrease due to the increased amount of nanotubes, which accounts for a higher mobility of polymer chains that in principle may affect shape memory behavior.

Table 3.1 DSC and DMA Characterization of DOMS-Based Elastomers

Sample	DSC								DMA			
	1st heating scan			Cooling scan		2nd heating scan						
	T_g [°C]	T_i [°C]	ΔH_i [J g^{-1}]	T_{ani} [°C]	ΔH_{ani} [J g^{-1}]	T_g [°C]	T_i [°C]	ΔH_i [J g^{-1}]	T_g [°C]	T_i [°C]	E'(50°C) [MPa]	E'(110°C) [kPa]
DOMS_SA	28.9	77.1	12.9	75.7	14.1	32.1	79.1	12.2	39.9	83.5	11.3	14.8
DOMS_0.75CNT	26.2	68.3	10.2	67.0	11.6	32.1	70.9	10.5	39.4	79.0	6.6	10.6
DOMS_1.5CNT	27.6	68.1	9.4	64.2	11.4	27.5	69.2	9.6	37.3	72.3	4.5	9.8
DOMS_3.0CNT	22.7	72.7	11.4	69.2	12.8	25.1	73.8	11.3	37.8	72.3	11.3	19.8

As for the phase behavior, DOMS_SA showed the highest value of isotropization temperature (T_i) and enthalpy (ΔH_i), whereas a decrease of these values was recorded for the composites, in particular for the samples containing 0.75 and 1.5 wt % of CNT (Table 3.1). Isotropization enthalpies were in the range of 9−13 J g^{-1}, comparable with typical ΔHi of smectic-A systems reported in literature. [30] The observed trend of Ti and ΔHi indicated that nanotubes are able to perturb the stability of the mesophase. [19] For LC polymers, the thermal stability of the LC mesophase is closely related to the morphology of the LC

domains formed, with smaller LC domains exhibiting lower isotropization temperatures. [22,32] In the present case, as the content of nanotubes increased up to 1.5 wt % the LC phase was destabilized, resulting in lower clearing temperatures and enthalpies. As the nanotube content further increased to 3.0 wt %, T_i and ΔH_i increased to values similar to those shown by DOMS_SA, likely due to CNT agglomeration phenomena.

Figure 3.12c shows storage modulus (E') and dissipation factor (tan δ) of the LCE as determined by dynamic mechanical analysis (DMA). Two thermal relaxations were observed, corresponding to glass transition and isotropization. The influence of nanotubes on the trends of T_g and T_i determined by DSC was confirmed by DMA. Moreover, storage moduli in the glassy region (T = 0 °C) increased with the content of MWCNT due to the stiffening effect of the rigid filler. For all the analyzed samples, at temperatures above T_i, the elastic moduli reached a plateau, indicating the formation of network structures (Figure 3.12c). Of particular note is that the value of E' in the rubbery region was affected by the presence of nanotubes.

In particular, as detailed in Table 3.1, above the isotropization temperature (110 °C) DOMS_SA showed a value of E' (about 15 kPa) higher than those of DS_0.75CNT and DS_1.5CNT (about 10 kPa). Only at higher CNT contents (DS_3.0CNT) did the network rigidity of the system start to increase again, reaching a value of E' of about 20 kPa at 110 °C. The prepared samples exhibited soft elasticity typical of LC elastomers, as displayed in Figure 3.12d for DOMS_SA, DS_0.75CNT, and DS_1.5CNT, in which stress−strain curves are reported. The uniaxial mechanical stress applied in the rubbery state was able to orient the networks efficiently. Three distinct regions were evident: At small strains, the samples underwent a linear deformation; at intermediate strains, a rubbery plateau-like region was recorded, in which the samples were deformed at almost constant stress. Within this segment, the samples experienced a polydomain-to-monodomain (P-M) transition under

the applied uniaxial mechanical stress, due to the soft-elastic response of the LC domains, which aligned along the stretching direction. Finally, at large strains, the modulus increased again, up to the breaking point of the samples. [33,34,35] Interestingly, the nanotubes were responsible for the lower stress threshold required to induce the P-M transition and shorter plateau regions of the filled elastomers in comparison with DOMS_SA (see inset of Figure 3.12d). This is due to the ability of LC domains to align rapidly under lower stress values in the presence of nanotubes. [21]

The presence of a stable polymer network and a reversible anisotropic/isotropic switching transition are considered the two requirements for the occurrence of shape memory. [36] In particular, thanks to their stress-induced P-M transition, the prepared LC epoxy elastomers are capable of reversible shape change under constant stress during temperature cycles, thus acting as temperature-induced shape-memory materials. [14] One of the most intriguing features of DOMS-based elastomers is represented by their ability to experience a significant two way shape-memory effect.

Figure 3.13b,d shows the four-cycle reversible thermo-actuation of DOMS_SA and DS_0.75CNT, evaluated by DMA in the film-tension geometry under a controlled load. Prior to start, samples were thermally equilibrated at 100 °C (T > Ti). After 10 min, a ramping force was applied up to a fixed tensile loading (σ = 45 kPa, loading rate = 4.5 kPa/min). Successively, the samples were cooled to T = 10 °C. During this step, all the samples spontaneously elongated due to soft-elastic response associated with anisotropization. When heated back to 100 °C, the samples gradually recovered their original length. The amplitude of this two-way actuation, calculated as the strain difference between 100 and 10 °C, was almost constant for each sample over many temperature cycles, thus indicating full reversibility and negligible creep. The cyclic elongation−contraction behavior is due to the reversible formation of well-aligned LC mesogen monodomains during cooling below

the clearing temperature. On heating, the anisotropic LC phase was disrupted, and the material recovered its original shape owing to entropic elasticity. Moreover, as already reported for epoxy based LCE, [14] the extent of actuation progressively increased on increasing the applied load (Figure 3.13e). Interestingly, the presence of nanotubes had two important consequences on thermo-mechanical behavior of DOMS-based elastomer composites. First, the two-way actuation was strongly dependent on the nanotube content. Neat DOMS_SA showed an elongation of about 20% during cooling under an uniaxial load corresponding to 45 kPa stress. In stark contrast, all the nanocomposite samples exhibited a dramatic enhancement of the thermal actuation extent, which was more significant at lower nanotube content. In particular, DS_0.75CNT spontaneously stretched up to 75%, representing a 3-fold elongation compared to that of DOMS_SA (Figure3.13b,d).

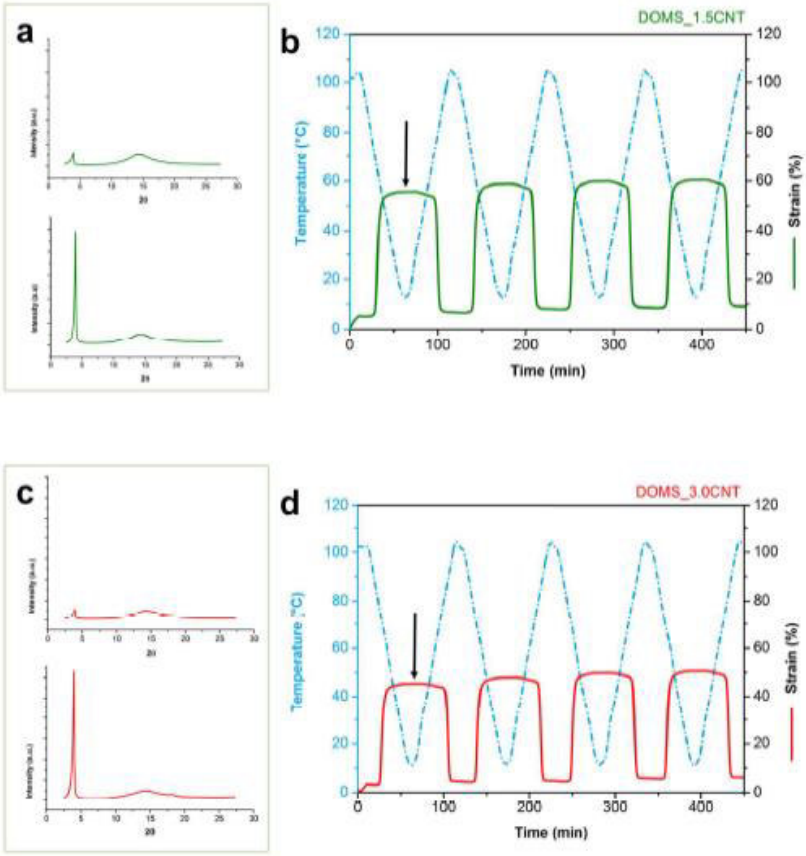

Figure 3.14 a) Intensity integrations along the meridian axis of WAXD diffraction pattern of the unstretched (top) and the fully stretched form of DS_1.5CNT (bottom, see the arrow in Fig. 3.14b); b) four-cycle two-way shape memory behavior of DS_1.5CNT under a tensile stress of 45 kPa; c) intensity integrations along the meridian axis of WAXD diffraction pattern of the unstretched (top) and the fully stretched form of DS_3.0CNT (bottom, see the arrow in Fig. 3.14d); d) four-cycle two-way shape-memory behavior of DS_3.0CNT under a tensile stress of 45 kPa.

As the nanotube content further increased, a slight reduction in actuation capability was observed (Figure 3.14). In addition, nanotubes remarkably decreased the stress threshold value needed to trigger shape recovery, with the nanocomposites being able to undergo appreciable actuation even at small loadings. As shown in Figure 3.12d, a uniaxially aligned film of DS_0.75CNT reached about 10% strain at a 5.6 kPa applied stress. Interestingly, the same loading condition did not induce any shape change on neat DOMS_SA.

WAXS was performed to evaluate structural changes on the nanoscale for neat DOMS_SA and DS_0.75CNT before and after thermally controlled actuation under an applied load of 45 kPa. The 2D WAXS diffraction patterns and the corresponding radial intensity integrations along the meridian direction, normalized with respect to the halo at higher 2θ, are displayed in Figure 3.13a,c. The 2D diffraction pattern of DOMS_SA showed a broad external halo centered at $2\theta_1$ = 20.0° that results from the overlap of the amorphous halo typical of epoxy resins and the diffraction peak corresponding to the intermolecular spacing between the rodlike liquid crystalline mesogens. [37] According to the Bragg equation, the calculated d1-spacing was 4.4 Å. A sharp inner reflection centered at $2\theta_2$ =5.6° (d_2-spacing =15.8 Å) was also visible in the diffraction pattern, indicating the formation of a smectic-A LC phase. [29] As evidenced by the slight polarization of the reflection observed for DS_0.75CNT, nanotubes promoted orientation of the LC smectic domains even on the unstressed sample. The order parameter, S, was determined by

elaborating the diffraction pattern as described in the Experimental Section. Indeed, values of 0.41 and 0.51 were calculated for DOMS_SA and DS_0.75CNT, respectively, confirming that nanotubes effectively contribute to the alignment of mesogens.

The enhanced actuation induced by nanotubes clearly affects the diffraction patterns of stretched samples and the corresponding meridian integrations. Weak orientation was noticed for DOMS_SA (Figure 3.13a, right), in agreement with the low elongation extent experienced by the sample during cooling under stress (S = 0.54). Instead, DS_0.75 CNT stretched under the same conditions showed an intense reflection at the equator (Figure 3.13c, right) due to the scattering of the amorphous phase and the neighboring mesogens (d_1-spacing = 4.4 Å), along with a sharp meridional reflection attributed to the periodic layers of the smectic LC structures (d_2-spacing =15.5 Å). This difference is even more clear from the analysis of the meridian integrations, displayed in Figure 3.13a,c (top). The high extent of polarization was related to the pronounced orientation of the smectic layers perpendicular to the stress direction promoted by the nanotubes. Indeed, for this sample, an S value of 0.70 was calculated.

Thermomechanical characterization of the LCE also highlighted a characteristic triple-shape-memory effect. [38] Figure 3.13f shows the triple-shape-memory cycle of DOMS_SA and DS_0.75 CNT. In the programming step, the LCE was stretched by a target stress of 45 kPa at a temperature of 100 °C. The sample was then cooled to 10 °C while the stress was maintained. During this step, the sample was stretched (about 20 and 75% with respect to the initial shape for DOMS_SA and DS_0.75 CNT, respectively) due to the transition from isotropic to LC monodomain, and the temporary shape was fixed. About 10 min after the temperature reached 10 °C, the imposed stress was removed; then, the sample was first heated to 60 °C then to 120 °C under stress-free conditions.

In this free recovery step, when the temperature was ramped, the strain gradually decreased, indicating the tendency to recover the original shape. However, as the temperature ramping was stopped to 60 °C, the samples reached a stable intermediate shape with about 15 and 70% residual strain for DOMS_SA and DS_0.75 CNT, respectively. This first thermomechanical response was due to the relaxation associated with Tg. When temperature was further increased to 120 °C, the samples underwent LC to isotropic transition, and the strain gradually decreased to zero, indicating recovery of the original shape. All the tested samples showed triple-shape behavior, and the thermomechanical response was affected by the presence and amount of MWCNT.

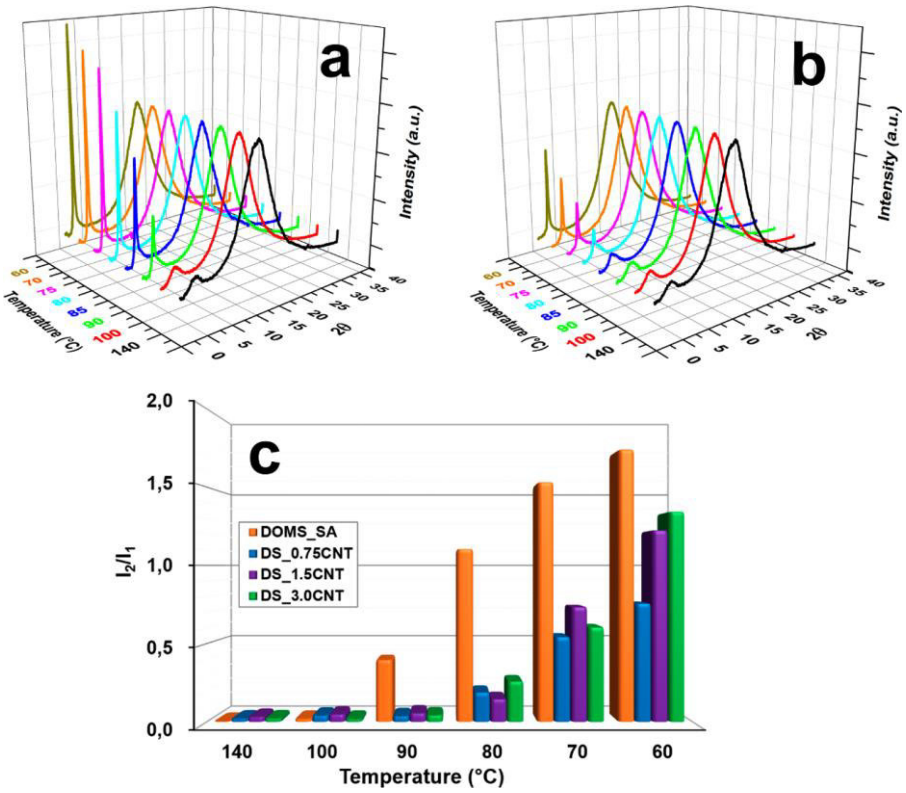

Figure 3.15 Temperature-controlled X-ray diffractometry. Intensity integrations along the meridian axis of diffrattograms collected at different temperatures during cooling of (a) DOMS_SA and (b) DS_0.75CNT. All spectra are normalized to the reflection at higher 2θ angle. (c) Temperature dependence of the intensity ratio (I_2/I_1) of the peaks corresponding to reflections at lower and higher 2θ angles, respectively

A comprehensive study of the effect of CNT on the triple-shape-memory behavior of this class of LCE nanocomposites is outside the scope of this paper and will be the subject of future investigation.

A further insight of the effect of nanotubes on the phase behavior of elastomers upon cooling is given in Figure 3.15a,b, where temperature-controlled X-ray diffractograms are reported for DOMS_SA and DS_0.75CNT, respectively. Samples were heated at a temperature above Ti and then gradually cooled to low temperatures, inducing elastomer anisotropization.

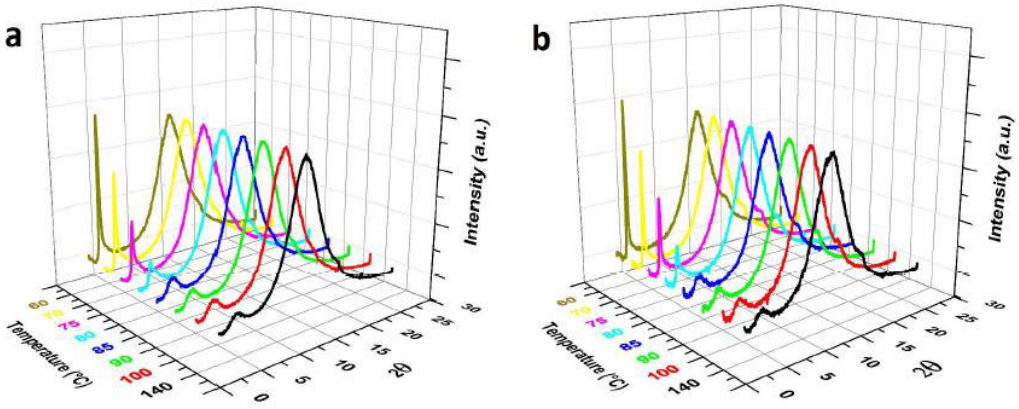

Figure 3.16 Temperature-controlled X-ray diffractometry. Intensity integrations along the meridian axis of diffractograms collected at different temperatures during cooling of: a) DS_1.5CNT; b) DS_3.0CNT. All spectra are normalized to the reflection at higher 2θ angle

Figure 3.15a shows the diffractograms collected in the temperature range between 140 and 60 °C, displaying the evolution of the two characteristic reflection peaks for DOMS_SA. The $2\theta_1$ peak due to the overlap of the amorphous contribution and the scattering of neighboring mesogens in the smectic layers shifted from 19.2 to 19.9° upon cooling (Figure 3.16), d_1-spacing decrease from 4.62 to 4.46 Å). Additionally, the full width at half-maximum (FWHM) varied from 7.2 to 6.0°, indicating the achievement of a higher-order

degree. These results indicate that during cooling a progressive ordering of neighboring mesogens occurs leading to a gradual increase of the component at higher 2θ at the expense of the amorphous halo in the convoluted reflection at 19.2°. Moreover, at high temperatures (T = 140 and 100 °C) a second less intense reflection was visible at low 2θ values, attributed to the scattering of randomly stacked mesogens in the isotropic phase.

As the temperature decreased, a sharp, intense peak gradually formed at 2θ2 = 5.7° (d2 = 15.5 Å), further indicating the organization of the stacked LC domains into an ordered smectic structure. The same trend was observed for DS_0.75CNT (Figure 3.15b). However, in this case the appearance of the smectic peak occurred at lower temperatures.

Moreover, the intensity was much lower with respect to DOMS_SA, suggesting that nanotubes inhibited the LC phase formation. On cooling, this sample also showed a less significant shift of the convoluted reflection at higher 2θ (from 19.3 to 19.7°) with respect to DOMS_SA. In order to quantitatively evaluate the effect of nanotubes on phase behavior, Figure 3.15c reports the I_2/I_1 ratio as a function of temperature, where I2 and I1 are the intensities of peaks centered at $2\theta_2$ and $2\theta_1$, respectively. The inhibiting effect of CNT is particularly significant for DS_0.75CNT, whereas it is less relevant for DS_1.5CNT and DS_3CNT (see also Figure 3.17 for a more accurate estimation). These results are in agreement with the lower isotropization temperatures and enthalpies determined by DSC for CNT-filled elastomers.

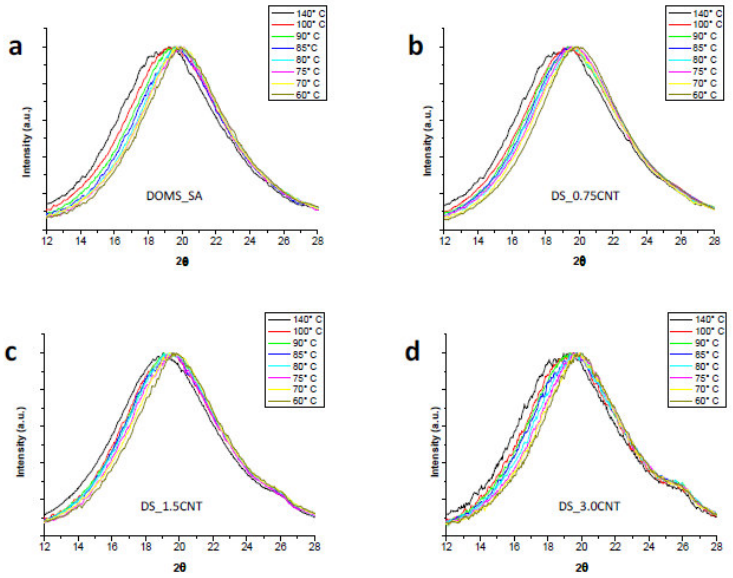

Figure 3.17 Temperature-controlled X-ray diffractometry evidencing the peak shift due to gradual increase of the component at higher 2θ at the expense of the amorphous halo in the broad convoluted reflection centred at about 19.2° (see Figure 3.15a,b and Figure 3.16). Intensity integrations in the 2θ range 12-28° along the meridian axis of diffractograms collected at different temperatures during cooling of: a) DOMS_SA; b) DS_0.75CNT; c) DS_1.5CNT; d) DS_3.0CNT. All spectra are normalized to the reflection at higher 2θ angle. Please note that the shoulder at about 25.5° that can be observed in b, c and d, is a third component due to the presence of MWCNT (corresponding d-spacing = 0.35 nm).

In order to correlate the thermomechanical response and the nanoscale structure of the samples with their morphology on the microscale, SEM analysis was carried out on cryogenically fractured surfaces of unstretched and stretched samples exhibiting monodomain LC phase formed during the cooling step under constant load. Figure 3.18 displays the morphological features evidenced by SEM and the related sketched nanostructure arrangements of mesogens during thermomechanical tests at the three major deformation states: (i) unstretched sample at room temperature, (ii) sample under an applied load of 45 KPa at T > Ti, and (iii) stretched sample after anisotropization. Both DOMS_SA (Figure 3,.18a) and DS_0.75CNT (Figure 3.18b) were represented and compared. Unstretched DOMS_SA (Figure 3.18a, left) and DS_0.75CNT (Figure 3.18b, left) showed

comparable morphologies. The samples evidenced the presence of randomly propagating fracture surfaces. Since LC domains deviate crack propagation, SEM micrographs of fractured surfaces indicate that for both samples LC domains are not aligned along preferential orientations. [22]

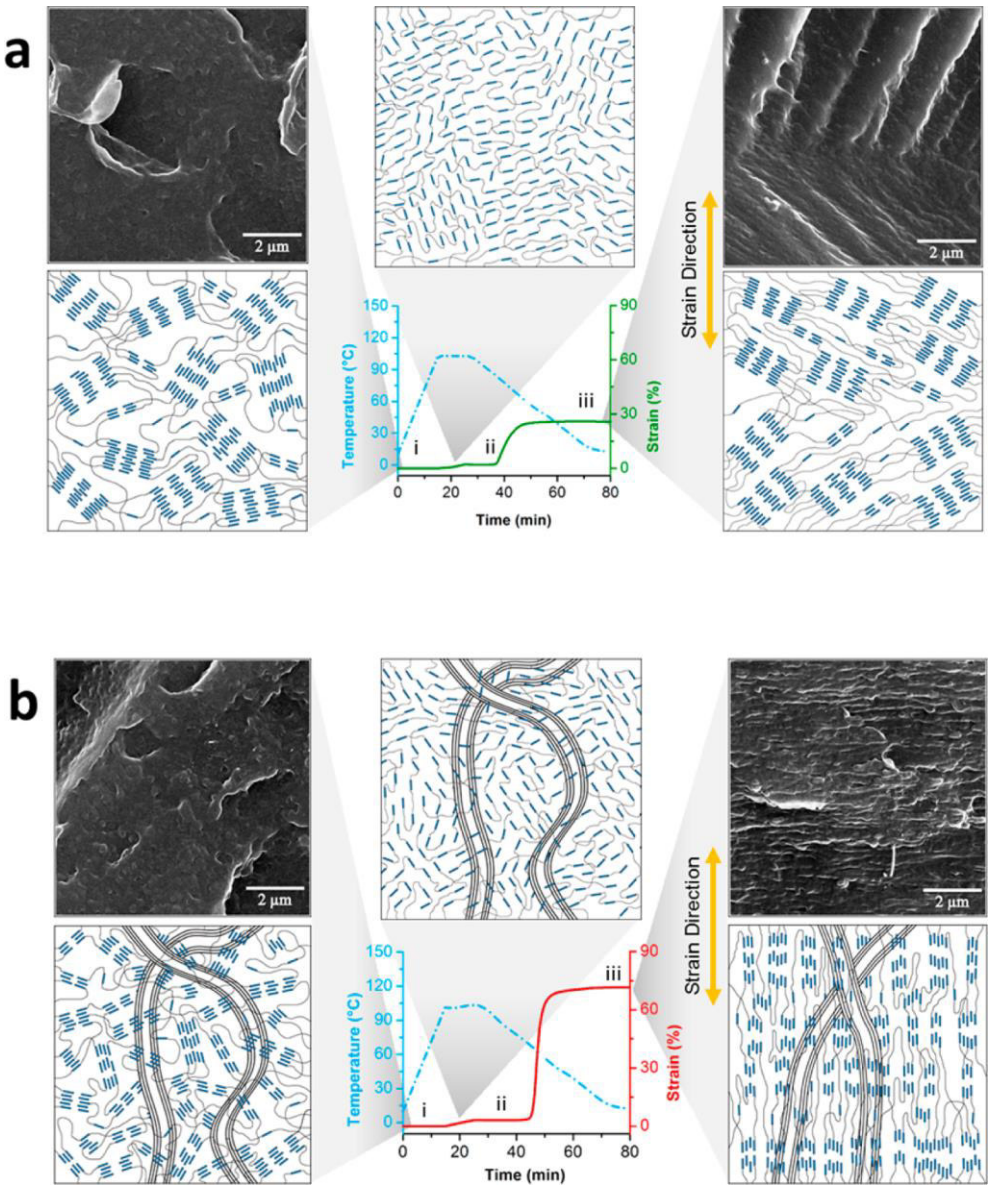

Figure 3.18 SEM micrographs and corresponding schematic representation of the structure of (a) DOMS_SA and (b) DS_0.75CNT at different stages of the thermomechanical test: (i) unstretched samples at room temperature; (ii) samples at T > Ti under an applied load of 45 KPa; and (iii) stretched samples after anisotropization. Mesogens are represented as blue rods. The walls of MWCNT are schematized with black lines. Mesogens are stacked in smectic LC domains at stages i and iii. At stage iii, a higher orientation degree

is evident for the sample DS_0.75CNT. Above T_i (stage ii), the disruption of the smectic phase is shown for both samples.

However, a significant difference is observed by comparing the samples obtained upon cooling under constant load. For both samples, the progressive development of a LC monodomain structure under loading induced the formation of oriented fracture surfaces. In the particular case of DOMS_SA (whose final elongation was 20% under an applied stress of 45 kPa), the presence of parallel fracture surfaces arranged in a micrometer-sized chevronlike structure is evident.

This morphological feature may reflect the generation of a complex layered structure at a mesoscale, which in turn is induced at a molecular level by the arrangement of mesogens progressively orientating along the stretching direction, as qualitatively sketched in Figure 3.18a (right). According to the above considerations, SEM image suggests that in the case of DOMS_SA the polydomain to monodomain transition was incomplete (Figure 3.18a, top right).

On the contrary, in the case of DS_0.75CNT, which spontaneously stretched up to 75%, the whole sample showed fracture planes perfectly aligned perpendicularly to the stretching direction (Figure 3.18b, right). The presence of carbon nanotubes allowed the sample to easily reach the end of the polydomain to monodomain plateau (see also Figure 3.13d), thus yielding in the same conditions a highly oriented system. This phenomenon can be attributed to the combined effect of the LC phase stability and network softness. In the case of DOMS_SA, the network rigidity above the isotropization temperature was higher than those shown by DS_0.75CNT and DS_1.5CNT, as evidenced by DMA analysis. Therefore, at low CNT contents, the combination between a softer network and a sufficient degree of liquid crystallinity resulted in higher strain values observed during cycling

thermomechanical tensile testing. [22] For higher CNT contents (3 wt % onward), the increase of network rigidity hinders polymer chain mobility, resulting in a slight reduction of actuation and recovery extent, as reported in Figure 3.14d for DS_3.0CNT.

The electrical behavior of the DOMS based nanocomposites was evaluated as a function of the CNT loading. In Figure 3.19 the electrical volume resistivity of neat resin and the optimized nanocomposites is reported.

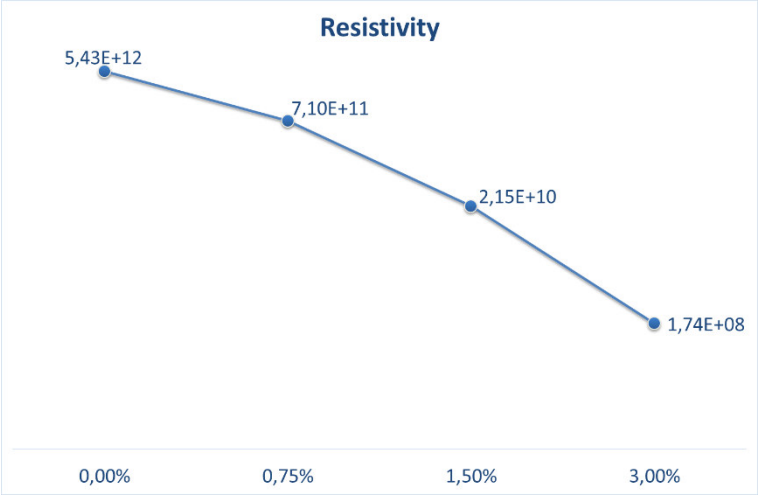

Figure 3.19 Volume resistivity (Ωcm^{-1}) as a function of MWCNT content in DOMS-based nanocomposites

As reported in the figure the resistivity decreases, as the content of MWCNTs increases. By observing the graph, it seems that the electrical percolation threshold was still not reached. But, even if a further increase would have been strongly detrimental for the mechanical properties, a sample with higher content of CNT was prepared (6%). In that case, a resistivity of $1{,}57 \times 10^{8}\ \Omega cm^{-1}$, proving that the percolation threshold was already reached at 3.00% content of nanofiller.

Such a decreasing of resistivity enables the electro-actuation of the SME, through Joule effect, as displayed in Figure 3.20 (for this attempt, a content of 12 wt% was used).

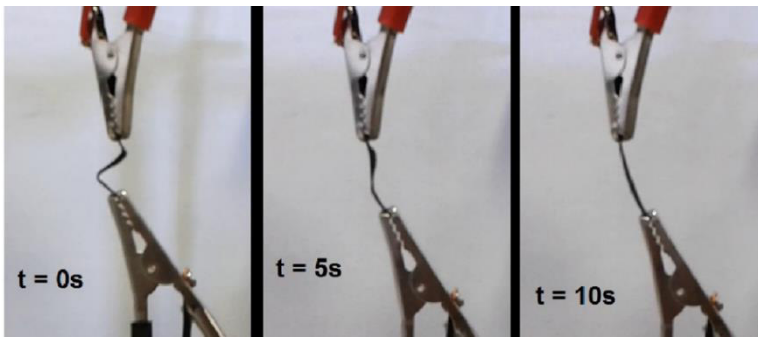

Figure 3.20 Time sequence of SME due to Joule effect.

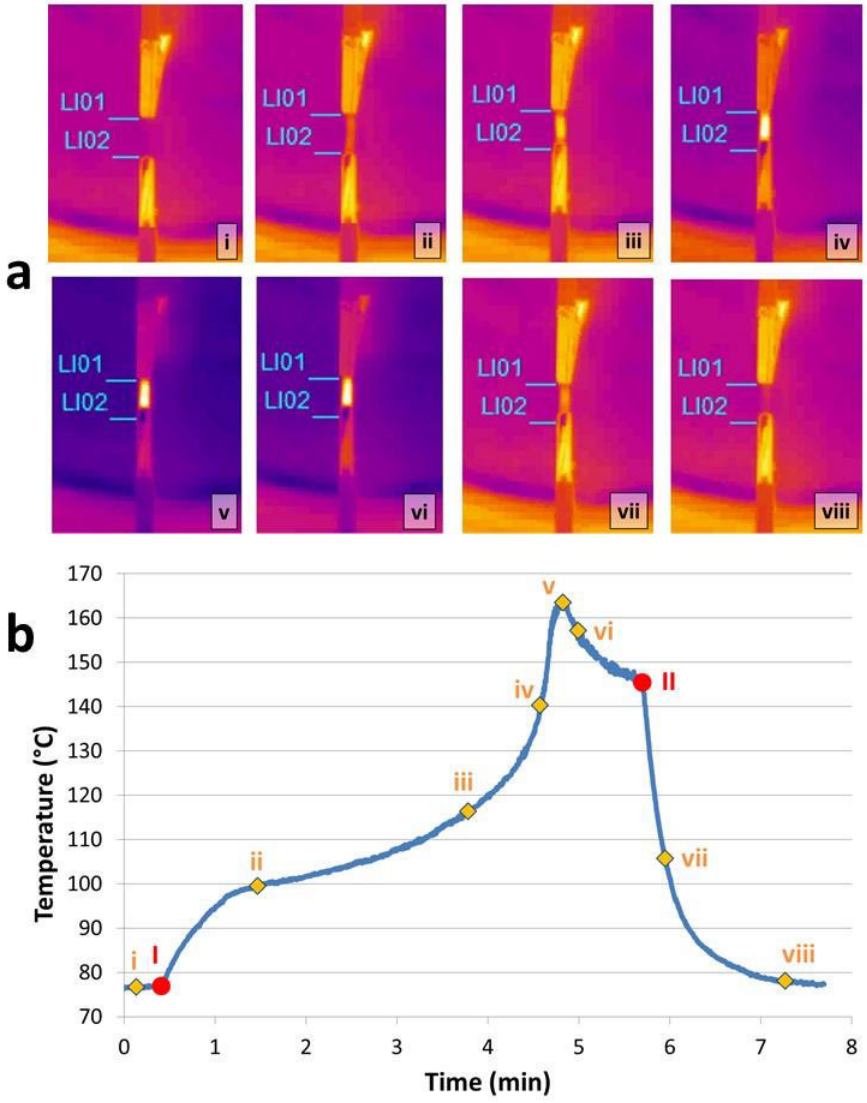

Figure 3.21 Temporal evolution of SME due to resistive heating. a) Picture sequence took at different times with thermo-camera (distance between cyan lines is 15 mm). b) Line refers to the evolution of the temperature measured in the sample region between LI01 and LI02 in a). Red points (I) and (II) are the points at which the voltage was turned ON and turned OFF, respectively.

In order to evaluate SME actuation through resistive heating, two electrodes were connected to a deformed nanocomposite specimen. Then, as soon as the voltage was applied (800 V), the sample started to switch from temporary shape to its permanent shape (Figure 3.20). The complete shift occurs in few seconds.

To prove that a conductive network made of MWCNT particles formed, the experiment just described was repeated, and the temperature recorded by means of an infrared camera, as shown in Figure 3.21, where the temporal evolution of SME due to resistive heating is shown. The sequence in Figure 3.21a was acquired in a time interval of about 8 minutes. The brighter areas represent higher temperature regions. The distance between the two cyan lines is 15 mm, that is the length of the sample deformed in its temporary shape. As it is outlined by the sequence, from (i) through (viii), the sample contracts, since it recovers its permanent shape. The temperature measured in the sample region between LI01 and LI02 is reported in figure 3.21b as a function of time. It is worth noticing that red dots represents the moment at which the voltage was turned on (I) and turned off (II).

As it is shown, the specimen was at about 75 °C when the observation started. After 30 seconds the voltage was turned on and the temperature of the sample started to rise, reaching a value of 165 °C in few minutes. In this time interval the permanent shape is recovered. Then, the temperature started to decrease immediately afterwards.

Furthermore, the specimen experienced a faster temperature decrease when the voltage was turned off, proving that the material became conductive with the inclusion of the carbon nanotubes, enabling electro-actuation of the SMPNC.

3.4. Conclusions

A series of new smectic epoxy nanocomposites have been developed incorporating surface-modified multiwalled carbon nanotubes at different loading levels into a LC elastomer. Besides the demonstrated high performance in the two-way shape-memory effect for the produced nanocomposites, it is significant that the approach used affords a large degree of tuning of the thermomechanical response that may enable the design of new shape-memory materials for target applications. For example, one can control the transition temperatures and the stress threshold required for the actuation by selecting the amount of nanotubes dispersed into the host matrix or stimulate the material at different thermomechanical recovery conditions to achieve triple-shape-memory response. Additionally, a more in-depth understanding of the microstructure− property relationships in nanocomposites is achieved, allowing a strict control on mechanical thermo-actuation of the realized systems. In the end, electro-actuation due to the enhancement of electrical conductivity was proved.

3.5. References

1 Zarek, M.; Layani, M.; Cooperstein, I.; Sachyani, E.; Cohn, D.; Magdassi, S. 3D Printing of Shape Memory Polymers for Flexible Electronic Devices. Adv. Mater. 2016, 28, 4449

2 Zhang, J.; Wu, G.; Huang, C.; Niu, Y.; Chen, C.; Chen, Z.; Yang, K.; Wang, Y. Unique Multifunctional Thermally-Induced Shape Memory Poly(p-dioxanone)−Poly(tetramethylene oxide)glycol Multiblock Copolymers Based on the Synergistic Effect of Two Segments. J. Phys. Chem. C 2012, 116, 5835−5845

3 Liu, Y.; Zhao, J.; Zhao, L.; Li, W.; Zhang, H.; Yu, X.; Zhang, Z. High Performance Shape Memory Epoxy/Carbon Nanotube Nanocomposites. ACS Appl. Mater. Interfaces 2016, 8, 311−320

4 Zhao, J.; Chen, M.; Wang, X. Y.; Zhao, X. D.; Wang, Z. W.; Dang, Z. M.; Ma, L.; Hu, G. H.; Chen, F. H. Triple Shape Memory Effects of Cross-Linked Polyethylene/Polypropylene Blends with Cocontinuous Architecture. ACS Appl. Mater. Interfaces 2013, 5, 5550−5556.

5 Ahn, S.-K.; Deshmukh, P.; Gopinadhan, M.; Osuji, C. O.; Kasi, R. M. Side-Chain Liquid Crystalline Polymer Networks: Exploiting Nanoscale Smectic Polymorphism to Design Shape-Memory Polymers. ACS Nano 2011, 5, 3085−3095

6 Hu, J.; Zhu, Y.; Huang, H.; Lu, J. Recent Advances in Shape− Memory Polymers: Structure, Mechanism, Functionality, Modeling and Applications. Prog. Polym. Sci. 2012, 37, 1720−1763

7 Hager, M. D.; Bode, S.; Weber, C.; Schubert, U. S. Shape Memory Polymers: Past, Present and Future Developments. Prog. Polym. Sci. 2015, 49−50, 3−33

8 Zhao, Q.; Qi, H. J.; Xie, T. Recent Progress in Shape Memory Polymer: New Behaviors, Enabling Materials, and Mechanistic Understanding. Prog. Polym. Sci. 2015, 49−50, 79−120.

9 Michal, B. T.; McKenzie, B. M.; Felder, S. E.; Rowan, S. J. Metallo-, Thermo-, and Photoresponsive Shape Memory and Actuating Liquid Crystalline Elastomers. Macromolecules 2015, 48, 3239−3246.

10 Ortiz, C.; Ober, C. K.; Kramer, E. J. Stress Relaxation of A Main-Chain, Smectic, Polydomain Liquid Crystalline Elastomer. Polymer 1998, 39, 3713−3718

11 Ambrogi, V.; Giamberini, M.; Cerruti, P.; Pucci, P.; Menna, N.; Mascolo, R.; Carfagna, C. Liquid Crystalline Elastomers Based on Diglycidyl Terminated Rigid Monomers and Aliphatic Acids. Part 1. Synthesis and Characterization. Polymer 2005, 46, 2105−2121

12 Giamberini, M.; Cerruti, P.; Ambrogi, V.; Vestito, C.; Covino, F.; Carfagna, C. Liquid Crystalline Elastomers On Diglycidyl Terminated Rigid Monomers And Aliphatic Acids. Part 2. Mechanical Characterization. Polymer 2005, 46, 9113−9125

13 Qin, H.; Mather, P. T. Combined One-Way and Two-Way Shape Memory in A Glass-Forming Nematic Network. Macromolecules 2009, 42, 273−280.

14 Pei, Z.; Yang, Y.; Chen, Q.; Terentjev, E. M.; Wei, Y.; Ji, Y. Mouldable Liquid-Crystalline Elastomer Actuators with Exchangeable Covalent Bonds. Nat. Mater. 2013, 13, 36−41

15 Liu, W.; Guo, L.-X.; Lin, B.-P.; Zhang, X.-Q.; Sun, Y.; Yang, H. Near-Infrared Responsive Liquid Crystalline Elastomers Containing Photothermal Conjugated Polymers. Macromolecules 2016, 49, 4023−4030.

16 Evans, J. S.; Sun, Y.; Senyuk, B.; Keller, P.; Pergamenshchik, V. M.; Lee, T.; Smalyukh, I. I. Active Shape-Morphing Elastomeric Colloids in Short-Pitch Cholesteric Liquid Crystals. Phys. Rev. Lett. 2013, 110, 187802

17 Yang, H.; Liu, J.-J.; Wang, Z.-F.; Guo, L.-X.; Keller, P.; Lin, B.-P.; Sun, Y.; Zhang, X.-Q. Near-Infrared-Responsive Gold Nanorod/Liquid Crystalline Elastomer Composites Prepared by Sequential Thiol-Click Chemistry. Chem. Commun. 2015, 51, 12126

18 Gulotty, R.; Castellino, M.; Jagdale, P.; Tagliaferro, A.; Balandin, A. Effects of Functionalization on Thermal Properties of Single-Wall and Multi-Wall Carbon Nanotube-Polymer Nanocomposites. ACS Nano 2013, 7, 5114

19 Ji, Y.; Marshall, J. E.; Terentjev, E. M. Nanoparticle-Liquid Crystalline Elastomer Composites. Polymers 2012, 4, 316−340

20 Lynch, M. D.; Patrick, D. L. Organizing Carbon Nanotubes with Liquid Crystal Solvents. Nano Lett. 2002, 2, 1197−1201

21 Ji, Y.; Huang, Y. Y.; Rungsawang, R.; Terentjev, E. M. Dispersion and Alignment of Carbon Nanotubes in Liquid Crystalline Polymers and Elastomers. Adv. Mater. 2010, 22, 3436−3440

22 Li, Y.; Pruitt, C.; Rios, O.; Wei, L.; Rock, M.; Keum, J.; McDonald, A. G.; Kessler, M. Controlled Shape Memory Behavior of a Smectic Main-Chain Liquid Crystalline Elastomer. Macromolecules 2015, 48, 2864−2874

23 Ambrogi, V.; Gentile, G.; Ducati, C.; Oliva, M. C.; Carfagna, C. Multiwalled Carbon Nanotubes Functionalized with Maleated Poly-(Propylene) by A Dry Mechano-Chemical Process. Polymer 2012, 53, 291−299.

24 Gentile, G.; Ambrogi, V.; Cerruti, P.; Di Maio, R.; Nasti, G.; Carfagna, C. Pros and Cons of Melt Annealing on the Properties of MWCNT/Polypropylene Composites. Polym. Degrad. Stab. 2014, 110, 56−64.

25 Lama, G. C.; Nasti, G.; Ambrogi, V.; Cerruti, P.; Gentile, G.; Carfagna, C. Epoxy Elastomers Reinforced with Functionalized Multi- Walled Carbon Nanotubes as Stimuli-Responsive Shape Memory Materials. AIP Conf. Proc. 2014, 1599, 182−185

26 H. Lee, K. Neville (1967). Handbook of epoxyresins. New York: McGrawHill; [chapter 11].

27 K.J. Saunders (1988). Organic polymer chemistry. New York: Chapman andHall; p. 412–427

28 M. Giamberini, E. Amendola, C.Carfagna (1997):MacromolChem Phys;198:3185–96.

29 V. Ambrogi, M. Giamberini, P. Cerruti, P. Pucci, N. Menna, R. Mascolo, C. Carfagna (2005): Liquid crystalline elastomers based on diglycidyl terminated rigid monomers and aliphatic acids. Part 1. Synthesis and characterization. Polymer 46, 2105–2121

30 Giamberini, M.; Amendola, E.; Carfagna, C. Liquid Crystalline Epoxy Thermosets. Mol. Cryst. Liq. Cryst. Sci. Technol., Sect. A 1995, 266, 9−22.

31 Cosco, S.; Ambrogi, V.; Musto, P.; Carfagna, C. Urea-Formaldehyde Microcapsules Containing An Epoxy Resin: Influence of Reaction Parameters on the Encapsulation Yield. Macromol. Symp. 2006, 234, 184−192

32 Donald, A. M.; Windle, A. H.; Hanna, S. Liquid Crystalline Polymers; Cambridge University Press: Cambridge, U.K., 2006.

33 Sanchez-Ferrer, A.; Finkelmann, H. Polydomain−Monodomain Orientational Process in Smectic-C Main-Chain Liquid-Crystalline Elastomers. Macromol. Rapid Commun. 2011, 32, 309−315

34 Dey, S.; Agra-Kooijman, D. M.; Ren, W.; McMullan, P. J.; Griffin, A. C.; Kumar, S. Soft Elasticity in Main Chain Liquid Crystal Elastomers. Crystals 2013, 3, 363−390

35 Giamberini, M.; Ambrogi, V.; Cerruti, P.; Carfagna, C. Viscoelasticity of Main Chain Liquid Crystalline Elastomers. Polymer 2006, 47, 4490−4496.

36 Meng, H.; Li, G. A Review of Stimuli-Responsive Shape Memory Polymer Composites. Polymer 2013, 54, 2199−2221

37 Choi, E.-J.; Ahn, H.-K.; Lee, J. K.; Jin, J.-I. Liquid Crystalline Twin Epoxy Monomers Based on Azomethine Mesogen: Synthesis and Curing with Aromatic Diamines. Polymer 2000, 41, 7617−7625

38 Ahn, S.-K.; Kasi, R. M. Exploiting Microphase Separated Morphologies of Side-Chain Liquid Crystalline Polymer Networks for Triple Shape Memory Properties. Adv. Funct. Mater. 2011, 21, 4543−4549

CHAPTER 4

Oxidation of graphite nanoplatelets (GNPs)

4.1. Introduction

Graphene is defined as a flat monolayer of carbon atoms tightly packed into a two-dimensional honeycomb lattice,[1] and is the basis for the realization of several advanced materials and devices, with applications in a large number of sectors that are expected to revolutionize multiple industrial fields.[2]

Key factors for the realization of advanced systems are understanding and controlling the chemistry and the processing of graphene and graphene derivatives. In particular, the realization of aqueous dispersions of graphene oxide (GO) was already in 2008 presented as an effective method for the processing of graphene.[3,4]

Despite the large scientific interest on this material, a few papers report comprehensive information on the effects of the oxidation degree on GO physico-chemical and structural properties, processability, adsorption properties of gases and organic dyes from water solutions and finally on the available specific surface area of GO in different physical states, such as dry GO self-assembled through different processes, or water dispersed GO.

Dreyer et al., [5] deeply investigated the chemistry of graphene oxide. More recently, Krishnamoorthy et al.,[6] detailed the different types of oxygen containing functional groups formed at increased oxidation degrees and how they influence the structural properties of GO. Even if these papers are fundamental for the understanding and for the qualitative and quantitative estimation of the effects of the oxidation process of graphene, they did not deal with the processing and the adsorption properties of the final materials.

As concerning the self-assemby of GO in different conditions, a very broad reviews[4] discusses the phenomena occurring during the self-concentration of GO at various

interfaces, also showing possible applications of the graphene based systems developed. Amongst the processing methodologies available to tailor graphene-based structures, particularly interesting is the self-assembly at the liquid-air interface[7,8], in view of obtaining 2D architectures. In particular, the effect of the oxidation degree of GO on the water mediated interlayer interactions has been investigated through molecular dynamics simulations,[9] explaining the mechanism at the basis of self-concentration of GO at the liquid-air interface. Another relevant aspect of GO 2D structures is related to its adsorption properties, and to the estimation of the surface area of these systems available to physical and chemical interactions with different adsorbates, such as gases and water-soluble dyes. Gadipelli and Guo[10] well summarized the gas sorption properties of graphene and derivatives, whereas Yan et al. [11] detailed the effect of the oxidation degree of graphene oxide on the adsorption of methylene blue from water solutions. Nevertheless, further insight on these aspects would be still needed to correlate the adsorption properties of GO to the level of interactions occurring between GO sheets.

Starting from this basis, the work here presented is focused on the effect of the oxidation degree on the chemical and physical properties, including the surface area, of GO samples realized by a modified Hummers method from commercial graphite nanoplatelets (GNP) and processed through water casting. In a first phase, a multi-technique characterization was performed to correlate the oxidative conditions adopted to the final oxidation degree of the obtained GO. Then, morphological and structural properties cast GO films realized by self-assembly at the liquid-air interface were evaluated and correlated to the different oxidation degree of the starting water-dispersed GO samples. Finally, the specific surface area of the realized systems was evaluated by BET analysis, and the results were discussed in relation to their structural

properties and to specific surface area measurements carried out on GO water dispersions by methylene blue adsorption tests.

4.2. Experimental

4.2.1. Materials

Graphite nanoplatelets (GNP) grade C, average lateral dimensions 1-2 μm according to the datasheet provided by the supplier, were purchased from XG Science (Lansing, MI, USA).

Sulfuric acid (H_2SO_4, reagent grade, 96% wt/wt in H_2O), hydrochloric acid (HCl, reagent grade, 37% wt/wt in H_2O), potassium permanganate ($KMnO_4$, > 99.0%), hydrogen peroxide solution (H_2O_2 30 % wt/wt in H_2O), methylene blue (MB, > 97%) and all solvents were purchased by Sigma Aldrich (Milan, Italy) and used without further purification.

4.2.2. Preparation of GO

GO was synthesized by a severe oxidation process of GNP taking inspiration from the Krishnamoorthy's modified Hummers method.[6] GNP (1 g) was stirred in 25 mL of a 96% H_2SO_4 solution for 30 minutes, keeping the temperature at 0 °C by an ice bath.[12] Then, 0.5, 1, 2 or 3% wt/wt equivalent of $KMnO_4$ were gradually added to the above solution, with the consequent formation of Mn_2O_7 that represents the actual oxidating species.[5,13]. During this operation, the temperature of the ice bath was allowed to increase up to room temperature. After that, the temperature was raised to 35 °C and the stirring was held for two more hours. The

resulting solution was diluted by gently adding 45 mL of water, under vigorous stirring. The temperature of the mixture raised instantaneously. During this step, the temperature of the water bath was allowed to increase up to 70 °C. This temperature was held for 15 minutes. 100 mL of H_2O_2 water solution (3% wt/wt) was further poured in the mixture to reduce the residual potassium permanganate and manganese oxide into manganese sulfate.[14] After one hour, the resulting suspension was centrifuged. The precipitate was collected and washed with 5% wt/wt HCl water solution under stirring. The suspension was centrifuged again and the precipitate was collected in 140 mL of distilled water. This last process was repeated until neutrality. Finally, the suspensions were diluted up to a final concentration of GO of about 4 mg/mL and sonicated with a Sonics Vibracell ultrasonic processor (500 W, 20 kHz) at 25% of amplitude, with a 50s/50s ON/OFF cycle, to improve the dispersion of GO nanosheets. The obtained suspensions were coded as GO1, GO2, GO3, GO4, where the number indicates the degree of oxidation obtained using increasing amounts of $KMnO_4$.

Cast GO samples (thickness about 8 μm) were obtained from water suspensions through an assembly process induced by the self-concentration of GO during water evaporation at the liquid/air interface.[15] In particular, samples were obtained by water casting at room temperature for at least 48h, followed by drying in vacuum oven at 90 °C overnight. Systems were coded as GO1-C, GO2-C, GO3-C, GO4-C.

4.2.3. Techniques

Energy Dispersive X-ray (EDX)

Energy Dispersive X-ray (EDX) analysis was performed using a FEI Quanta 200 FEG SEM equipped with an Oxford Inca Energy System 250 and an Inca-X-act LN2-free analytical silicon drift detector, on GNP and dried GO samples placed onto aluminum SEM stubs. The analysis was performed at 30 kV acceleration voltage. Average results and standard deviation values are based on three consecutive measurements on different areas of each sample.

Fourier transform infrared (FTIR) spectroscopy

Cast GO samples and pristine GNP were analyzed by means of Fourier transform infrared spectroscopy (FTIR) to evaluate the extent of the surface modification. By comparison, FTIR spectra were recorded on pristine GNP. Spectra were recorded with a Perkin Elmer Spectrum One FTIR spectrometer using a resolution of 4 cm^{-1} and 32 scan collections.

Confocal Raman spectroscopy

Confocal Raman spectra were acquired on cast GO samples and GNP by a Horiba-Jobin Yvon Aramis Raman spectrometer operating with a diode laser excitation source limiting at 532 nm and a grating with 1200 grooves/mm. The 180° back-scattered radiation was collected by an Olympus metallurgical objective (MPlan 50X, NA = 0.50) and with confocal and slit apertures both set to 400 mm. The radiation was focused onto a Peltier-cooled CCD detector (Synapse Mod. 354308) in the Raman-shift range 2000-1000 cm^{-1}. To separate the individual peaks in unresolved, multicomponent profiles, spectral deconvolution was performed using the software Grams/8.0AI, Thermo Scientific using a Voigt function line

shape. By a non-linear curve fitting of the data, height, area and position of the individual components were calculated.[16]

Dynamic Light Scattering (DLS)

The average size of GO sheets in water suspension was determined through Dynamic Light Scattering (DLS) analysis using a Zetasizer Nano ZS (Malvern Instruments). The analysis was performed at 25 °C at a scattering angle of 173°.

Wide angle X-ray diffraction (WAXD)

Wide-angle X-ray scattering analysis (WAXS) was carried out on cast GO samples by means of a Rigaku model III/D max generator equipped with a 2D imaging plate detector, using a Ni-filtered Cu Kα radiation (wavelength 1.5418 Å) at room temperature. To separate the individual peaks in unresolved WAXS profiles, spectral deconvolution was performed using the above mentioned software Grams/8.0AI, Thermo Scientific using a Lorentzian functions.

Thermogravimetric analysis (TGA)

Thermogravimetric analysis (TGA) of cast GO samples and GNP was carried out using a Mettler TGA/SDTA851 analyzer. All the samples were analyzed in nitrogen flux (30 mL/min) at 2 °C/min heating rate, from room temperature to 800 °C, using about 3 mg of material for each sample.

Differential Scanning Calorimeter (DSC)

Differential scanning calorimeter (DSC) experiments were carried out on cast GO samples using a TA Instruments DSC Q2000. The analyses were performed under nitrogen flux (30 mL/min) in dynamic mode at a 10 °C/min heating rate from 100 to 400 °C.

Scanning Electron Microscopy (SEM)

Scanning electron microscopy (SEM) of GNP and cast GO samples was performed by means of a FEI Quanta 200 FEG SEM in high vacuum mode. Before SEM observations, samples were mounted onto SEM stubs by means of carbon adhesive disks and sputter coated with a 15 nm thick Au-Pd layer. All the samples were observed at 10-30 kV acceleration voltage using a secondary electron detector.

Transmission Electron Microscopy (TEM)

Bright field Transmission Electron Microscopy (TEM) analysis of GO and GNP was performed on a FEI Tecnai G12 Spirit Twin (LaB6 source) at 120 kV acceleration voltage. TEM images were collected on a FEI Eagle 4k CCD camera. Before the analysis, water dispersed GO samples, diluted at about 1 mg/mL, were collected by immersing TEM copper grids in the suspensions. By comparison, GNP was also analysed after dispersion at about 1 mg/mL in N,N-dimethylformamide (DMF) and collection and drying onto TEM copper grids.

Specific surface area

Specific surface area (SSA) of GNP and cast GO samples was determined through N_2 adsorption analysis performed at liquid nitrogen temperature by means of a Micromeritics ASAP 2020 analyzer, using high purity gases (> 99.999 %). Prior to the analysis, all the samples were degassed at 150 °C under vacuum (P $<10^{-5}$ mbar) for 10 h. SSA was determined from the linear part of the Brunauer-Emmett-Teller (BET) equation.

SSA of graphene oxide in suspension (MB SSA) was measured through UV-vis spectroscopy with methylene blue (MB) dye as a probe. [17,18,19] GO1, GO2, GO3 and GO4 were diluted to 0.030 mg/mL in order to obtain a stable dispersion of graphene oxide in water, then an amount of MB equal to 1.5 times that required to cover the theoretical surface area of graphene oxide (2630 m^2/g) was added to the GO suspensions. After mixing for 24h at room temperature, a conjugate structure of GO and MB was formed, due to π-π interactions, and a precipitate was visible. The GO/MB mixture was centrifuged at 10000 rpm for 10 minutes by means of a Hermle Labortechnik Z 326 K centrifuge, to induce separation of the smaller sheets from the transparent solution. Then, the MB concentration of the supernatant solution was measured using a Jasco V570 UV spectrophotometer. A calibration curve was built to evaluate the MB concentration from the absorbance of the solution at 664 cm^{-1}, so the residual methylene blue in solution was found, and thus the adsorbed MB was calculated.

Considering the specific surface area of a MB molecule (2.54 m^2/g),[20] the adsorbed MB amount was correlated to the exposed area of the graphene oxide through the following equation:

$$SSA_{GO} = m_{MB}\, SSA_{MB}/m_{GO} \qquad (4.1)$$

where SSA_{GO} is the specific surface area of graphene oxide, SSA_{MB} is the area covered by 1 g of methylene blue, and m_{GO} and m_{MB} are respectively the mass of GO used in the experiment and the mass of MB adsorbed by graphene oxide.

4.3. Results and discussion

Quantitative analysis the GNP oxidation was carried out by EDX analysis, whose results are reported in Table 4.1. As concerning plain GNP, the oxygen/carbon atomic ratio was 0.06. This result showed that even in plain GNP there is a detectable level of oxidation, due to the production process. Increasing the oxidation degree of the realized GO samples, a monotonic increase of the O/C atomic was recorded, with a final value of 0.65 measured for the sample GO4, corresponding to a high oxidation level.[21]

The oxidation process of GNP was monitored by FTIR analysis. FTIR spectra in the range 800-200 cm^{-1} of GNP and cast GO samples are reported in Figure. 4.1a, showing the presence of convoluted bands in the range 1570-1620 cm^{-1} attributed to adsorbed water molecules and to C=C stretching vibrations of unoxidized graphitic domains.[22] The band at 1720-1740 cm^{-1}, whose relative intensity progressively increased with the oxidation degree, was assigned to C=O stretching vibrations of carboxyl edge groups.[23] Absorption bands attributed to C-O stretching vibrations and O-H deformations of carboxyl and hydroxyl groups are centered at 1040-1050 cm^{-1} and 1360-1370 cm^{-1}, respectively, whereas the presence of epoxy groups was evidenced by the typical band attributed to the stretching of C-O stretching, centered at 1220-1230 cm^{-1}.[24] As shown in Figure. 4.1a, the intensity of the adsorption band attributed to hydroxyl groups was relatively more intense at low oxidation degrees, whereas the adsorption band attributed to epoxies was significantly more intense the highly oxidized GO4-C sample. As concerning the carboxyl

groups, their bands slightly increased in intensity with the oxidation degree. These results indicated that the relative amount of the oxygen containing groups generated on graphene sheets changed with the conditions used for the oxidation process, with different species predominating at different oxidation degrees. In particular, OH groups seemed to be more relevant at low oxidation degrees, while epoxy groups prevailed at higher oxidation degrees, both these species mainly present on the basal plane of graphene oxide sheets.[25] On the contrary, carboxyl groups, generated at the edges of graphene oxide sheets, progressively increased with the dosage of $KMnO_4$.

Raman spectra of GNP and cast GO samples in the range 1000-1800 cm^{-1} are reported in Figure. 4.1b. In each spectrum a band centred at 1326-1343 cm^{-1} (D-band) and a complex band with components centred at 1555-1572 cm^{-1} (G-band) and 1595-1602 cm^{-1} (D'-band) were observed. The D-band is typical of disordered carbon in graphenes, and in particular to finite or nanosized graphitic planes, defects, vacancies, heptagon-pentagon pairs, kinks and heteroatoms. The G-band originates from the in-plane tangential stretching of carbon-carbon bonds in graphene sheets. Finally, the D' band, evidenced as a shoulder of the G-band at higher frequencies, is another feature induced by disorder and defects in the graphene structure. By spectral deconvolution, the intensity ratio I_D/I_G, a parameter indicating the degree of disorder in the graphene structure, was calculated and reported in Table 4.1. Results showed that more drastic oxidative conditions induced a progressive increase of I_D/I_G, even if a small inversion of the trend was observed for sample GO4, as already reported by Kadam et al.[26]

Through the analysis of the Raman spectra, the aromatic cluster size (L) in GNP and in each cast GO sample was calculated applying the empirical equation:[17,27]

$$L\ (nm) = 4\ A_G/A_D \qquad (4.2)$$

where A_G and A_D are the integrated intensities of G and D peaks, respectively.

As shown in Table 4.1, the average aromatic cluster size, related to the size of extended aromatic system left undamaged upon the oxidation process, monotonically decreased with the increase of $KMnO_4$ dose, from 11.8 to 2.0 nm.

Nevertheless, by DLS measurements, even if the oxidation process significantly reduced the aromatic cluster size, it did not affect the average size of the platelets, that remained almost unchanged with respect to those of GNP, irrespectively of the final oxidation extent of GO.

WAXS intensity profiles of GNP and cast GO samples are shown in Figure. 4.1c. Results are reported in Table 4.1. For GNP a sharp diffraction peak at $2\theta_1$ = 26.5° (interlayer distance of 0.336 nm) was observed, which corresponds to a compact stacked planar multilayered carbon structure.[17] Upon mild oxidation, i.e. in the case of GO1-C and GO2-C, this peak remained sharp and well resolved. However, a broadening effect was observed and quantified through spectral deconvolution. Its full width at half maximum (FWHM) increased from 0.51 (GNP) to 0.90 (GO2-C) due to the early distortion occurring of the AB stacking order of the graphite lattice generated by oxidation. For GO1-C and GO2-C, spectral deconvolution also indicated the presence of a second reflection at lower angles, $2\theta_2$ = 24.7-24.5°, corresponding to an increase of the interlayer distance, up to 0.363 nm. Nevertheless, for these samples, the extent of layer stacking almost unaffected by the oxidation was still high, as indicated by the intensity ratio between the reflection 2 and 1, lower than 0.3.

When higher oxidation levels were reached, GO3-C, a shift of the peak corresponding to the 002 reflection was recorded, associated to the evidence of a second reflection at lower angles. By deconvolution, the first peak, attributed to a more packed fraction of GO sheets, was centered at $2\theta_1$ = 24.4° with an increase of the corresponding d_1 spacing to 0.365 nm with respect to pristine GNP, while the second peak was centered at $2\theta_2$ = 20.9°

(d_2 = 0.425 nm). Moreover, for GO3-C, the distortion of the AB stacking order of the graphite lattice was very significant as well as the relative amount of less densely stacked GO sheets, as indicated by the high $FWHM_1$= 5.1, and by the I_2/I_1 ratio = 0.48, respectively.

Finally, at high oxidation degrees, sample GO4-C, an inversion of the intensities of the first and second reflection was observed, in this case the peak at lower angles being much more intense with respect to the broad reflection at higher 2θ values (I_2/I_1 = 2.41).[28] Reflection were centered at $2\theta_2$ = 12.7° and $2\theta_1$ = 23.3°. Therefore, most of the GO sheets for GO4-C were stacked with an average spacing d_2 = 0.697 nm, and a lower fraction with an average spacing d_1 = 0.382 nm. This abrupt change was the consequence of the heterogeneous nature of the oxidized graphene, constituted by graphitic sp^2 domains and by sp^3 domains typical of oxidized graphite.[6]

Table 4.1 Results of EDX, Raman and XRD analysis on GNP and cast GO samples at increasing oxidation degrees.

Sample		GNP	GO1-C	GO2-C	GO3-C	GO4-C
$KMnO_4$/GNP wt equivalent		-	0.5	1.0	2.0	3.0
O/C atomic ratio		0.06 ± 0.01	0.15 ± 0.03	0.24 ± 0.01	0.34 ± 0.03	0.65 ± 0.07
I_D/I_G		0.14	0.16	0.75	1.23	1.11
Average aromatic cluster size (nm)		11.8	11.3	2.8	2.6	2.0
WAXS	$2\theta_1$ (degrees)	26.5	26.6	26.4	24.4	23.3
	d_1 (nm)	0.336	0.335	0.338	0.365	0.382
	$FWHM_1$ (degrees)*	0.51	0.61	0.90	5.1	5.6
	D_1 (nm)**	31.7	26.5	17.9	3.2	2.9
	$2\theta_2$ (degrees)	-	24.7	24.5	20.9	12.7
	d_2 (nm)	-	0.360	0.363	0.425	0.697
	$FWHM_2$ (degrees)*	-	3.9	5.2	2.6	2.8
	D_2 (nm)**	-	4.1	3.1	6.1	5.9
	I_2/I_1***	0	0.10	0.28	0.48	2.41

* FWHM = full width at half maximum

** D_i = mean size of the of the stacked domains in the direction perpendicular to graphene planes, calculated from the reflection i (eq. 4.3)

*** Intensity ratio between WAXS reflection 1, centred at higher 2θ values, and reflection 2, centred at lower 2θ values.

The average size (D) of the stacked domains in the direction perpendicular to the graphene planes was calculated for cast GO samples at different oxidation degrees using the Debye-Scherrer equation:[29]

$$D = k\lambda/\beta \cos\theta \quad (4.3)$$

where k is a shape factor whose value can be approximated to 0.89, even if it varies with the shape of the crystallites, β is the FWHM in radians of the reflection, λ is the wavelength of the radiation used and θ is the Bragg angle of the reflection. As concerning the behavior of the reflection located at higher angles, the average domain size progressively decreased with increasing the oxidation degree, from about 32 nm for GNP, to a final D_1 value lower than 3 nm for GO4-C. Dividing these domain sizes by the calculated d_1 spacing for each sample, the average number of GO sheets can be obtained in each domains. In our case, this average number varied between about 94 GO sheets for GNP, to 79 (GO1-C), 53 (GO2-C), and finally 8.6 and 7.5 for GO3-C and GO4-C, respectively, thus demonstrating that stacking phenomena were progressively inhibited increasing the oxidation degree.In the case of low oxidized samples, a similar data analysis was not very significant for the low intense and high convoluted reflection at lower 2θ angles, due to uncertainty of the $FWHM_2$ values calculated by spectral deconvolution. Nevertheless, for the sample GO4-C, whose reflection centered at $2\theta_2$ angles was well separated by that centered at $2\theta_1$, the calculated average number of stacked GO sheets spaced by about 0.70 nm, was close to 8, this value being comparable to the value found for the more tight GO sheets evidenced by the reflection centered at $2\theta_1$. This finding indicated that the highly oxidized sample was constituted by two classes of stacked primary GO sheets, different for their average spacing (0.382 vs. 0.697 nm) and

their average dimension in the direction perpendicular to the GO planes (2.9 vs. 5.9 nm), but similar in the average number their constituting GO flakes.

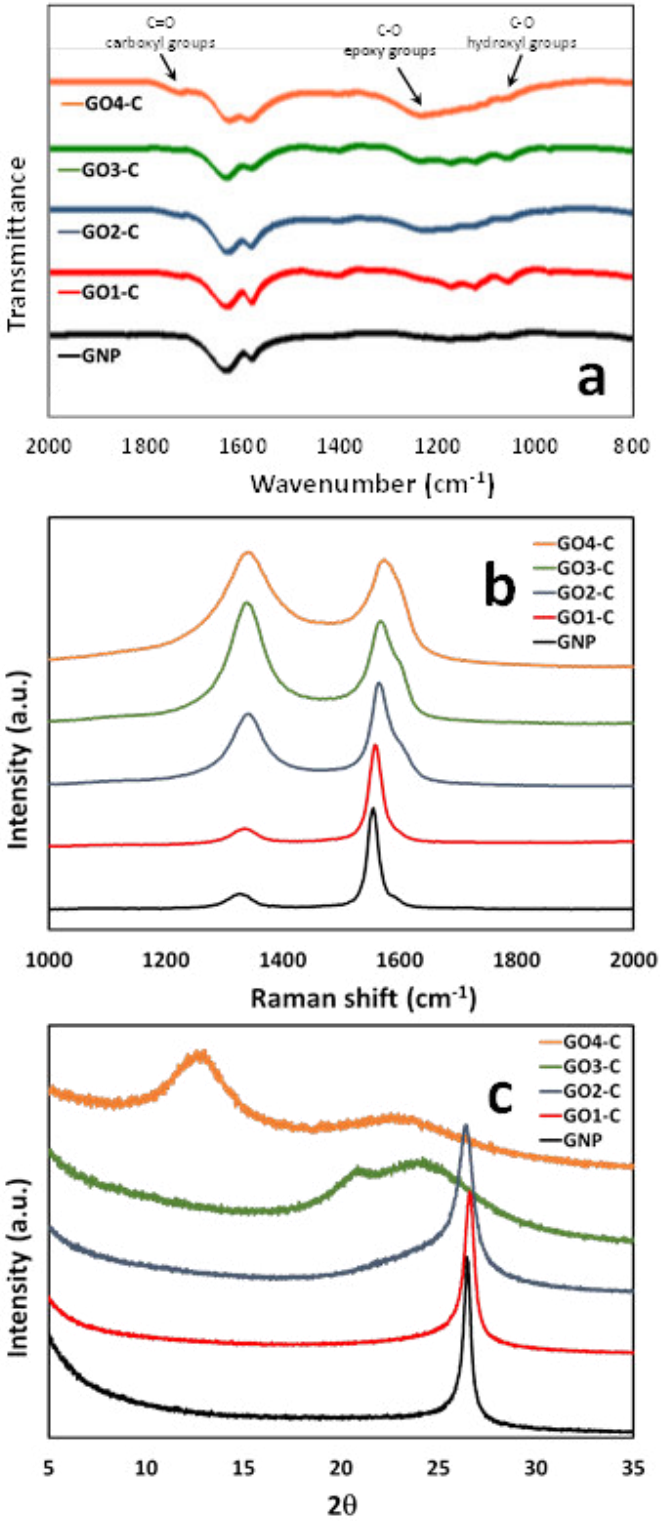

Figure 4.1 FTIR (a), Raman (b) and WAXS spectra (c) of GNP and cast GO samples.

GNP and cast GO samples with different oxidation degrees were also analysed by TGA in non-oxidative conditions, in order to evaluate their thermal stability. Results are reported in Table 4.2 and in Figure. 4.2a-b. At about 150 °C, a relevant mass loss occurred for all the samples, whose extent was directly correlated to their oxidation degree. The maximum rate of degradation occurred between 178 and 190 °C. For the sample GO4-C, the derivative TGA curve also showed, in addition to the main degradation peak, the presence of a shoulder at a higher temperature, as already reported by Kang et al.[30] for GO sample oxidized in comparable conditions. The residual percent weight at 300 °C decreased from 98 wt% for GNP to 85 wt% for GO3-C and to 69 wt% for GO4-C. For all the samples, the mass loss process was attributed to the thermally induced decomposition of labile oxygen-containing groups in GO,[18] producing the formation of carbon monoxide and dioxide, and water. Calorimetric analysis allowed associating this weight loss step in the range 150-300 °C to an exothermic process.

Table 4.2 Results of thermogravimetric and calorimetric analysis on GNP and cast GO samples at increasing oxidation degrees.

Sample	TGA	DSC	
	Residual weight % at 300° C	T_{exo} (°C)	ΔH_{exo} (J/g)
GNP	98	-	0
GO1-C	94	205	40
GO2-C	93	204	87
GO3-C	85	201	323
GO4-C	69	213	809

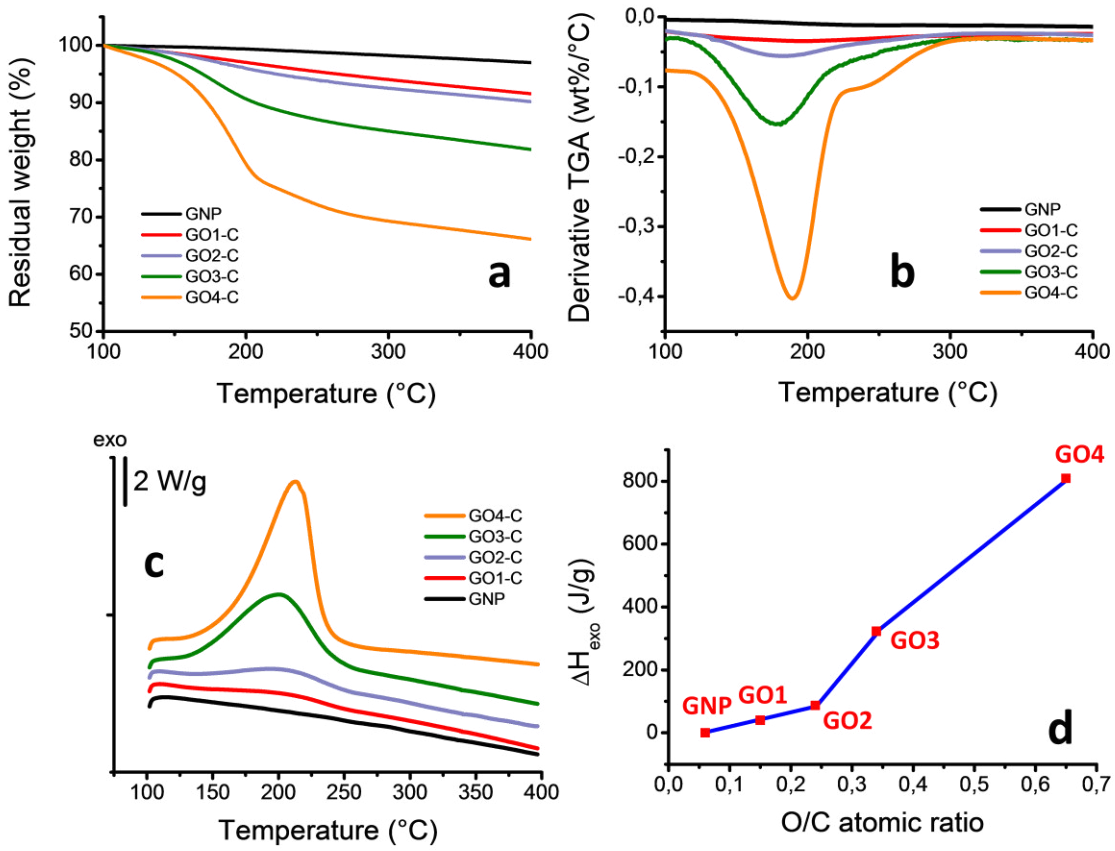

Figure 4.2 Results of thermogravimetric and calorimetric analysis on GNP and cast GO samples at increasing oxidation degrees: TG curves (a); derivative TG curves (b); DSC traces (c); enthalpy associated to the thermal decomposition process vs. oxygen/carbon atomic ratio of cast GO samples.

DSC curves of GNP and cast GO samples are reported in Figure. 4.2c. The maximum temperature and the enthalpy of the process are reported in Table 4.2. As shown, while the degree of oxidation did not significantly affect the temperature corresponding to the maximum of the exothermic peak, significant changes of the ΔH_{exo} were progressively recorded increasing the oxidation level of the GO samples up to GO2-C, followed by an even more abrupt change starting from GO3-C, up to 809 J/g for GO4-C. Plotting the obtained ΔH_{exo} vs. the oxygen content of GO cast samples, expressed as the O/C atomic ratio (see Figure. 4.2d), a change of the slope of the curve was clearly evidenced at medium oxidation levels. To explain

this behaviour, it can be considered the structure of GO sheets consisting of unoxidized polyaromatic areas alternate to oxidized clusters containing hydroxyl and epoxide groups and carboxyl groups located at the edges of the GO sheets,[25] and the results obtained by FTIR analysis, that demonstrated that the relative amount of these groups changed with the final oxidation degree of GO. Kang et al.,[30] demonstrated that the ratio among different functional groups, especially epoxies and hydroxyls, significantly affected the thermal stability of GO, Recently, Qiu et al.,[31] through theoretical calculations, showed that the decomposition of epoxide groups is significantly exothermic while the thermal decomposition of hydroxyl groups is isoenthalpic or only slightly endothermic. The thermal decomposition of carboxyl groups, instead, is exothermic, but less than the decomposition of epoxides. All these considerations are consistent with the results that we obtained by FTIR and DSC analysis, confirming that at low oxidation levels the predominant species are carboxyl groups and hydroxyl groups, and progressively increasing their content in GO, their thermal decomposition induced a slow increase of the associated ΔH_{exo}. Increasing the oxidation level, a higher concentration of epoxy groups were generated on graphene, thus making the decomposition of highly oxidized GO samples progressively much more exothermic, with a steeper increase of the associated enthalpy.

As detailed in the introduction of this chapter, in this work cast GO materials were obtained by self-concentration of GO during water evaporation at the liquid/air interface and the samples coded as GOX-C, where X indicate different oxidation degrees of GO in water dispersion, were obtained. For this process, it must be considered that GO suspensions are constituted by deprotonated graphene oxide sheets which create a dynamic network through their dipole-dipole interactions. When solvent

evaporation is promoted, GO nanoplatelets reaching the interface tend to aggregate and, once further nanoplatelets reach the upper layer are able to interact with the first layer through van der Waals forces. Therefore, GO tend to self-concentrate at the interface and GO sheets tend to stack, progressively forming a layer-by-layer cast film (steps C- I to C-IV of Figure 4.3).[32]

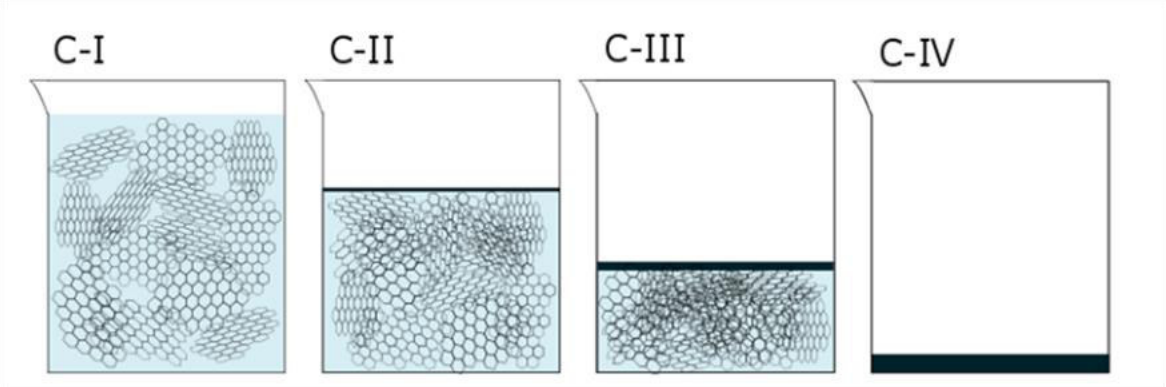

Figure 4.3 Representation of the drying steps involved in the GO casting.

Even if the mechanism of self-concentration and stacking of GO layers is widely accepted, a few papers concentrated the analysis of the effect of the oxidation degree of GO on the self-assembly, that is the key factor for the formation of GO cast films, also denoted as GO paper-like, papers or composite papers. Medhekar et al.,[9] through molecular dynamics simulations, elucidated the effect of the amount of oxygen containing groups on the interlayer mechanism of formation, structure and mechanical properties of GO papers. While the work was mainly focused on the water mediated interlayer interactions, they also mentioned the possible presence of intra-layer hydrogen bonds. Once again considering that GO sheets consist of unoxidized polyaromatic areas alternate to oxidized clusters

containing hydroxyl and epoxide groups, and ionizable carboxyl groups mainly located at the edge,[25] as the interaction amongst ionizable carboxyl edge groups is manly repulsive,[33] the formation of a self-standing membrane can mainly derive from intra-layer hydrogen bonds involving hydroxyl and epoxide groups. Therefore, the effect of different oxidation degree on the self-assembly process of GO is expected to be relevant.

Indeed, the realization of cast GO films from dispersions containing GO at different oxidation degrees confirmed this hypothesis. In Figure. 4.4 results of SEM analysis on GO-C samples are reported. Starting from GO1, GO2 or GO3-C it was not observed the formation of self-standing films. As shown in Figure. 4.4a, starting from the low oxidized GO2, the obtained samples was constituted by discontinuous GO islands with average size of hundreds of micrometers. The analysis of the surface of this sample at higher magnifications (Figure.4.4d) confirmed the low level of interaction amongst GO platelets. Very similar results were observed for GO1-C. At higher oxidation levels (GO3-C, see Figure. 4.4e) a more pronounced interaction between adjacent GO platelets was observed. Single GO sheets were not clearly identifiable and they were crumpled and well linked each other. Nevertheless, also in this case the investigation of the cast sample at low magnifications revealed the presence of discontinuous fragments of GO with average size of about 250-300 μm. Only further increasing the oxidation level to GO4, a large, self-standing and flexible GO film was obtained. The surface morphology of the GO4-C sample is shown in Figure. 4.4b and f. At low magnification, the continuity of the film and the absence of defects was clearly evidenced. At higher magnification the high level of interaction between GO sheets did not allow identifying their original contour and shape, all the sheets resulting

merged in a continuous and regular morphology. The cross-sectional structure of the film GO4-C is shown in Figure. 4.4g and h. The sample was characterized by a homogeneous thickness, approximately 8 μm, with the presence of almost parallel GO layers along the whole section.

A further insight on the mechanism of self-assembly of GO with different oxidation levels was obtained by TEM analysis, whose results are shown in Figure. 4.5. The occurrence of the formation of a self-standing film at the liquid air interface was confirmed by TEM image shown in Figure. 4.5a. By immersion of a non coated copper grid within the GO4 dispersion, after water evaporation a self-standing film with lateral dimension larger than 40 μm was observed amongst the mesh grids. At higher magnification, TEM analysis revealed the fine structure of the film, and it was possible to identify some of the constituting GO sheets. Selected area electron diffraction (SAED) showed that the film was composed by turbostratically stacked multilayer GO sheets, not oriented along preferential directions in the plane.[34] On the contrary, using uncoated TEM grids, it was not possible to collect self-standing films from GO1-3 dispersions. As shown in Figure. 4.5d for GO2, GO sheets were not able to give an effective self-assembling and after water evaporation they resulted partially isolated on the carbon support of the carbon-coated copper grid. Similar results were obtained for GO1 and GO3.

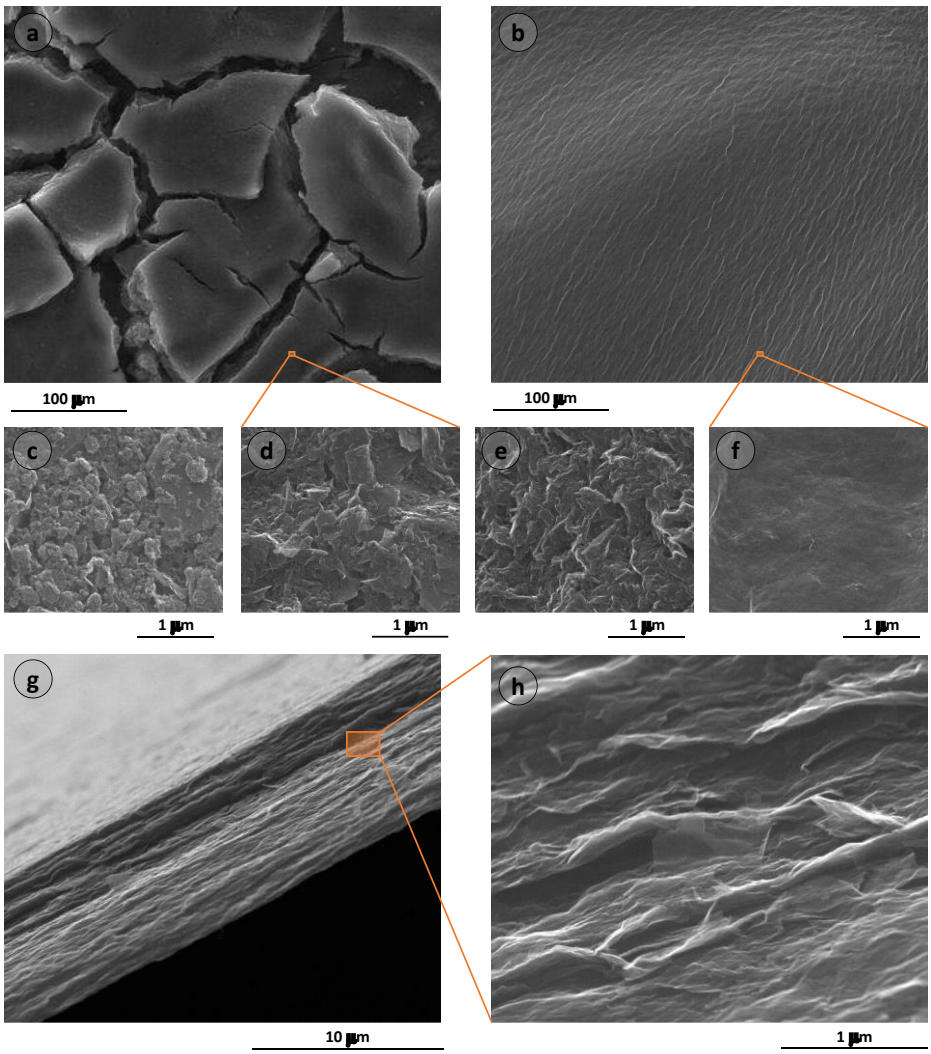

Figure 4.4 SEM micrographs of: upper surfaces of (a,d) GO2-C; (b,f) GO4-C; (c) GNP, (e) GO3-C, (g,h) cross-sections of GO4-C.

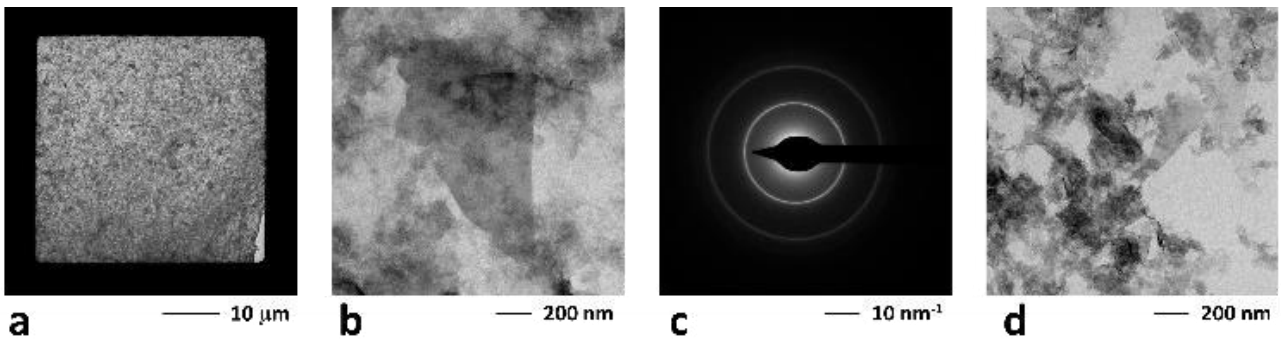

Figure 4.5 (a,b) TEM micrographs of a self-standing GO film on non-coated copper grid obtained from the water dispersion GO4; c) SAED of (b); d) TEM micrograph of GO sheets collected on a carbon-coated copper grid from the water dispersion GO2.

Several studies have been focused on the adsorption capacity in water dispersions of methylene blue (MB) by graphene oxide.[35],[36],[37],[38],[39] Since the first work of McAllister et al.,18 with slight change of the protocol, the adsorption of MB has been used to evaluate the SSA of graphene oxide ad its derivatives.[19,40,41]

The relationship between the oxidation degree of graphene oxide samples and their MB adsorption was already reported by Yan et al.,[11.] In this work, an exponential increase of the dye uptake was obtained with the increase the oxidation degree, attributed to the enhanced exfoliation of highly oxidized GO and to the presence of more active adsorption sites towards the dye. Nevertheless, the authors did not evaluate from the experimental MB uptake the SSA of the samples.

Instead, for our systems, using the MB dye as a probe, the specific surface area (MB SSA) of samples GO1-GO4 was determined on diluted water suspensions, by adding an excess of MB and determining the amount on non-adsorbed dye, as detailed in the experimental. Results are reported in Table 4.3.

Table 4.3 Specific surface area values calculated by methylene blue adsorption (MB SSA) on GO water suspensions and by N_2 adsorption at 77K (BET SSA) on cast GO samples

Oxidation degree	MB SSA (m^2/g)	BET SSA (m^2/g)
	GO suspensions	Cast GO
0 (GNP)		480 ± 5
1	1415 ± 19	346 ± 1
2	1401 ± 79	333 ± 1
3	1700 ± 83	195 ± 1
4	1760 ± 185	1.8 ± 0.1

Low oxidized GO samples, GO1 and GO2, showed MB SSA values close to 1400 m^2/g. Considering the theoretical specific surface area of graphene and graphene derivatives (2630 m^2/g) these results indicated that, even at low O/C atomic ratio, GO sheets were well dispersed and only limited stacking phenomena occurred in water suspensions. Moreover, by increasing the oxidation degree, the MB SSA monotonically increased, up to a significant value of 1760 m^2/g for GO4, showing that for this sample, in diluted conditions, only about 33% of the available GO area was masked by stacking and interactions occurring amongst GO sheets.

Results of the BET SSA of GNP and cast GO samples obtained by GO at different oxidation degree are reported in Figure 4.6 and Table 4.3.

Gas sorption properties of graphene and related materials, including graphene oxide, have been comprehensively discussed by Gadipelli and Guo.[10] By N_2 adsorption (77 K, 1 bar), BET SSA value up to about 900 m^2/g have been reported for thermally exfoliated GO,[42] even if most of the GO samples described in literature showed BET SSA values lower than 500 m^2/g.[10,43] The low BET SSA values observed for bulk GO samples with respect to the theoretical value of 2630 m^2/g, are generally explained considering that the bulk material shows large extent of stacking, assumed that the interlayer gallery spaces are inaccessible to the probe molecules used in surface area analysis.[44] In our case, starting from a BET SSA of 480 m^2/g, for commercial GNP, increasing the oxidation degree of GO, a progressive decrease of the BET SSA was observed, with an approximate 30% decrease of the surface area recorded for GO1-C and GO2-C and 60% decrease for GO3-C (see Table 4.3). Interestingly, a very low surface area was recorded for GO4-C, close to 2 m^2/g, demonstrating the relevance of stacking phenomena by self-assembly of highly oxidized GO at the liquid-air interface. Moreover, this result also indicated that, despite the wide interlayer spacing calculated by WAXS

analysis for GO4-C (about 0.70 nm), these interlayer galleries were inaccessible to the probe nitrogen molecule used in surface area analysis, also as a possible consequence of the high level of interactions amongst oxygen containing functional groups of adjacent graphene oxide sheets.

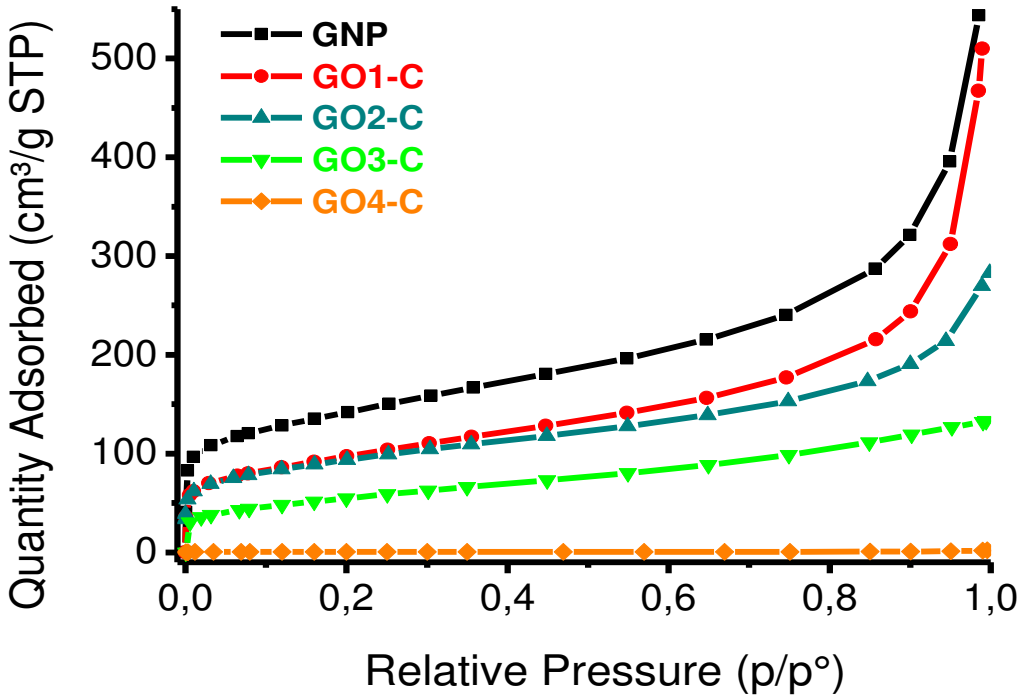

Figure 4.6 Nitrogen adsorption isotherms at 77K of GNP and cast GO samples.

4.4. Conclusions

This work presents an insight on the effect of the oxidation degree on the chemistry, the processability and the surface area of graphene oxide. GO samples were realized from graphite nanoplatelets by a modified Hummers method, using different dosage of $KMnO_4$. The effect of the $KMnO_4$/GNP ratio on the type and amount of oxygen-containing functional groups generated on the surface of graphene was investigated by FTIR and

Raman and Energy dispersive X-ray spectroscopy. Results indicated that the obtained GO samples were characterized by a very low to high level of oxidation. Raman and WAXS analysis allowed obtaining a deep characterization of the structure of GO samples, confirming that increasing the oxidation degree induced a progressive disruption of the graphitic crystalline order and an increase of the interlayer distance between graphene sheets. DLS measurements indicated that, even if the oxidation process significantly reduced the aromatic cluster size of GNP, it did not affect the average size of the platelets.

Thermal and thermogravimetric analysis were proven to be useful tools for the characterization of GO samples. The exothermal thermal decomposition of GO was significantly affected by the oxidation degree, and a non-linear dependence of the enthalpy of the process with type and amount of oxygen-containing functional groups was detected.

Cast GO samples were prepared by self-concentration of GO during water removal by evaporation at the liquid/air interface. SEM and TEM analysis on the obtained samples clearly revealed a dependence of the self-assembly ability of GO with the oxidation degree. Only at high oxidation levels large, defect-free, self-standing GO films were obtained, constituted by highly interacting graphene sheets showing also at high magnifications a continuous and regular morphology.

Specific surface area measurements carried out on GO in water dispersions by using methylene blue as a probe, revealed for low oxidized GO samples, MB SSA values close to 1400 m^2/g. indicating that, even at low O/C atomic ratio, GO sheets were well dispersed and only limited stacking phenomena occurred in water suspensions. This effect was more pronounced for highly oxidized GO, showing in this case that, in diluted conditions,

only about 33% of the available GO area was masked by stacking and interactions occurring amongst GO sheets.

BET specific surface area measurements carried out by nitrogen adsorption at 77 K also gave interesting information on the interaction occurring between graphene sheets at different levels of oxidation. In particular, a progressive decrease of the BET SSA was recorded on cast samples by increasing the oxidation level, with a final SSA of about 2 m^2/g recorded for the highly oxidized sample. This demonstrated the relevance of stacking phenomena by self-assembly of highly oxidized GO at the liquid-air interface.

The obtained results were used to select the best oxidation degree of GO for the surface modification and the embedding in the epoxy-elastomer matrix, described in the next chapter. In particular, GO at medium oxidation level (GO3) was used as starting material because it represented the best trade-off between the presence of suitable functional groups, needed for the surface modification, and the reduced tendency to self-agglomeration during processing.

4.5. References

1 A. K. Geim, K. S. Novoselov, Nat. Mater., 2007, **6**, 183.

2 A. C. Ferrari, F. Bonaccorso, V. Falko, K. S. Novoselov et al., *Nanoscale*, 2015, **7**, 4598.

3 D. Li, M. B. Muller, S. Gilje, R. B, Kaner, G. G. Wallace, *Nat. Nanotechnol.*, 2008, **3**, 101.

4 J.-J. Shao , W. Lv, Q.-H. Yang, *Adv. Mater.*, 2014, **26**, 5586.

5 D. R. Dreyer, S. Park, C. W. Bielawski, R. S. Ruoff, Chem. Soc. Rev., 2010, **39**, 228.

6 K. Krishnamoorthy, M. Veerapandian, K. Yun, S.-J. Kim, *Carbon*, 2013, **53**, 38.

7 X. Wang, Z. Xiong, Z. Liu, T. Zhang, *Adv. Mater.*, 2015, **27**, 1370.

8 Y. Ma, Y. Chen, *Natl. Sci. Rev.*, 2015, **2**, 40.

9 N. V. Medhekar, A. Ramasubramaniam, R. S. Ruoff, V. B. Shenoy, *ACS Nano*, 2010, *27*, 2300.

10 S. Gadipelli, Z. X. Guo, *Progr. Mater. Sci.*, 2015, **69**, 1.

11 H. Yan, X. Tao, Z. Yang, K. Li, H. Yang et al., *J. Hazard. Mater.*, 2014, **268**, 191.

12 A. M. Dimiev, J. M. Tour, *ACS Nano*, 2014, **8**, 3060.

13 **K. R. KOCH, P. F. KRAUSE*, J. CHEM. EDUC.*, 1982,** 59**, 973.**

14 W. S. Hummers Jr., R. E. Offeman, *J. Am. Chem. Soc.*, 1958, **80**, 1339.

15 J. J. Shao , W. Lv, Q. Guo , C. Zhang, Q. Xu , Q. H. Yang , F. Kang, *Chem. Comm.*, 2012, **48**, 3706.

16 V. Ambrogi, G. Gentile, C. Ducati, M. C. Oliva, C. Carfagna, *Polymer*, 2012, **53**, 291.

17 H. Yan, H. Wu, K. Li, Y. Wang, X. Tao, H. Yang, A. Li, R. Cheng, *ACS Appl. Mater. Interfaces*, 2015, **7**, 6690.

18 M. J. McAllister, J.-L. Li, D. H. Adamson, H. C. Schniepp, A. A. Abdala, J. Liu, O. M. Herrera-Alonso, D. L. Milius, R. Car, R. K. Prud'homme, I. A. Aksay, *Chem. Mater.*, 2007, **19**, 4396.

19 P. Montes-Navajas, N. G. Asenjo, R. Santamaría, R. Menéndez, A. Corma, H. García, *Langmuir*, 2013, **29**, 13443.

20 R. S. Rubino, E. S. Takeuchi. J. Power Sources, 1999, 81–82, 373.

21 M. Nováček, O. Jankovský, J. Luxa, D. Sedmidubský, M. Pumera, V. Fila, M. Lhotka, K. Klímová, S. Matějková, Z. Sofer, *J. Mater. Chem. A*, 2017, **5**, 2739.

22 Y. Wang, J. Liu, L. Liu, D. D. Sun, *Nanoscale Res. Lett.*, 2011, **6**, 241.

23 D. C. Marcano, D. V. Kosynkin, J. M. Berlin, A. Sinitskii, Z. Sun, A. Slesarev, L. B. Alemany, W. Lu, J. M. Tour, *ACS Nano*, 2010, **4**, 4886.

24 C. Xu, X. Shi, A. Ji, L. Shi, C. Zhou, Y. Cui, B. Xu, *PLoS One*, 2015; **10**, e0144842.

25 J. Kim, L. J. Cote, F. Kim, W. Yuan, K. R. Shull, J. Huang, *J. Am. Chem. Soc.*, 2010, **132**, 8180.

26 M. M. Kadam, O. R. Lokare, K. V. M. K. Kireeti, V. G. Gaikara, N. Jha, *RSC Adv.*, 2014, **4**, 62737.

27 F. Tuinstra, J. L. Koenig*, J. Chem. Phys.*, 1970, **53**, 1126.

28 H. K. Jeong, M. H. Jin, K. P. So, S. C. Lim, Y. H. Lee, *J. Phys. D: Appl. Phys.*, 2009, **42**, 065418.

29 L. Zhang, F. Zhang, X. Yang, G. Long, Y. Wu, T. Zhang, K. Leng, Y. Huang, Y. Ma, A. Yu, Y. Chen, *Sci. Rep.*, 2013, **3**, 1408.

30 J. H. Kang, T. Kim, J. Choi, J. Park, Y. S. Kim, M. S. Chang, H. Jung, K. T. Park, S. J. Yang, C. Rae Park, *Chem. Mater.*, 2016, **28**, 756.

31 Y. Qiu, F. Collin, R. H. Hurt, I. K. laotsa, *Carbon*, 2016, **96**, 20.

32 C. Chen, Q.-H. Yang, Y. Yang, W. Lv, Y. Wen, P.-X. Hou, M. Wang, H.-M. Cheng, *Adv. Mater.*, 2009, **21**, 3007.

33 F. Kim, L. J. Cote, J. Huang, *Adv. Mater.*, 2010, **22**, 1954.

34 L. Chen, J. Lei, F. Wang, G. Wang, H. Feng, *RSC Adv.*, 2015, **5**, 40148.

35 T. Liu, Y. Li, Q. Du, J. Sun, Y. Jiao, G. Yang, Z. Wang, Y. Xia, W. Zhang, K. Wang, H. Zhu, D. Wu, *Colloids Surf. B*, 2012, **90**, 197.

36 L. Chen, J. Yang, X. Zeng, L. Zhang, W. Yuan, *Mater. Express*, 2013, **3**, 281.

37 W. Zhang, C. Zhou, W. Zhou, A. Lei, Q. Zhang, Q. Wan, B. Zou, *Environ. Contam. Toxicol.*, 2011, **87**, 86.

38 S.-T. Yang, S. Chen, Y. Chang, A. Cao, Y. Liu, H. Wang, *J. Colloid Interface Sci.*, 2011, **359**, 24.

39 W. Peng, H. Li, Y. Liu, S. Son, *J. Mol. Liq.*, 2016, **221**, 82.

40 H. Zhang, X. Han, Z. Yang, J. Zou, *J. Nanomater. Mol. Nanotechnol.*, 2013, **S1**, 003.

41 Q. Wu, Y. Sun, H. Bai, G. Shi, *Phys. Chem. Chem. Phys.*, 2011, **21**, 11193.

42 K. S. Subrahmanyam, S. R. C. Vivekchand, A. Govindaraj, C. N. R. Rao, *J. Mater. Chem.*, 2008, **18**, 1517.

43 V. B. Parambhath, R. Nagar, K. Sethupathi, S. Ramaprabhu*, J. Phys. Chem. C*, 2011, **115**, 15679.

44 F. Guo, M. Creighton, Y. Chen, R. Hurt, I. Külaots, *Carbon*, 2014, **66**, 476.

CHAPTER 5

Graphene oxide/Epoxy Shape-Memory Liquid Crystalline Elastomer

5.1 Introduction

Shape memory polymers (SMPs) are responsive polymers that can fix a temporary shape after a deformation, and can recover original (permanent) shape in response to external stimuli, for instance temperature, pH, light, electric or magnetic field or solvents. The shape recovery may also occur through the contraction of oriented, extended chains of the material, triggered by a phase transition[1]. Liquid crystalline elastomers (LCEs) belong to this class of polymeric materials, as they are characterized by exceptional thermo-mechanical behavior that comes out thanks to the combination of the orientational order characteristic of the liquid crystalline phase, with the entropic elasticity of the polymer network[2]. Moreover, they show a spontaneous shape modification at the LC to isotropic state thermal transition. This results in a temperature-triggered strain recovery, upon the application of a fixed tensile stretching. Furthermore, the LCEs' thermo-mechanical properties are strictly related to the ability of the material to experience a reversible transition of the LC phase, from polydomain to monodomain, under tensile stress. This transition is due to the parallel alignment of the mesogens with the stress axis. All these features make liquid crystalline elastomers suitable for applications in which reversible thermoactuation is needed.

A potential strategy to tailor responsiveness of LCEs is represented by the incorporation of functional conjugated compounds or inorganic and carbonaceous particles[3]. For example, the incorporation of CNT into LCE can promote a faster and more efficient response over the thermal actuation, improving thermal conductivity of polymeric LCE and thus inducing a quick delivery of heat to all mesogens[4]. Moreover, the mutual alignment between either low-molecular-weight or polymer liquid crystals and CNT has been proven[5]. In a previous paper [6] a series shape memory nanocomposites have been developed

incorporating surface-modified multiwalled carbon nanotubes at different loading levels into a LC elastomer. It was shown that the approach used affords a large degree of tuning of thermomechanical response, allowing the design of new shape-memory materials for target applications.

In the present work, functionalized graphene oxide was employed for the realization of liquid crystalline shape memory nanocomposites. Recently, graphene oxide has been used in numerous polymer applications in both scientific and technological areas. The spread of graphene oxide is due to its unique thermal, electronic, mechanical and optical features as well as to its excellent biocompatibility[7]. Moreover, GO is suitable for fabricating polymer nanocomposites[8,9,10], as it is rich of oxygen-containing groups, which effectively weaken the van der Waals forces among the graphitic sheets and facilitate GO dispersion in both solvents and polymer matrices. As a further advantage, GO is obtained through facile chemical exfoliation of graphite and graphene nanoplatelets. In this respect, GO can be thus a desirable reinforcing filler to enhance the intrinsic properties of pristine polymers. In the recent years, a number of papers have been published dealing with the use of graphene oxide in shape memory polymer systems[11,12,13]. Among them, papers describing epoxy-based shape memory materials are also reported, in which reduced graphene oxide is used to enhance electro-responsive behavior of SM epoxies[14,15].

Another significant feature of GO relies on its liquid crystallinity in aqueous dispersions. The LC phase behaviour can be maintained by including an additional polymer component in the solvent medium[16]. Furthermore, it has been demonstrated that the orientation of graphene oxide liquid crystals could be manipulated by a magnetic field or mechanical deformation, offering a worthwhile approach for the realization of high-performance nanocomposites, optical and energy-storage materials, and other numerous advanced applications[17].

Starting from these considerations, this research has been focused on the realization and characterization of polymer nanocomposites based on epoxy elastomers filled with graphene oxide. The objective was to investigate the effect of the nanofiller on the structure and properties of the LCE, with particular concern on the shape memory effect. For this purpose, a mesogenic epoxy monomer, namely p-bis(2,3-epoxypropoxy)-α-methylstilbene (DOMS), was selected as diepoxy monomer. The use of DOMS was based on its ability to impart, in combination with a suitable co-monomer, liquid crystalline properties to the cured resin. DOMS was synthesized according to a procedure previously set up[18]. Sebacic acid (SA) was selected as a co-monomer, as it is able to give elastomeric and shape memory properties. The effect of varying amounts of GO on LC elastomers was then studied.

In order to obtain high performance nanocomposites, the achievement of homogeneous distribution and dispersion of the nanofillers within the polymer matrix was required. Hence, the first objective of the work here presented is the set up of an effective compatibilization strategy based on the surface modification of GO, able to improve the interfacial adhesion with the matrix. Once the compatibilization strategy was optimized, the preparation and characterization of the liquid crystalline elastomeric nanocomposites has been carried out.

5.2 Experimental

5.2.1 Materials

p-bis(2,3-epoxypropoxy)-α-methylstilbene (DOMS) was prepared according to the synthetic procedure described in a previous work[19] (melting point = 126.2 °C; nematic-to-isotropic transition temperature ($T_{n\rightarrow i}$) = 89.6 °C, monotropic; Yield = 47.5%.

Sebacic acid (SA, melting point 133-137°C), purity > 99%, was obtained from Sigma-Aldrich and used as received. Tricaprylammonium chloride (TCAC) was used as catalyst. Structural formulas of DOMS and SA, along with the scheme of reaction leading to the LCE, are reported in Scheme 5.1.

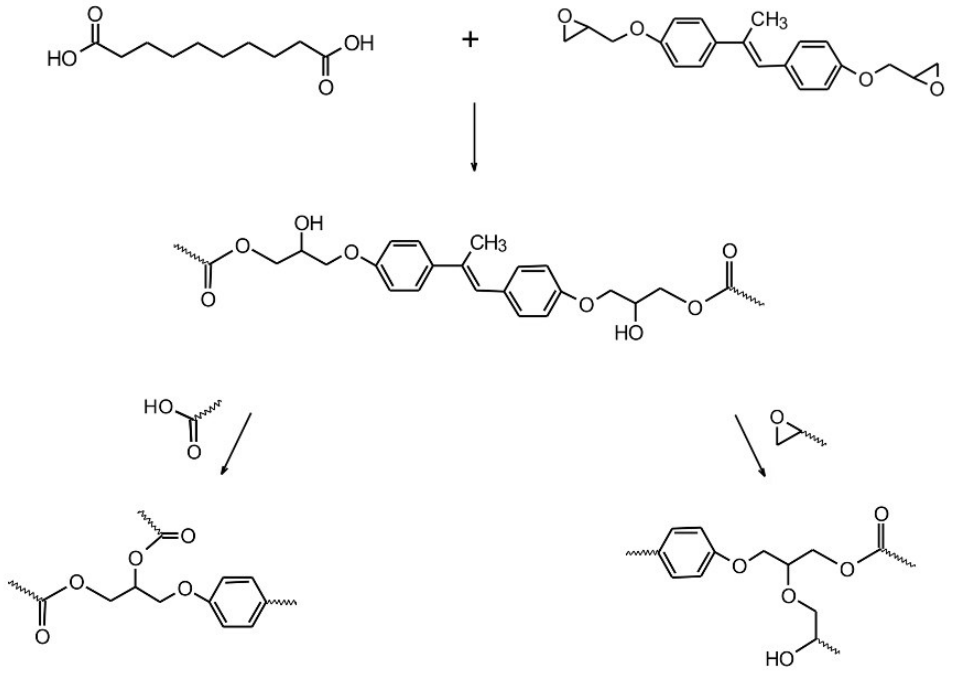

Scheme 5.1. Structural formulas of DOMS and SA, and reaction scheme involved in the formation of the LC elastomer network.

Graphite Nanoplatelets (GNP) with average surface area of 300 m^2/g and bulk density of 0.2-0.4 g/cm^3 were purchased from XG Sciences. GO was synthesized starting from GNP, as detailed in Section 2.3.

Sulphuric acid, H_2SO_4, potassium permanganate, $KMnO_4$, 30% v/v hydrogen peroxide water solution and hydrochloric acid 37 v/v were purchased from Sigma-Aldrich and used as received.

5.2.2 Preparation of epoxy functionalized adducts

The functionalization of GNP with epoxy-based groups was carried out in a two-step procedure including the oxidation of GNP and the subsequent reaction of water-dispersed GO with DOMS.

GO was synthesized using the harsh oxidation of graphite according to the modified Hummers method of Krishnamoorthy et al.[20] by employing $KMnO_4$ and concentrated H_2SO_4, followed by sonication. GNP (0.53 g) were stirred in 98% H_2SO_4 (15 mL) for 30 minutes. The required amount of KMnO4 was gradually added to the above solution while keeping the temperature below 20 °C. The mixture was then stirred at 35 °C for 2 h. The resulting suspension was diluted by adding slowly 25 mL of water under vigorous stirring, and further treated by adding 30% H_2O_2 solution (5mL) and 45 mL of distilled water. The resulting graphite oxide suspension was repeatedly washed and centrifuged, first with 5% HCl aqueous solution and then with distilled water until the pH of the solution became neutral. Finally, this solution was sonicated for 1 h (30sec pulse on and 30sec pulse off), obtaining the exfoliation of the graphitic oxide into a few-layer GO.

Epoxy functionalized GO adducts were prepared as described below. First, the concentration of GO in water dispersion was calculated: a known volume of the dispersion was weighed and then placed on a hot stage to allow water evaporation. As soon as it got dry, GO was weighed and the concentration of solution was calculated. The required amount of GO water dispersion, corresponding to a theoretical 0.75 wt.% percentage of GO in the composite, was added to molten DOMS at 165 °C dropwise, in order to guarantee the complete evaporation of water. Subsequently, the catalyst (TCAC, 2 mol.% with respect to epoxy content) was added, and the resulting mixture was sonicated for 2 hours with a 10 sec ON/ 50 sec OFF pulse cycle, and an amplitude of 25% while it was under magnetic stirring. The obtained adduct was recovered using dioxane and centrifuged at 10000 rpm for 10 min with a brake time of 4 min. The precipitated was isolated from the solution

containing epoxy excess, washed and centrifuged again with dioxane; this step was repeated 4 times. The remaining adduct was then dried and analysed.

5.2.3 Preparation of neat DOMS-SA resin

Neat DOMS-SA resin was obtained by adding a stoichiometric amount of SA to molten DOMS (molar ratio 1:1 with respect to DOMS). Once SA melted, the catalyst (TCAC, 2 mol.% with respect to the amount of epoxy groups) was added, and the mixture was kept under stirring for 2 minutes, then poured into a previously heated Teflon-coated glass mold and cured in an oven at 180 °C for 2 hours. The obtained sample was coded as DS_Neat.

5.2.4 Preparation of nanocomposites

Epoxy-based nanocomposites were obtained by a two-step procedure, involving first the dispersion of GO in the molten organic phase and subsequently the curing reaction between the epoxy monomer and the sebacic acid, as detailed in the following.

DOMS was melted and the appropriate amount of GO water solution was slowly added, in order to obtain a 0.15 wt.% GO nanocomposite. Then the catalyst (TCAC, 2 mol.%) was added. Sonication at 165 °C for 120 minutes alternating ON/OFF cycles lasting 10 and 50 seconds, respectively, with an amplitude of 25%, was performed. Subsequently, SA (molar ratio 1:1 with respect to DOMS) was added. Once it was melted, a further amount of catalyst (TCAC, 2 mol.%) was added. The obtained mixture was sonicated at 165 °C for further 120 sec. The resulting material was poured into a previously heated Teflon-coated glass mold and cured in oven at 180 °C for 2 hours. The same procedure was used to prepare the composite containing 0.45 wt.% of GO. The samples were coded as DS_GO_15 and DS_GO_45, respectively.

5.2.5 Techniques

Fourier transform infrared (FTIR) spectroscopy

FTIR analysis was performed on DOMS, GNP, GO and on the epoxy-functionalized GO-DOMS. FTIR spectra were obtained through the attenuated total reflectance (ATR-FTIR) method using a PerkinElmer Spectrum One FTIR equipped with a universal ATR sampling accessory (Wellesley, MA, USA). Spectra were collected using a resolution of 4 cm^{-1} and 16 scan collections.

Thermogravimetric analysis (TGA)

TGA was carried out using a Perkin Elmer Pyris Diamond thermogravimetric analyser (Wellesley,MA, USA). DOMS, GNP, GO, GO-DOMS adduct and DOMS-GO mixture were analyzed in air flux (100 mL/min) at 2 °C/min heating rate using about 3 mg of material for each sample. All graphene-based samples were analyzed with a procedure including a preliminary isothermal step for 120 min at 120 °C in air flux in order to remove absorbed moisture and residual solvent.

Transmission Electron Microscopy (TEM)

TEM analysis was performed on a FEI TECNAI G12 Spirit-Twin (120 kV, LaB6) microscope equipped with a FEI Eagle 4K CCD camera (Eindhoven, The Netherlands).

Differential Scanning Calorimeter (DSC)

A TA Instrument DSC Q2000, equipped with a Refrigerator Cooling System (RCS) accessory, was used to monitor the phase and glass transitions temperatures of cured

samples. DS_Neat, DS_GO_15, and DS_GO_45. Tests were performed in dynamic mode according to the following temperature treatment: heating from -40 to 150 °C at 10 °C/min heating rates; cooling from 150 to -20 °C at 10 °C/min; heating from -20 to 200 °C at 10°C/min. Nitrogen was used as purge gas.

Scanning Electron Microscopy (SEM)

SEM analysis was performed using a FEI Quanta 200 FEG (Eindhoven, The Netherlands) in high vacuum mode, using a secondary electron detector and an accelerating voltage ranging between 15 and 20 kV. For the analysis, cryogenically fractured specimens were obtained from the sample coded DS_GO_45. Before the analysis, samples were coated with a gold-palladium layer (about 15 nm thick) by means of a Emitech K575X sputter coater. EDS/SEM measurements were also performed.

Wide angle X-ray diffraction (WAXD)

XRD measurements were made using a Bruker-AXS D8-Discover diffractometer equipped with parallel incident beam (Göbel mirror), vertical θ-θ goniometer, XYZ motorized stage and with a GADDS (General Area Diffraction System). Samples were placed directly on the sample holder for transmission analysis. An X-ray collimator system close-to-the-sample allows analyzing areas of 500 µm. The X-ray diffractometer was operated at 40 kV and 40 mA to generate Cukα radiation. The GADDS detector was a HI-STAR (multiwire proportional counter of 30x30 cm with a 1024x1024 pixel) placed at 15cm from the sample. The X-ray beam hit the sample at 0.0º of incidence. The collected frame (2D XRD pattern) covers at such distance a range from 2.0 up to 35.0º 2θ. The direct X-ray beam is stopped by a beam stop placed directly at the end of the collimator after the sample.

The exposition time was of 600s per frame. The resulting images were gamma integrated to obtain a conventional 2θ diffractogram.

Thermomechanical analysis (TMA)

Thermomechanical analysis was performed using a Perkin Elmer Pyris Diamond DMA Dynamic Mechanical Analyzer equipped with a Cooling Controller, under nitrogen flux. A static tensile load of 45 kPa was applied and temperature was cyclically varied between 20 and 110 °C at a fixed rate of 2°C/min in order to monitor the shape-memory behavior effect of all samples.

5.3 Results and discussion

5.3.1 Epoxy-functionalized GO adducts

GO functionalization was carried out according to the procedure described in the Experimental Part. The GO epoxy adducts were purified by means of repeated washing and centrifugation cycles using dioxane and then analyzed through TGA, FT-IR and TEM analysis, as displayed in Figure 5.1.

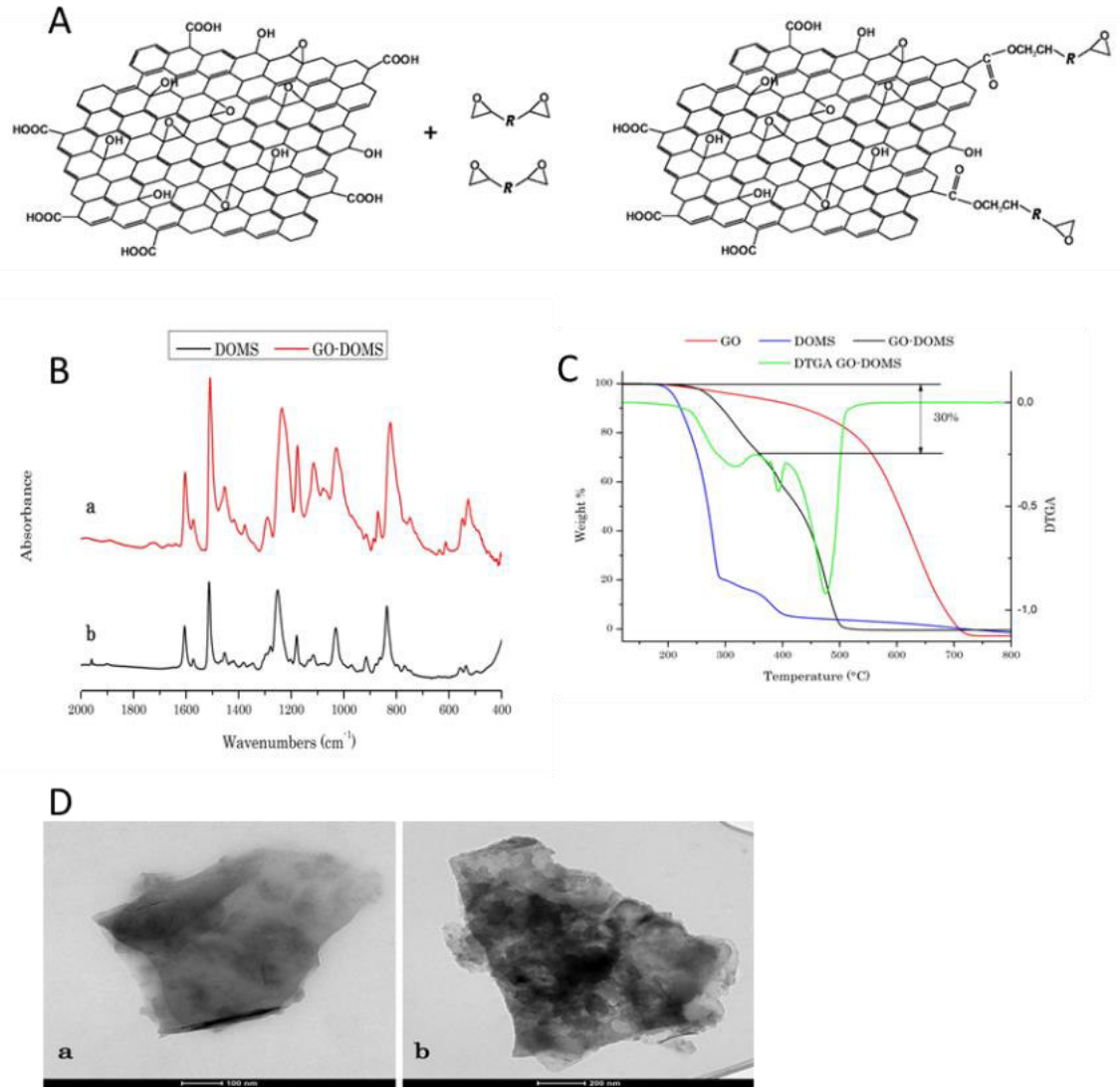

Figure 5.1 (A) Reaction scheme between epoxy groups of DOMS and carboxyl groups of GO; (B) spectra of neat DOMS (a) and GO-DOMS (b); (C) TGA curves of neat DOMS, GO, GO-DOMS and DTGA curve of GO-DOMS; (D) TEM images of GO (a) and GO-DOMS adduct (b).

In Figure 5.1A the reaction mechanism between DOMS and GO is sketched. The achievement of GO functionalization with DOMS monomer (GO-DOMS) was verified through the analytical characterization of the adduct purified through repeated dioxane washing and centrifugation cycles. The occurred grafting of DOMS on the GO surface was confirmed by FTIR analysis. FTIR spectra of neat DOMS and GO-DOMS adduct are reported in Figure 5.1B. The presence in the GO-DOMS spectrum of all the peaks typically associated

to DOMS is indicative of the successful formation of the epoxy-functionalized graphene oxide. In order to obtain the quantitative evaluation of the amount of epoxy grafted onto GO, TGA analysis was performed on dried GO and the GO-DOMS adduct under air. The heating rate was set as 2 °C/min in order to separate the different degradation processes. In Figure 5.1C, TGA traces of GO, DOMS and GO-DOMS are reported along with the derivative TGA trace of GO-DOMS sample. None of the sample exhibited any significant degradation phenomena for temperatures lower than 200 °C. At higher temperatures, they showed a different thermo-oxidative behavior. DOMS underwent the thermo-oxidative degradation through a 2-step mechanism, the first step occurring in the range 200-300 °C, and the second one in the range 300-400 °C. The TGA trace of GO showed a slow weight loss between 300 and 500 °C, then a rapid degradation in the range 500-700 °C. As concerning GO-DOMS, it exhibited a weight loss step in the range between 250-400 °C related to the degradation of the DOMS fraction grafted on GO that was not removed after purification. It was found that about 30 wt.% of DOMS was covalently bound to the GO surface. Subsequently, a second step related to the degradation of GO fraction present in the adduct occurred, leading to a complete volatilization at 500 °C. This result highlights that the functionalized GO is less stable than the parent GO. It can be hypothesized that the functionalization process of GO with DOMS, may shift the degradation of the GO fraction to lower temperatures. TEM images of GO and GO-DOMS adduct are reported in Figure 5.1D. From a comparison of the images, it is evident that the surface of GO sheets is distinctly covered by an organic layer (Fig. 1D-b), confirming the homogenous grafting of DOMS on the particle surface.

5.3.2 Preparation and characterization of nanocomposites

As detailed in the experimental part, epoxy-based nanocomposites were obtained by a two-step procedure. In order to obtain macroscopically homogeneous materials, the crosslinking reaction was performed starting from the GO-DOMS adducts. First, the fillers were dispersed in the molten monomers, sonicated, and then, after the addition of the curing agent, the obtained mixtures were poured in Teflon-coated glass molds and cured in oven at 180 °C for 2 h. Well-dispersed nanocomposites with 0.15 and 0.45wt.% of carbonaceous fillers were obtained. As an example, Figure 5.2 shows SEM micrographs of DS_GO_45. As evidenced in the figure, GO platelets were uniformly dispersed within the matrix, and a good adhesion between matrix and filler was achieved.

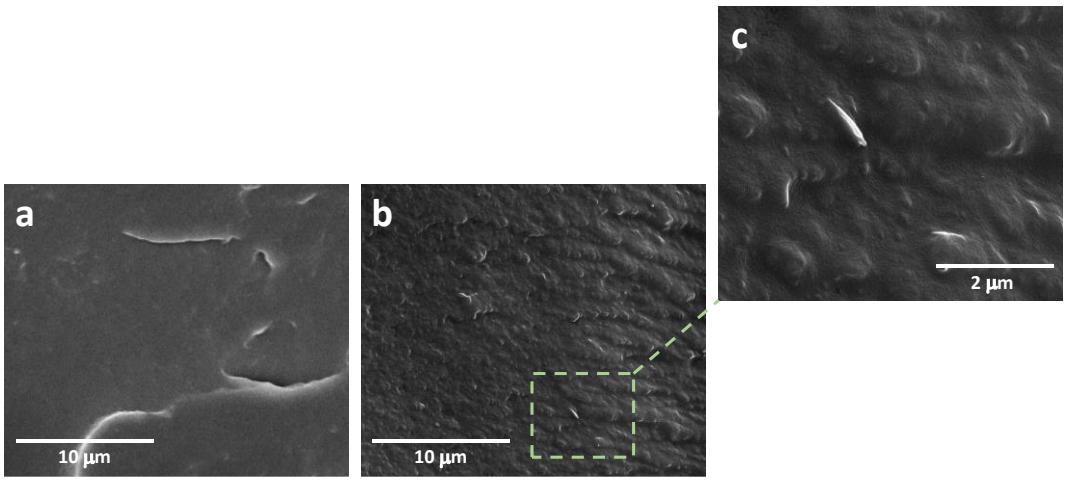

Figure 5.2 SEM images of fractured surfaces of (a) DS_NEAT, and (b and c) DS_GO_45.

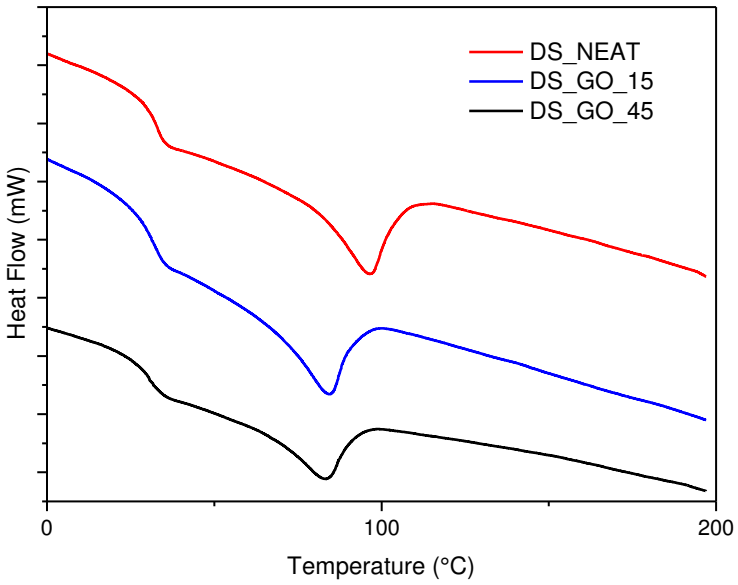

Figure 5.3. DSC traces (II heating scan) of DS_Neat, DS_GO_15, and DS_GO_45.

Figure 5.3 shows the DSC traces of all LCE samples. Table 5.1 reports the values of glass transition temperatures (T_g), as well as the temperatures (T_i) and enthalpies (ΔH_i) associated to the isotropization of the LC elastomers.

Table 5.1 DSC and DMA characterization of the elastomers-based nanocomposites.

Sample	DSC			DMA				
	T_g [°C]	T_i [°C]	ΔHi [J g^{-1}]	T_g [°C]	T_i [°C]	E'(0°C) [GPa]	E'(80°C) [MPa]	E'(120°C) [MPa]
DS_Neat	33.0	96.6	14.5	38.4	67.3	1.43	16.1	1.74
DS_GO_15	31.4	84.4	12.3	36.9	68.3	0.155	6.32	1.45
DS_GO_45	30.4	83.3	11.7	36.8	63.5	2.20	5.12	1.77

Compared to the neat matrix, GO-filled nanocomposites showed a slight decrease of Tg, Ti and ΔHi values associated to the smectic-to-isotropic transition. Isotropization enthalpies were in the range of 11−15 J g^{-1}, comparable with values recorded for isotropization of smectic-A systems [21]. The observed trend of Ti and ΔHi suggested that the presence of GO increased the polymer free volume, affecting the LC phase stability[22,23,24]. In general, for LC polymers, the thermal stability of the liquid crystalline phase is closely related to the morphology of the LC domains formed, with smaller LC domains exhibiting lower isotropization temperatures. In the case of DS_GO_15 and DS_GO_45, the addition of GO likely induced a slight, not significant variation of the smectic structure. This is evidenced also by wide-angle X-ray diffraction patterns reported in Figure 5.4.

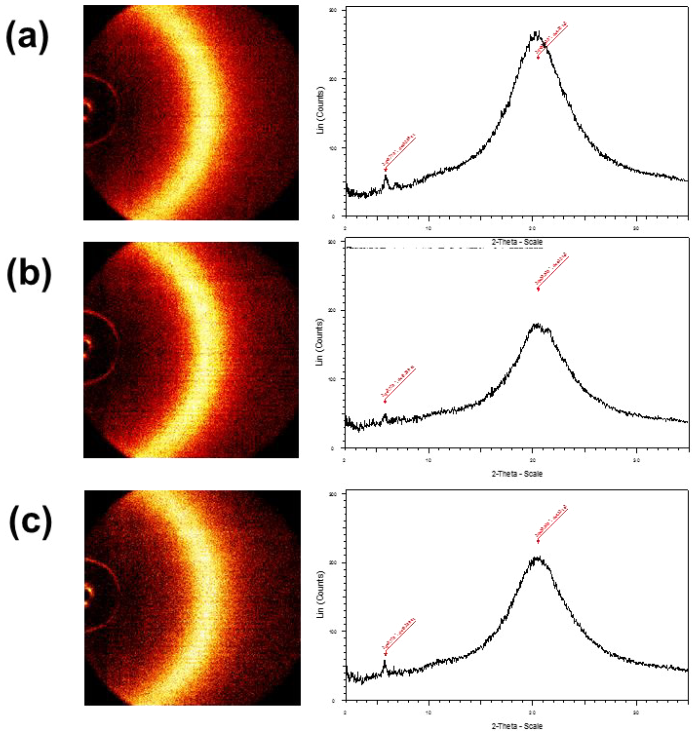

Figure 5.4 WAXD diffraction patterns (left) and the corresponding intensity integrations along the meridian axis (right) of unstretched (a) DS_Neat, (b) DS_GO_15, and (c) DS_GO_45

WAXD diffraction patterns of all the investigated samples showed a weak reflection at 2θ = 5.78° corresponding to a $d_{spacing}$ of about 15.3 Å, comparable with the length of 15.1 Å calculated for DOMS-based mesogen [21]. Therefore, the morphological analysis confirmed DSC data, as the obtained spectra were almost identical for the three samples, suggesting a negligible influence of GO on the LC phase behavior. Most probably GO flakes were able to align to the smectic planes without significantly disturbing the layered structure of the elastomeric matrix. As reported in literature, sheets of GO were found to exhibit liquid crystallinity in both aqueous and organic media, and thus are potentially able to induce higher order structures to a polymer composite[25,26].

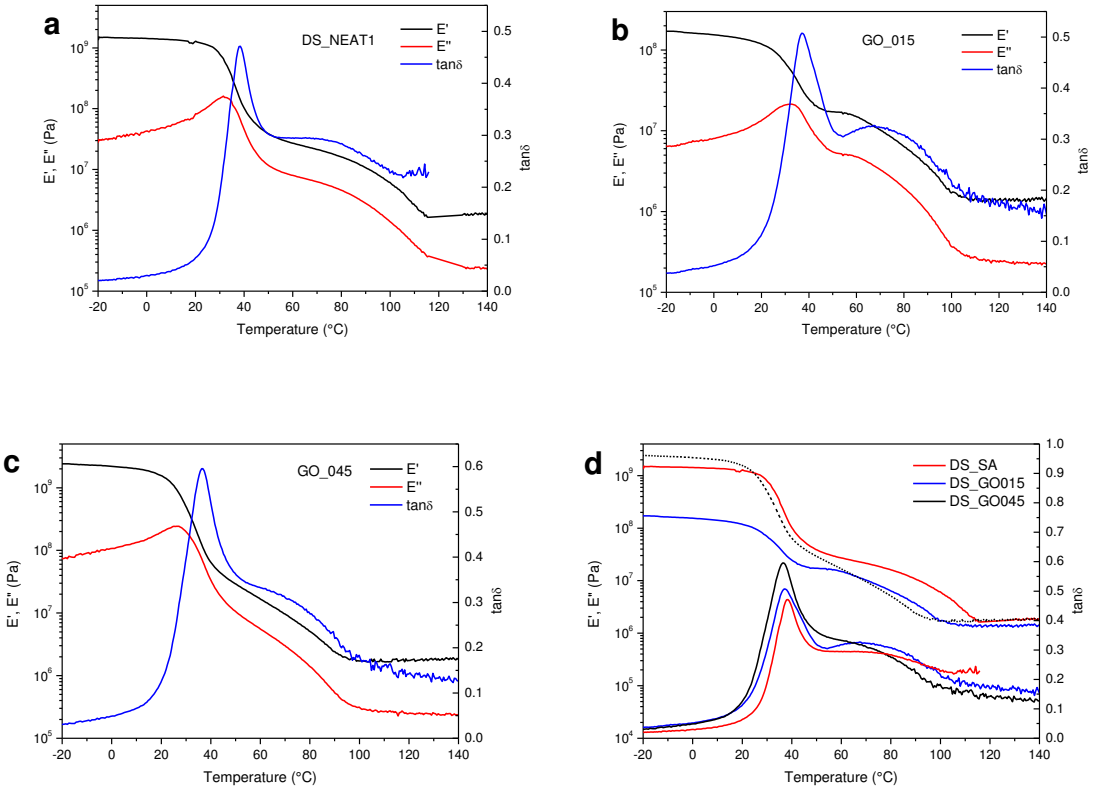

Figure 5.5. DMA curves of (a) DS_Neat, (b) DS_GO_15, and (c) DS_GO_45. (d) Comparison of E' and tand curves of all samples.

Figure 5.5a-c shows storage and loss moduli (E’ and E’’), and dissipation factor (tanδ) of the LCE as determined by dynamic mechanical analysis (DMA). In all cases, E’ values were larger than E’’ over the temperature range explored, demonstrating that, irrespective of the presence of filler, the elastic component was prevailing over the viscous one due to the crosslinked structure of the elastomers. Two thermal relaxations (see also Table 5.1) were observed, corresponding to glass transition and isotropization. In particular, as noticed from the tan curves, glass transition had a greater impact on the elastomer viscoelastic properties compared to isotropization. In Figure 5d, E’ and tan curves of all samples are compared. From the curve (and the values in Table 1), the influence of GO as determined by DSC was confirmed by DMA. In particular, a decrease by 1.5 °C in glass transition temperature was noted for DS_GO_15 and DS_GO_45. As regards T_i, the calculation of the peak value from the tanδ curve was not trivial, therefore the experimental curve was deconvoluted through peak fitting, and the values related to the maximum of the fitting curve are listed in Table 5.1. It is noticed that T_i values from DMA are significantly lower than those detected by DSC. It is likely that the mechanical relaxation due to T_g is able to trigger the molecular motions which eventually lead to isotropization. From the values calculated, it seems that a higher content of filler results in a destabilization of the LC phase, as suggested by the lower T_i value. Rather unexpectedly, there was no definite trend in storage moduli in the glassy region (T = 0 °C) with the content of MWCNT (Table 5.1). A high content (0.45wt %) of GO resulted in a larger value of E’ due to the stiffening effect of the rigid filler. However, when only 0.15 wt% GO was included in the composite, a significant drop of E’ was noticed. This result suggests that in presence of low amounts of GO, inter-chain attractive forces or chain flexibility are affected, owing to the interaction between polymer chains and GO platelets. Increasing the content of GO may lead to particle agglomeration, causing a stiffening of the material due to the introduction of rigid

filler particles. It is also worth noticing that the value of E' in the rubbery region was affected by the presence of GO. In particular, as detailed in Table 5.1, above the isotropization temperature (80 °C), DS_Neat showed a value of E' (about 16 MPa) significantly higher than that of DS_GO_15 and DS_GO_45 (about 6 MPa). This outcome indicates that the carbon filler may reduce the network rigidity also in the rubbery state. In this regard, no significant effect due to the amount of GO was observed. This behavior was similar to that reported for DOMS_SA-based MWCNT composites, where only high CNT contents (3.0 wt%) caused the rigidity of the system to increase in comparison to the neat sample24.

Finally, for all the analyzed samples, at temperatures above 120 °C, the elastic moduli reached a plateau, indicating the formation of a stable network structure, which was not affected by the presence of filler as concerns the mechanical response.

Shape memory behavior of the prepared nanocomposites was investigated by TMA analysis. Figure 6 shows the four-cycle reversible thermo-actuation of DS_Neat, DS_GO_15 and DS_GO_45, evaluated by DMA in the film-tension geometry under a controlled static load by measuring the change in sample length with temperature. The reversible elongation (R_r) value, which corresponds to the amplitude of shape recovery, was calculated as the difference between strain values measured at 110 and 20 °C and reported in the table displayed in Figure 5.6.

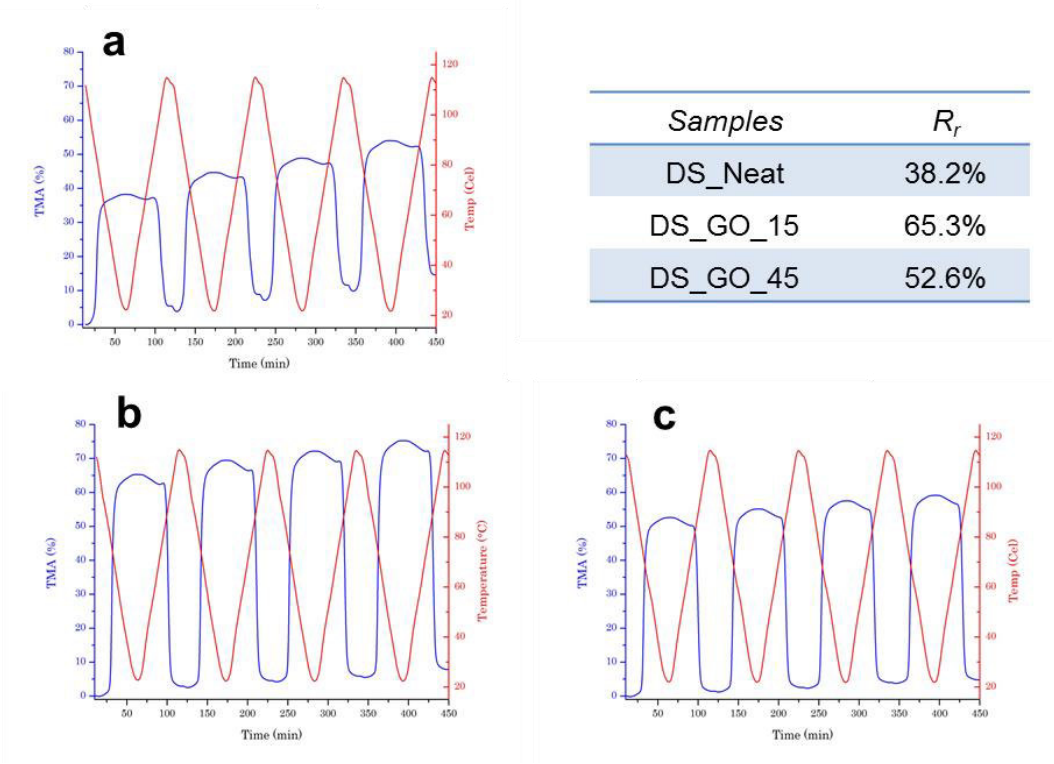

Samples	R_r
DS_Neat	38.2%
DS_GO_15	65.3%
DS_GO_45	52.6%

Figure 5.6 TMA trace of (a) DS_Neat, (b) DS_GO_15, (c) DS_GO_45 samples and table containing their reversible elongation (Rr) values

The presence of a lightly crosslinked epoxy resin combined with the thermally induced reversible switching from anisotropic to isotropic phase was responsible for the shape memory effect[27,28]. In the particular case of the obtained systems, thanks to their stress-induced polydomain to monodomain transition, the prepared LC epoxy elastomers are capable of reversible shape change under constant stress during temperature cycles, thus acting as temperature-induced shape-memory materials[29].

Prior to start, samples were thermally equilibrated at a temperature above clearing temperature ($T > T_i$). After 10 min, a ramping force was applied up to a fixed tensile loading (σ = 45 kPa, loading rate = 4.5 kPa/min). Successively, the samples were cooled to T = 20 °C, allowing the samples to spontaneously elongate due to soft-elastic response associated with isotropic to smectic transition. When reheated up to 110 °C, the samples gradually

regained their original length. The reversible elongation (R_r) was moderately constant for each sample over many temperature cycles, thus indicating reversibility with modest creep. This result was confirmed by the R_r values reported in the table in Figure 5.6, that were nearly constant for all the samples over the entire temperature cycle.

The cyclic thermoactuation was activated by the reversible formation of well-aligned liquid crystalline monodomains during cooling below the clearing temperature. On heating, due to entropic elasticity the anisotropic LC phase was lost, leading to the material in its original shape. As evidenced by Figure 5.6, the presence of GO enhanced thermo-mechanical behavior of DOMS-based elastomer, in a concentration-dependant manner. Neat DOMS_SA showed an elongation of about 40% during cooling under an uniaxial load corresponding to 45 kPa stress. On the other hand, the two nanocomposite samples showed a significant increase of the thermal actuation extent, which was more substantial at lower nanotube content. In particular, DS_GO_15 spontaneously stretched up to 65%, corresponding to a 50% increase of elongation compared to DS_Neat in the same solicitation conditions (Figure 5.6). For higher percentages of GO, i.e. in the case of DS_GO_45 a slight reduction in the actuation capability was observed, probably due to a less efficient mutual alignment of GO platelets with the rigid moieties of the matrix or to filler agglomeration, as also evidenced by DSC, DMA and WAXD results.

In order to give an insight on the microscale morphology developed upon the alignment of neat and GO containing LCE samples, SEM analysis was carried out on cryogenically fractured surfaces of films exhibiting a monodomain LC phase, formed during the cooling step under constant loading. As an example, Figure 7 reports the morphological features of fracture surfaces parallel and orthogonal to the stretching direction of DS_Neat and DS_GO_45, as evidenced by SEM.

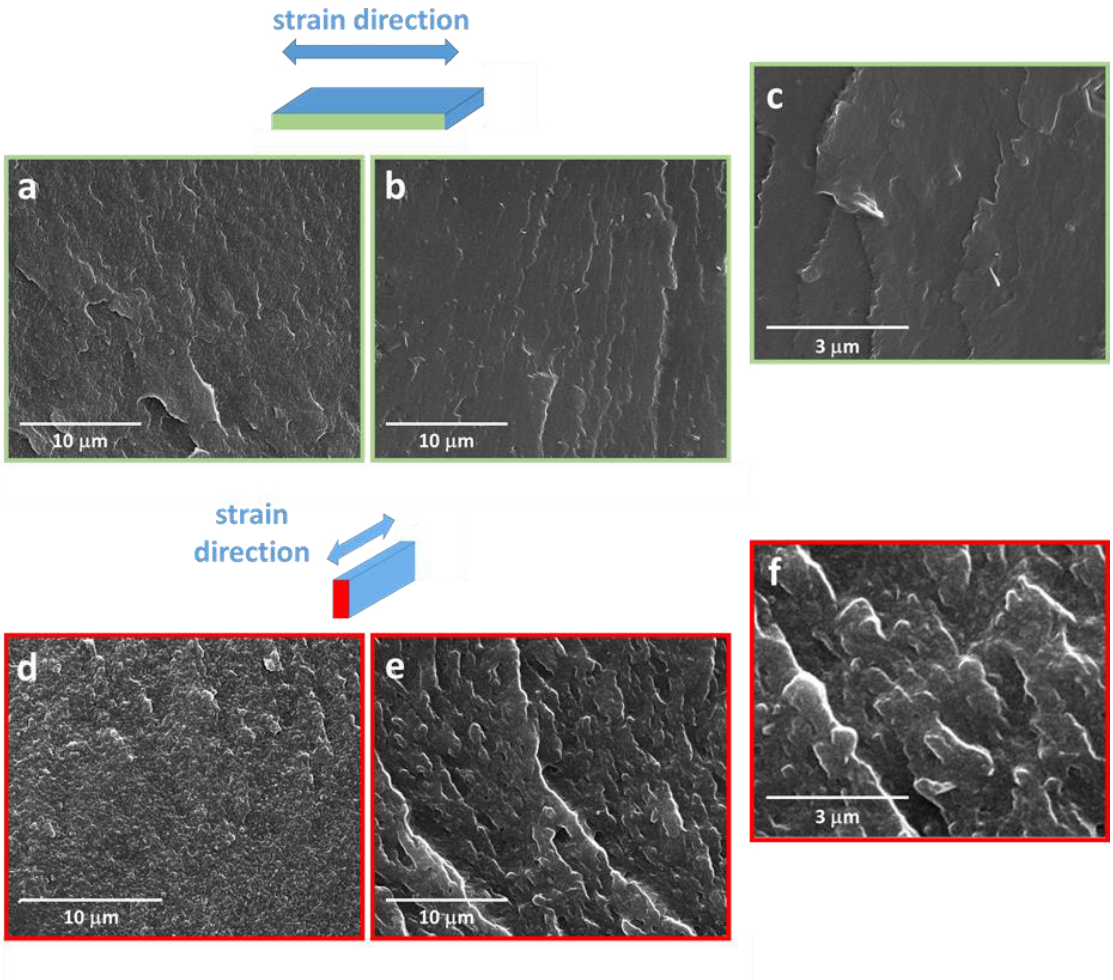

Figure 5.7 SEM images of fractured surfaces parallel (upper panel) and orthogonal (lower panel) to the stretching direction of (a, d) DS_Neat, and (b, c, e, f) DS_GO_45).

When the fracture surfaces parallel to the stretching direction were examined, DS_Neat (Figure 5.7a) and DS_GO_45 (Figure 5.7b) showed comparable morphologies. Since LC domains deviate crack propagation, SEM micrographs of fractured surfaces indicate that for both samples they are aligned along preferential orientations. This morphological feature reflects the generation of a complex layered structure at a mesoscale, which in turn is induced at a molecular level by the arrangement of mesogens progressively orientating along the stretching direction, due to the polydomain to monodomain transition.

Significant differences were observed analysing the cross sections orthogonal to the alignment direction. In the case of DS_Neat (Figure 5.7d), a remarkably rough surface was

observed, in which a number of small domains deviating crack propagation were visible. On the contrary, in the case of DS_GO_45, which spontaneously stretched up to 50%, the sample showed a higher degree of order. Large fracture planes perpendicularly aligned to the stretching direction were noticed (Figure 5.7e), demonstrating a long-range correlation between LC domains. It is likely that the GO platelets allowed the sample to easily reach the end of the polydomain to monodomain plateau, thus yielding in the same conditions a highly oriented system. This phenomenon can be attributed to the combined effect of the LC phase stability and network softness. In the case of DS_Neat, the network rigidity above the isotropization temperature was higher than that shown by DS_GO_45, as evidenced by DMA analysis. Therefore, the combination between a softer network and a sufficient degree of liquid crystallinity resulted in higher strain values observed during cycling thermomechanical tensile testing for the GO-filled LCE.

5.4 Conclusions

In this work, LC epoxy based elastomers reinforced with graphene oxide (GO) have been studied. In particular, the work has been focused on the optimization of the compatibilization procedure of carbonaceous nanofillers, and on the preparation and characterization of the nanocomposites. The effect of different amounts of functionalized GO on thermoactuaction was also evaluated.

Epoxy monomer DOMS was obtained by a synthetic protocol previously set up in our research group. GO used as nanofiller was synthesized by a modified Hummers method, and characterized by dispersion experiment, FTIR analysis, TGA analysis and EDS/SEM analysis that confirmed the occurrence of GNP oxidation.

An effective compatibilization strategy, able to improve the interfacial adhesion between epoxy resin and carbonaceous nanofillers and to promote their homogeneous dispersion, has been set up. This strategy has been based on the covalent functionalization of the GO surface with the epoxy monomer. The functionalized adducts have been isolated and characterized by means of TEM analysis, FTIR analysis and TGA analysis, showing that appreciable amounts of diepoxy monomers have been grafted on the nanofillers surfaces.

Nanocomposite films were prepared by cast molding and then characterized in their morphological, structural, thermomechanical and electrical properties. SEM images have shown a very homogeneous distribution and dispersion of both the epoxy-functionalized nanofillers within the polymeric matrix, confirming the effectiveness of the compatibilization approach.

The analysis of the thermal properties of the obtained materials have shown a decrease of Tg as a consequence of the addition of fillers. Besides, GO also reduced the network rigidity in the rubbery state. As for the phase behavior of the composites, a significant decrease of the isotropization temperature and the ΔHi associated to the smectic-to-isotropic transition has been observed, suggesting that the nanofillers inhibit the stability of the LC phase.

The thermomechanical characterization of the realized nanocomposites has shown that the GO enhanced the thermoactuation. More specifically, the extent of shape-recovery was significant in the case of DS_GO_15, as the combined effect of the LC phase stability and network softness resulted in higher strain values observed during cycling thermomechanical tensile testing for the GO-filled LCE.

5.5 References

1 Y. Liu, H. Lv, X. Lan, J. Leng, S. Du (2009): Review of electro-active shape-memory polymer composite. Composites Science and Technology, 69, 2064–2068

2 T. Ikeda, J. Mamiya, Y. Yu (2007): Photomechanics of Liquid-Crystalline Elastomers and Other Polymers. Angew. Chem. Int. Ed., 46, 506 – 528

3 Gulotty, R.; Castellino, M.; Jagdale, P.; Tagliaferro, A.; Balandin, A. Effects of Functionalization on Thermal Properties of Single-Wall and Multi-Wall Carbon Nanotube-Polymer Nanocomposites. ACS Nano 2013, 7, 5114

4Gulotty, R.; Castellino, M.; Jagdale, P.; Tagliaferro, A.; Balandin, A. Effects of Functionalization on Thermal Properties of Single-Walland Multi-Wall Carbon Nanotube-Polymer Nanocomposites. ACS Nano 2013, 7, 5114

5 Lynch, M. D.; Patrick, D. L. Organizing Carbon Nanotubes with Liquid Crystal Solvents. Nano Lett. 2002, 2, 1197−1201

6 G.C. Lama, P. Cerruti, M. Lavorgna, C. Carfagna, V. Ambrogi, G. Gentile Controlled Actuation of a Carbon Nanotube/Epoxy Shape-Memory Liquid Crystalline Elastomer J. Phys. Chem. C, 2016, 120 (42), pp 24417–24426

7 K. Wang, J. Ruan, H. Song, J.L. Zhang, Y. Wo, S.W. Guo, et al. Biocompatibility of graphene oxide Nanoscale Res Lett, 6 (2011), p. 8

8 Z. Cai, X. Meng, Y. Han, H. Ye, L. Cui, Q. Zhou Reinforcing polyamide 12,12 with graphene oxide via a two-step melt compounding process Compos A Appl Sci Manuf, 69 (2015), pp. 115–123

9 P. Pokharel, S. Choi, D.S. Lee The effect of hard segment length on the thermal and mechanical properties of polyurethane/graphene oxide nanocomposites Compos A Appl Sci Manuf, 69 (2015), pp. 168–177

10 S. Han, B.C. Chun Preparation of polyurethane nanocomposites via covalent incorporation of functionalized graphene and its shape memory effect Compos Part A-Appl S, 58 (2014), pp. 65–72

11 Tan, Lin, et al. "Functional shape memory composite nanofibers with graphene oxide filler." Composites Part A: Applied Science and Manufacturing 76 (2015): 115-123

12 Thakur, Suman, and Niranjan Karak. "Bio-based tough hyperbranched polyurethane–graphene oxide nanocomposites as advanced shape memory materials." RSC Advances 3.24 (2013): 9476-9482.

13 Chang, Zhenyue, et al. "Two-dimensional shape memory graphene oxide." Nature communications 7 (2016). Liu, Xuefa, et al. "Electro-active shape memory composites enhanced by flexible carbon nanotube/graphene aerogels." Journal of Materials Chemistry A 3.21 (2015): 11641-11649

14 Chen, Lei, et al. "Epoxy shape-memory polymer reinforced by thermally reduced graphite oxide: Influence of processing techniques." Journal of Applied Polymer Science 132.38 (2015).

15 Chen, Lei, et al. "Nanocomposites of epoxy-based shape memory polymer and thermally reduced graphite oxide: Mechanical, thermal and shape memory characterizations." Composites Part B: Engineering 91 (2016) 75-82;

16 Kim, J. E., Han, T. H., Lee, S. H., Kim, J. Y., Ahn, C. W., Yun, J. M. and Kim, S. O. (2011), Graphene Oxide Liquid Crystals. Angew. Chem. Int. Ed., 50: 3043–3047

17S. H. Lee, D. R. Dreyer, J. An, A. Velamakanni, R. D. Piner, S. Park, Y. Zhu, S. O. Kim, C. W. Bielawski, R. S. Ruoff, Macromol. Rapid Commun. 2010, 31, 281–288

18 V. Ambrogi, M. Giamberini, P. Cerruti, P. Pucci, N. Menna, R. Mascolo, C. Carfagna (2005): Liquid cristalline elastomers based on diglycidyl terminated rigid monomers and aliphatic acids. Part 1. Synthesis and characterization. Polymer, 46, 2105–2121

19 M. Giamberini , E. Amendola C. Carfagna (1995): Liquid Crystalline Epoxy Thermosets, Molecular Crystals and Liquid Crystals Science and Technology. Section A. Molecular Crystals and Liquid Crystals, 266,1, 9-22

20 K. Krishnamoorthy, M. Veerapandian, K. Yun, S.J. Kim (2013): The chemical and structural analysis of graphene oxide with different degrees of oxidation. Carbon, 53, 38-49

21 Giamberini, M.; Amendola, E.; Carfagna, C. Liquid Crystalline Epoxy Thermosets. Mol. Cryst. Liq. Cryst. Sci. Technol., Sect. A 1995, 266, 9−22

22 N.P. Zschoerper, V.Katzenmaier, U.Vohrer, M.Haupt, C.Oehr, T.Hirth, Analytical Investigation Of The Composition Of

Plasma-Induced Functional Groups on Carbon Nanotube Sheets. Carbon, 2009, 47(9), 2174-2185

23 Daniel R. Dreyer, Alexander D. Todd, Christopher W. Bielawski “Harnessing the chemistry of graphene oxide” Chem. Soc. Rev., 2014, 43, 5288

24 Giuseppe Cesare Lama, Pierfrancesco Cerruti, Marino Lavorgna, Cosimo Carfagna,Veronica Ambrogi, Gennaro Gentile,” Controlled Actuation of a Carbon Nanotube/Epoxy Shape-Memory Liquid Crystalline Elastomer” J. Phys. Chem. C 2016, 120, 24417−24426

25 Z. Xu, H. Sun, X. Zhao and C. Gao, Adv. Mater., 2013, 25, 188–193

26 T.-Z. Shen, S.-H. Hong and J.-K. Song, Nat. Mater., 2014, 13, 394–399

27 C. Liu, H. Qinb, P. T. Mather (2007): Review of progress in shape-memory polymers. J. Mater. Chem., 17, 1543–1558

28 Meng, H.; Li, G. A Review of Stimuli-Responsive Shape Memory Polymer Composites. Polymer 2013, 54, 2199−2221

29 Giamberini, M.; Cerruti, P.; Ambrogi, V.; Vestito, C.; Covino, F.; Carfagna, C. Liquid Crystalline Elastomers On Diglycidyl Terminated Rigid Monomers And Aliphatic Acids. Part 2. Mechanical Characterization. Polymer 2005, 46, 9113−9125

CHAPTER 6

General conclusion and future outlook

6.1 Conclusion

In this thesis, shape memory polymer nanocomposites were produced using epoxy-based liquid crystalline polymer, as matrix, and surface-modified MWCNT, as well as surface-modified GNP, as nanofiller. For the LCE matrix, DOMS monomer was selected. EPON was used for the study on the dispersion and compatibilization of carbonaceous nanofillers.

The main problem faced with these systems consisted in the formation of clusters formed by nanofillers. The surface modification was necessary to enhance the dispersion and the distribution of nanoparticles within the matrix. For this reason, a compatibilizaton strategy of MWCNT and GNP was investigated. The products of this procedure were analyzed and characterized from thermal, chemical and morphological point of view. Such result was possible if MWCNT-COOH were adopted.

Solvent dispersion experiment, FTIR spectroscopy, TEM analysis and TGA analysis proved that an epoxy-grafting process occurred on the surface of both kind of nanoparticles, even in higher amount with respect to the predicted one calculated on the carboxylic groups on the surface of MWCNT, due to the homopolymerization of the epoxy monomer.

Concerning GNP, a first oxidation process was necessary, in order to promote the exfoliation of graphene sheets. Different amount of oxygen-containing groups were achieved, depending of the treatment. Once these oxidations occurred, several analyses were performed to prove the actual surface modification. WAXS and Raman spectroscopy gave indications on the different structures depending on the oxidation, proving that increasing the degree of oxidation the disruption of the nanoparticles, as well as the distance between graphene sheets, was increased. However, as noticed from DLS, the

reduction of the GNP cluster size, did not affect on the average size of the nanoplatelets. Moreover, FTIR proved the actual formation of different oxygen-containing groups on the surface. Through TGA and DSC, It was possible to detect the amount of such functional groups starting from the non-linear dependence of the enthalpy of the process with type and amount of those groups.

SEM and TEM analyses of dried GO showed how its self-assembly ability changed with the oxidation degree. At high oxidation level a self-standing GO films were detected.

Methylene blue was used to investigate the specific surface area of GO samples. At low-oxidized particle dispersion, GO sheets were well dispersed. Instead, for those sample with an higher oxidation degree, more stacking phenomena occurred. This was also proved by the BET method for evaluation of specific surface area, in which a decrement of SSA was observed with the increasing of oxidation degree.

For this reason, only the intermediate-oxidized GO dispersion was embedded within the polymer matrix to obtain nanocomposites. This choice was made because it represented the best trade-off between the presence of suitable functional groups, needed for the surface modification, and the reduced tendency to self-agglomeration during processing.

This sample, then, experienced the surface-epoxidation. The obtained adducts were characterized by means of TEM analysis, FTIR analysis and TGA analysis, showing that appreciable amounts of diepoxy monomers have been grafted on the nanofillers surfaces.

This compatibilization strategy is the first part of the optimized procedure aimed to obtain homogenous nanocomposites. When sebacic acid is added to the mixture of DOMS monomer and modified MWCNT or GNP, in presence of a catalyst, and is then poured in pre-heated glass mold, SMPNC is obtained.

The presence of MWCNTs changed the thermo-mechanical behavior of the starting material, changing the LC degree of the sample, enabling the design of new shape-memory materials for target applications and even achieving the triple shape memory response.

As for MWCNT, the nanocomposites in which GO was dispersed showed an increased thermoactuation, in terms of extent of shape-recovery. They were also softer than the neat resin. This was translated higher strain values observed during cycling thermomechanical tensile testing for the GO-filled LCE.

With respect to the most recent advances in these fields, this work combines the high actuation efficiency and mechanical properties of the epoxy-based liquid-crystalline resins with the enhancement of the actuation extent and the electro-actuation given by the inclusion of conductive nanoparticles. Despite the processability of these systems is lower than the thermoplastic ones, such as polyurethanes, their liquid crystallinity provides a much more appreciable actuation, also with respect to other epoxy-based shape memory systems.

6.2 Future development

At the moment, this kind of material is being used to obtain a laminate, in which one layer consist in a pre-strained LCE, coupled with another layer of another kind of SMP, whose main characteristic is the ability to recover its permanent shape while the system is cooling down. In this way, the obtained laminate can be intended as an autonomous shape-shifting system.

In this view, the previously characterized SMPNCs, thanks to the presence of carbonaceous material used as nanofiller, can be used in order to promote an electric field-induced shape-shifting material.

Appendix A

A.1 List of figures

DS_3.0CNT. (c) Storage modulus (E') and tan δ of DOMS_SA, DS_0.75CNT, DS_1.5CNT, and DS_3.0CNT. (d) Stress−strain curves of DOMS_SA, DS_0.75CNT, DS_1.5CNT, and DS_3.0CNT

Figure 3.13 Thermomechanical properties of LC nanocomposite elastomers: (a) WAXD diffraction pattern of the unstretched (left) and the fully stretched DOMS_SA (right, corresponding to the elongated state indicated by the arrow in panel b) and corresponding intensity integrations along the meridian axis normalized to the reflection at higher 2θ (top left and right). (b) Four-cycle two-way shape-memory behavior of DOMS_SA under tensile loading corresponding to 45 kPa. (c) WAXD diffraction pattern of the unstretched (left) and the fully stretched DS_0.75CNT (right, see the arrow in panel d) and corresponding intensity integrations along the meridian axis normalized to the reflection at higher 2θ (top left and right). (d) Four-cycle two-way shape-memory behavior of DS_0.75CNT under tensile loading corresponding to 45 kPa. (e) Two-way shape-memory behavior of DOMS_SA and DS_0.75CNT under decreasing tensile loadings (σ = 180 to 5.6 kPa). (f) Triple shape-memory behavior of DOMS_SA and DS_0.75CNT

Figure 3.14 a) Intensity integrations along the meridian axis of WAXD diffraction pattern of the unstretched (top) and the fully stretched form of DS_1.5CNT (bottom, see the arrow in Fig. 3.14b); b) four-cycle two-way shape memory behavior of DS_1.5CNT under a tensile stress of 45 kPa; c) intensity integrations along the meridian axis of WAXD diffraction pattern of the unstretched (top) and the fully stretched form of DS_3.0CNT (bottom, see the arrow in Fig. 3.14d); d) four-cycle two-way shape-memory behavior of DS_3.0CNT under a tensile stress of 45 kPa.

Figure 3.15 Temperature-controlled X-ray diffractometry. Intensity integrations along the meridian axis of diffrattograms collected at different temperatures during cooling of (a) DOMS_SA and (b) DS_0.75CNT. All spectra are normalized to the reflection at higher 2θ angle. (c) Temperature dependence of the intensity ratio (I_2/I_1) of the peaks corresponding to reflections at lower and higher 2θ angles, respectively

Figure 3.16 Temperature-controlled X-ray diffractometry. Intensity integrations along the meridian axis of diffractograms collected at different temperatures during cooling of: a) DS_1.5CNT; b) DS_3.0CNT. All spectra are normalized to the reflection at higher 2θ angle

Figure 3.17 Temperature-controlled X-ray diffractometry evidencing the peak shift due to gradual increase of the component at higher 2θ at the expense of the amorphous halo in the broad convoluted reflection centred at about 19.2° (see Figure 3.15a,b and Figure 3.16). Intensity integrations in the 2θ range 12-28° along the meridian axis of diffractograms collected at different temperatures during cooling of: a) DOMS_SA; b) DS_0.75CNT; c) DS_1.5CNT; d) DS_3.0CNT. All spectra are normalized to the reflection at higher 2θ angle. Please note that the shoulder at about 25.5° that can be observed in b, c and d, is a third component due to the presence of MWCNT (corresponding d-spacing = 0.35 nm).

Figure 3.18 SEM micrographs and corresponding schematic representation of the structure of (a) DOMS_SA and (b) DS_0.75CNT at different stages of the thermomechanical test: (i) unstretched samples at room temperature; (ii) samples at T > Ti under an applied load of 45 KPa; and (iii) stretched samples after anisotropization. Mesogens are represented as blue rods. The walls of MWCNT are schematized with black lines. Mesogens are stacked in smectic LC domains at stages i and iii. At stage iii, a higher orientation degree is evident for the sample DS_0.75CNT. Above Ti (stage ii), the disruption of the smectic phase is shown for both samples.

Figure 3.19 Volume resistivity (Ωcm^{-1}) as a function of MWCNT content in DOMS-based nanocomposites

Figure 3.20 Time sequence of SME due to Joule effect.

Figure 3.21 Temporal evolution of SME due to resistive heating. a) Picture sequence took at different times with thermo-camera (distance between cyan lines is 15 mm). b) Line refers to the

Figure 5.5 DMA curves of (a) DS_Neat, (b) DS_GO_15, and (c) DS_GO_45. (d) Comparison of E' and tand curves of all samples.

Figure 5.6 TMA trace of (a) DS_Neat, (b) DS_GO_15, (c) DS_GO_45 samples and table containing their reversible elongation (Rr) values

Figure 5.7 SEM images of fractured surfaces parallel (upper panel) and orthogonal (lower panel) to the stretching direction of (a, d) DS_Neat, and (b, c, e, f) DS_GO_45).

A.2 List of Tables

A.3 List of publications

Papers and proceedings:

G. C. Lama, G. Gentile, P. Cerruti, M. Lavorgna, V. Ambrogi, C. Carfagna, "Shape-Memory Nanocomposite Elastomers Filled with Carbon Nanomaterials", Advances in Science and Technology, Vol. 100, pp. 5-10, 2017.

G. C. Lama, P. Cerruti, M. Lavorgna, C. Carfagna, V. Ambrogi, G. Gentile, “Controlled Actuation of a Carbon Nanotube/Epoxy Shape-Memory Liquid Crystalline Elastomer”, J.Phys.Chem.C, Vol. 120, 24417−24426, 2016.

A. Marotta, G. C. Lama, G. Gentile, P. Cerruti, C. Carfagna and V. Ambrogi, “Shape-memory effect of nanocomposites based on liquid-crystalline elastomers”, AIP Conf. Proc. 1736, 020062 (2016).

G. C. Lama, G. Nasti, V. Ambrogi, P. Cerruti, G. Gentile and C. Carfagna, “Epoxy elastomers reinforced with functionalized multi-walled carbon nanotubes as stimuli-responsive shape memory materials”, AIP Conf. Proc. 1599, 182 (2014).

A.4 Conference Contributions

“Tailoring Shape Memory Behavior of Lightly Cross-Linked Elastomers”. Oral Presentation, Materials 2016, Catania, Italy. 12/02/2016

“Shape memory properties in lightly cross-linked elastomers filled with MWCNT”. Oral Presentation, Macrogiovani, Catania, Italy, 12/05/2016

“Shape-mamory properties in epoxy-based elastomers filled with MWCNTs” Oral Presentation, EPF, Dresden, Germany, 24/06/2015

“Epoxy Elastomers Reinforced with Functionalized Multi-Walled Carbon Nanotubes as Stimuli-Responsive Shape Memory Materials” Oral Presentation, TOP, Ischia, Italy, 26/06/2014